UiT
THE ARCTIC
UNIVERSITY
OF NORWAY

Faculty of Science and Technology
Department of Physics and Technology

Comparing sea ice areas identified within quad-polarimetry high-resolution SAR satellite scenes with the same areas in dual-polarimetry medium resolution SAR scenes

—

Magnus Hvidsten

EOM-3901 Master's thesis in Energy, Climate and Environment 30 SP

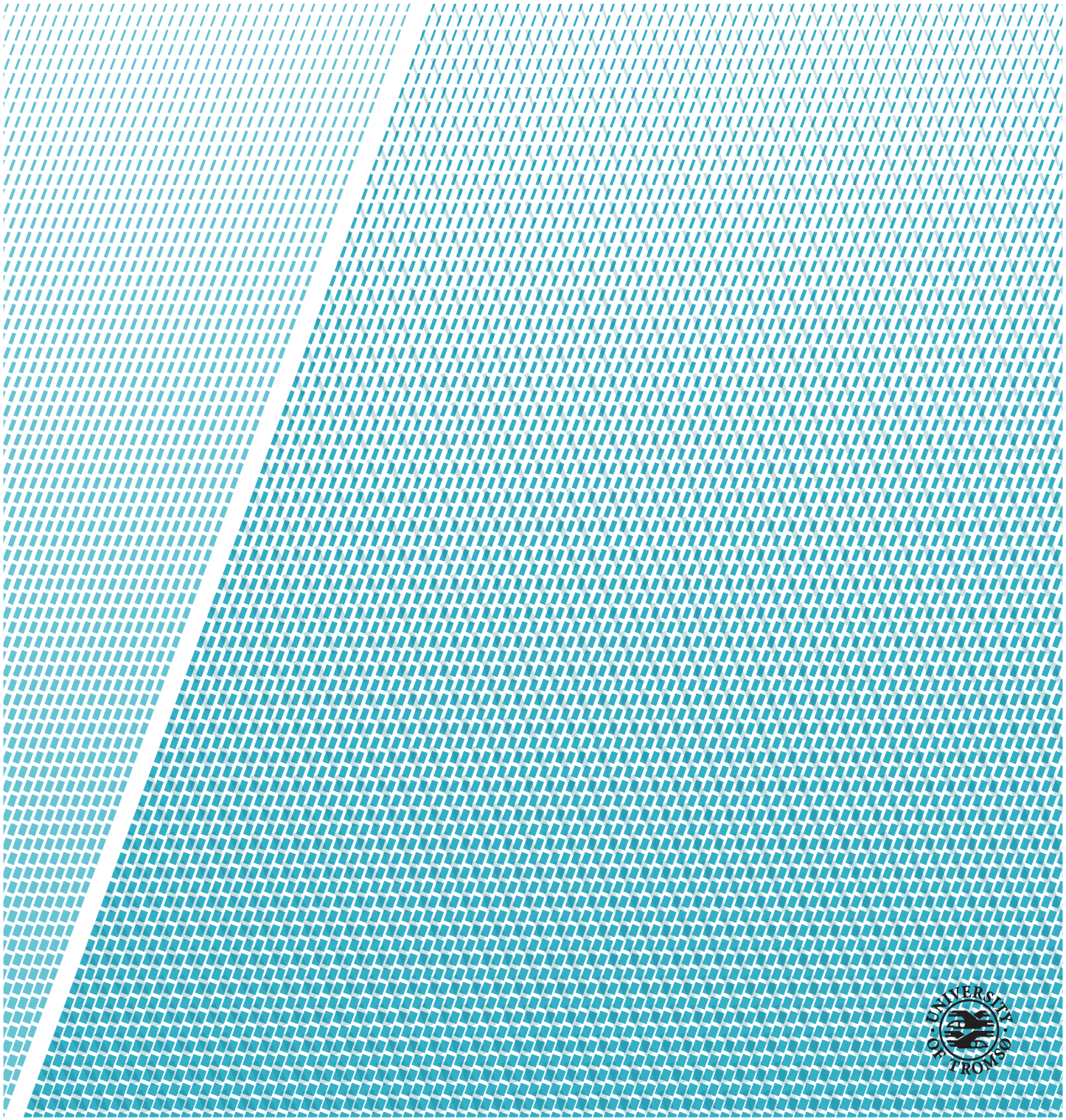

Abstract

This thesis compares polarimetric features from quad-polarimetric (quad-pol) SAR (synthetic aperture radar) data and emulated dual-polarimetric (dual-pol) SAR data to investigate the information captured over sea ice areas located in the Barents Sea. The emulation is performed by averaging, downsampling, reduction of polarization channels, and adjustment of the noise equivalent sigma zero (NESZ). SAR is an active imaging system which enables imaging of remote regions under challenging weather conditions such as in the Arctic. The polarimetric features of entropy (H) and $\bar{\alpha}$, and the H/$\bar{\alpha}$-plot is compared, as well as the cross-polarizarion ratio and the damping ratio. The co-polarization ratio is used to provide information of the constituents in the imaged scene. It is shown that the interpretation of H, $\bar{\alpha}$, and the H/$\bar{\alpha}$-plot from emulated dual-polarimetric HH/HV data are not consistent with conventional interpretation of H, $\bar{\alpha}$, and the H/$\bar{\alpha}$-plot. The cross-polarization ratio and the damping ratio yielded promising results, and it was shown that for the data utilized in the thesis constituents of a given size can be separated from its surroundings in the emulated dual-polarimetric HH/HV data.

The thesis delivers evidence of information loss between quad-polarimetric SAR data and dual-polarimetric SAR data and discusses the underlying reasons behind the information loss. It lays the ground for further analysis of the reasons for information loss in multi-polarization and single-polarization parameters between quad-polarimetric SAR data and dual-polarimetric SAR data.

Acknowledgements

First and foremost I would like to thank my supervisors Malin Johansson and Camilla Brekke, for all the discussions and the good advices along the way. I would also like to thank CIRFA for giving me the luxury of having a desk in their premise, and the employees at CIRFA for many good advises along the way.

Contents

List of Figures

List of Tables

Abbreviations

Dual-pol	Dual-polarimetric
EM	Electromagnetic
FQ13	Fine quad-polarimetric mode 13
H	Entropy
LUT	Look-up table
NESZ	Noise equivalent sigma zero/Noise floor
NRCS	Normalized radar cross section
PRF	Pulse repetition frequency
psu	Practical salinity units
Quad-pol	Quad-polarimetric
RAR	Real aperture radar
RCS	Radar cross section
r.m.s	Root mean square
ROI	Region of interest
SAR	Synthetic aperture radar
SCWA	ScanSAR Wide A
SLC	Single look complex
SNR	Signal-to-noise ratio
SW	Swath width
UV	Ultra violet

1 Introduction

This thesis utilizes synthetic aperture radar (SAR) data collected over the Arctic region. The Arctic region is a remote region with harsh weather conditions covered by clouds and an absence of sunlight for a longer period of the year. This limits the usage of in-situ measurements and optical space-borne radars. The SAR instrument is able to handle these conditions in a satisfactory manner as it utilizes the microwave region of the electromagnetic (EM) spectrum, enabling the EM waves to travel through the cloud cover, cope with the harsh weather conditions as well as not being dependent on sunlight as it is an active radar system. Furthermore, SAR satellite data have the temporal and spatial resolution needed to provide satisfactory surveillance in the Arctic region.
Single- and dual-polarimetric C-band SAR are often used for sea ice monitoring in the Arctic, e.g. the Radarsat-2 and Sentinel-1 satellites. The monitoring includes ice drift, ice concentration mapping and classification of ice types [2]. The information is often delivered to the Arctic maritime industry such as oil and fishing industry. Quad-polarimetric SAR data contains more polarimetric information than single- and dual-polarimetric SAR data, but is limited by the swath width. The additional polarimetric information enables a more thorough separation of scattering mechanisms, useful for studies concerning, but not limited to, sea ice classification.
This study aims to emulate dual-polarimetric data from quad-polarimetric data located in the Barents Sea to investigate the differences and similarities between dual-polarimetric products and quad-polarimetric products. The emulation is done to meet the qualities of ScanSAR products (specifically ScanSAR Wide A) through pixel spacing adjustment, reduction of polarization channels

and adjustment of the noise equivalent sigma zero/noise floor (NESZ). The information loss between quad-polarimetric data and dual-polarimetric data is investigated by means of multi-polarization features and single-polarization features. These features is deduced through decomposition and intensity ratios, and covers the nature of the scattering mechanisms and the general behaviour of the scattering surfaces.

1.1 Motivation

This thesis aims to further investigate the relationship between spatial regions identified within high-resolution quad-polarimetric scenes and medium resolution dual-polarimetric SAR scenes. This is done by investigating the polarimetric features of entropy (H), $\bar{\alpha}$, and the H/$\bar{\alpha}$-plot in addition to the cross-polarization ratio and the damping ratio.
Quad-polarimetric data contains more detailed information than single- and dual-polarimetric data but covers a smaller area. Little is known about how distinct spatial regions identified within these high-resolution scenes translate into the areas in the medium resolution SAR scenes. Some studies have used quad-polarimetric scenes and reduced the pixel spacing to meet the resolution of dual-polarimetric scenes (e.g. [49]) and compared the scattering information. These studies focused on radar imaging over land, while this master thesis are looking into scattering information in the Arctic regions. In addition adjustment of the NESZ is considered in this thesis, as the NESZ is different for quad-polarimetric data and dual-polarimetric data. The thesis utilizes quad-polarimetric SAR data and emulates dual-polarimetric HH/HV SAR data, as most operational dual-polarimetric SAR offer the HH/HV combination.

1.2 Objectives

This thesis main goal is to investigate the similarities and dissimilarities between quad-polarimetric and dual-polarimetric data. This is done by emulating dual-polarimetric data from quad-polarimetric data including adjustment of the NESZ before a comparison of a subset of polarimetric features is executed. The multi-polarization features H and $\bar{\alpha}$ is investigated aswell as the H/$\bar{\alpha}$-plot. These features are first and foremost derived for usage in fully polarimetric systems where all polarization channels are present, and the emulation of dual-polarimetric data is done step-wise to investigate the effects of these steps. The differences found for each step in the features are discussed, and the eigenvalues and eigenvectors are used to deliver evidence of the changes observed. The method of extraction and interpretation is another aspect of

the thesis as the multi-polarimetric features is derived for usage in a fully polarimetric system. The main focus of discussion in the thesis is based on these features as these can be used to explain the scattering mechanisms of the scene. Further the cross-polarization ratio and the damping ratio is utilized to compare the information loss from quad-polarimetric data to dual-polarimetric data. These studies are split into 4 steps. These give insight in how the intensity of the backscatter is altered. Together with the multi-polarization features they give insight in which of the differences between quad-polarimetric and dual-polarimetric data that alters the results in the presented features and to what extent.

1.3 Contributions to the field

The study introduces an investigation of information content in quad-polarimetric SAR data and dual-polarimetric SAR data. This is done by comparison of different polarimetric features that is often used when interpreting radar products. The polarization features H, $\bar{\alpha}$, the H/$\bar{\alpha}$-plot, the cross-polarization ratio, and the damping ratio for SAR data located in the Arctic is studied, and gives insight in which of the differences between quad-polarimetric data and dual-polarimetric data that alters the features, the information contained in the data, and to what extent. It lays the ground for further analysis, and presents ideas of what should be included in further studies.

1.4 Outline

This study is divided into 10 chapters after the introduction;

- Chapter 2 introduces basic SAR theory.
- Chapter 3 presents basic information about the radar sensor used and the study area.
- Chapter 4 presents theory of sea ice.
- Chapter 5 presents background theory needed in the thesis. This theory is used in the method of the thesis.
- The polarimetric features utilized in the thesis is presented in chapter 6.
- In chapter 7 the method used to obtain the results is presented.

- The results and discussion are given in chapter 8, and the conclusion of the thesis is found in chapter 9.

- Chapter 10 introduces further work.

2

Synthetic aperture radar

A SAR satellite is used to collect the data utilized in the study. It is a sensor used in satellites such as RADARSAT-2. In this chapter basic SAR theory is presented, as knowledge of SAR is essential when investigating the data and the results. An imaging radar system falls within one of two categories; Real-aperture radars (RAR) or SAR. The major difference between the two is SARs ability to synthesize a longer antenna, enhancing the azimuth resolution. SAR utilizes the backscattered response of EM radiation to obtain information about the object of interest. SARs are active radar systems that utilize the microwave region in the EM spectrum, i.e. wavelengths between the P-band and the Ka-band can be used [28]. Normally wavelengths between the P-band and the X-band is used in space-borne radars, as these cope with atmospheric disturbance, clouds, and weather conditions because of their wavelength [28].

An active imaging system is both transmitting and receiving EM radiation. In this way the wavelength of the EM radiation can be chosen, as opposed to passive imaging systems where exterior sources of EM radiation is used. Knowing the wavelength of the incidence EM radiation enables precise calculations of the ground truth, as the incoming and outgoing signals are known. Wavelengths can also be chosen such that both day and night imaging is possible, as opposed to passive imaging systems utilizing EM radiation from the Sun. The pulses transmitted is in the form of a chirp signal. The reason arises in range resolution, where modulation is needed to obtain a higher resolution. It is done as it is desired to have high energy and a wide bandwidth in the signal. Because of system limitations high energy often implies a longer signal,

while a wide bandwidth implies a short signal. To cope with these prerequisites a chirp signal is used. The echoes received from one point on the ground is recorded coherently and combined to synthesize a linear array [14]. As the SAR is moving over an object doppler shift is present. As the point of interest enters the antenna footprint the doppler shift is positive, and decreases to zero when the antenna is directly above the point before becoming negative [14]. Use of SAR therefore requires knowledge about doppler shift and doppler history.

2.1 Radar geometry

SAR is normally mounted such that the imaged scene is illuminated from the side, as illustrated in figure 2.1(a). The reason being that an oblique view of the scene eliminates the ambiguities of having two symmetric equidistant points, i.e. right and left can be decided.

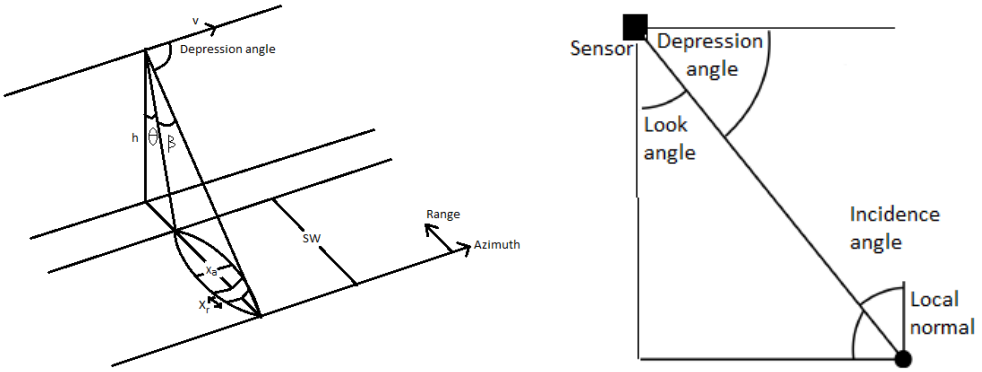

(a) (b)

Figure 2.1: (a) Radar geometry, based on figure 6-25 in [14]. Where v is the direction of the flight path, β is the beam width, θ is the look angle, h is the distance from the sensor to the ground, X_a is the azimuth resolution, X_r is the range resolution, SW is the swath width. (b) Relationship between the look angle and the incidence angle.

There are several angles that represents the geometry of a SAR imaging system (See figure 2.1(a) and figure 2.1(b)). In figure 2.1(b) the incidence angle and the look angle are illustrated. When the surface illuminated is flat the incidence angle equals the look angle. The angle extended between the horizontal line drawn directly to the side of the aircraft and the upper part of the beam in figure 2.1(a) is called the depression angle. The portion of the scene that is

illuminated with the smallest depression angle possible is called the far-range, while the edge of the footprint closest to the aircraft is called near range. Finally the intersection between these two areas is called mid-range [5]. The angle between the vertical line drawn directly from the aircraft and the point of which the incident wave hits is called the look angle (θ) [14].
As the radar is moving a continuous strip is mapped in the direction of flight, with a width defined as the swath width (SW) [14]. (See figure 2.1). The flight line is often referred to as the azimuth direction (along track), while the direction perpendicular to the azimuth direction is called range direction.

The backscatter from the imaged scene is collected in slant-range, a presentation utilizing the distance from the radar to the point where the radiation hits. When interpreting these outputs ambiguities and artifacts arise. Radar shadowing occurs when the signal meets topographic obstacles on the ground such as elevations of the ground. The illumination can only see one side of the obstacle, causing a shadow on the far side. Layover happens when the elevation angle of the obstacle is big, causing the backscatter from the top of the obstacle to be received before that from the base of the obstacle. Forshortening is a less extreme case, where the distance from the base and the top of the obstacle is measured to be smaller than it is [5]. The desired output for the user is often as ground truth. The connection between these two representations are known. The ground truth range resolution is decided by the minimum distance between two separable points [14]. The range resolution is determined by the time difference between the signal received from different points, which gives the distance between the two points on the ground. This is expressed in the following manner:

$$\Delta t = \frac{2X_r}{c} sin\theta_i \tag{2.1}$$

where Δt is the time difference of the received echoes, X_r is the distance between the two points in ground range, c is the speed of light and θ_i is the incidence angle.

As the output pulse length is limited by the bandwidth [14], the ground range resolution X_r can be written as:

$$X_r = \frac{c}{2Bsin\theta_i} \tag{2.2}$$

where B is the bandwidth.

As in range direction, the azimuth resolution is defined as the two nearest

separable points in azimuth direction, i.e. on a constant delay line [14]. The azimuth resolution X_a is given as:

$$X_a = \frac{h\beta}{cos\theta_i} = \frac{h\lambda}{Lcos\theta_i} \tag{2.3}$$

where h is the distance from the ground to the radar, β is the antenna beam width in azimuth direction, λ is the wavelength and L is the antenna length. For a SAR imaging system the length of the antenna (L) is synthesized. A target on the ground stays inside the beam for a longer period, and is viewed from different angles [14]. The systematic imaging of the target enables measurements of phase and doppler history, which enables a longer synthesized antenna (See figure 2.2).

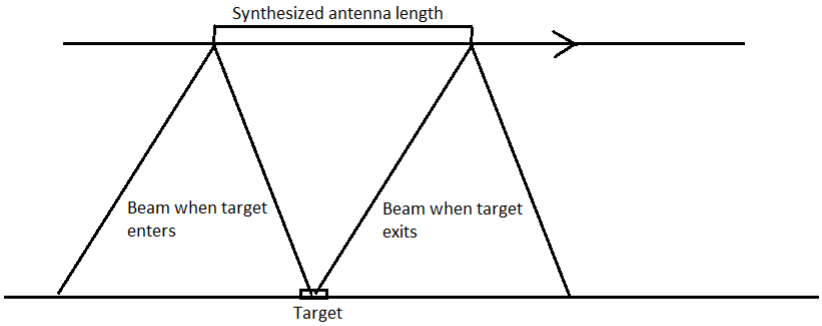

Figure 2.2: Radar geometry, based on figure 6-32 in [14]

The synthesized antenna leads to a new expression of X_a for SAR imaging systems:

$$X_a = \frac{L}{2} \tag{2.4}$$

If the antenna beam width (β) is held constant, the look- or depression angle determines the size of the area illuminated. A bigger look angle (moving the illuminated area towards the far range) causes the size of the area illuminated to increase, making the coverage larger but implies lower resolution as the time between each received echo increases relative to the distance on ground. Also artifacts caused by the slant-range representation becomes more apparent, such as radar shadowing, layover, and forshortening [5].

2.2 Frequency

EM radiation consists of a coupled electric and magnetic force field, and is utilized in remote sensing. This coupled field propagates through space in an oscillatory manner, making the coupled force field act as a wave [52]. The power contained in the wave is dependent on the frequency of the wave.

The span of frequencies an EM wave can have is described in the EM spectrum. The EM spectrum ranges from 0.3 Å up to 30 000 km in wavelength, and 10^{20} Hz to 10 Hz in frequency. The EM spectrum is divided into spectral regions such as the radio band, the microwave band, the infrared band, the ultra violet (UV) band, and the X-ray band, which are all used in radar imaging [14]. In this study only the microwave band is investigated, as SARs utilize microwaves. The microwave band can be further divided into bands P, L, S, C, X, Ku, K, Ka, ranging from roughly 0.3 GHz to 40 GHz. Microwaves with frequencies less than about 10 GHz ignores the impact of the atmosphere [52], i.e. bands P, L, S, C, and X penetrate the atmosphere without much interference and is often used in environmental surveillance. Bands Ku, K, and Ka is therefore normally not used in space borne radars. C-band is often used for operational monitoring of sea ice as it discriminates sea ice and water well. It is also sensitive to salinity, and can differ between different types of sea ice [34]. In this study C-band at 5.405 GHz is used. The EM spectrum and the microwave region can be seen in figure 2.3.

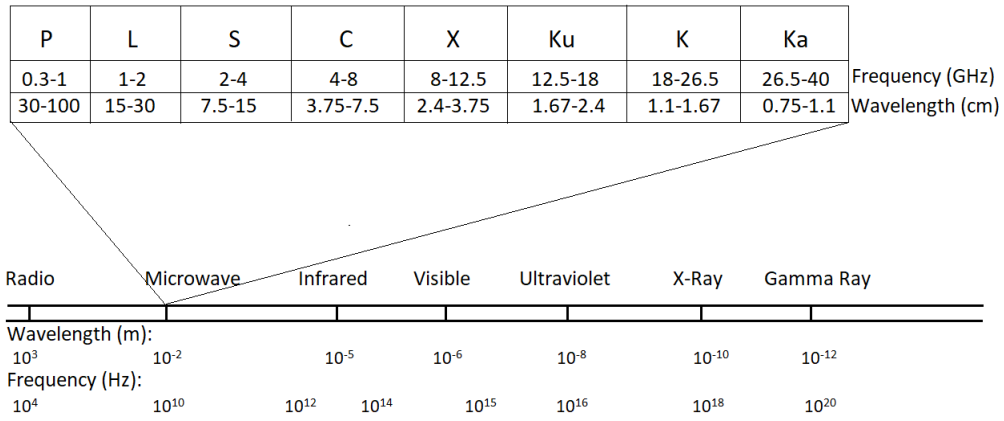

Figure 2.3: EM spectrum with microwave bands, based on figure 2.1 in [8]

SARs utilize different parts of the EM spectrum, as the frequency of an EM wave decides the ability of the wave to penetrate a medium. Typically waves with long wavelengths (small frequencies) penetrate deeper into a medium,

following the expression of the penetration depth (L_p):

$$L_p = \frac{\lambda\sqrt{\varepsilon'}}{2\pi\varepsilon''} \tag{2.5}$$

where L_p is the penetration depth, ε' is the permittivity of the medium which the wave travels through, and ε'' is the permittivity of the medium which the wave penetrates [14].

2.3 Polarimetry

In radar remote sensing polarization plays a major role in the output of an observation. The amount and type of data from a target is dependent on the polarization. The polarization of an EM wave is defined as the polarization of the electric field [14]. In a horizontally polarized EM wave the electric field is parallel to the plane of incidence, while in the vertical case it is orthogonal. In remote sensing, the antenna is often designed to both transmit and receive EM waves of different polarizations; horizontal linear and vertical linear. This is accomplished by first sending a wave of one polarization before sending the next. An EM wave can also be circular polarized. If both polarizations are sent simultaneously with a 90° phase difference, a circular polarization is achieved [28]. It is however not possible to obtain a perfectly circular EM wave from a radar with todays technology. Upon receival the antenna utilizes both the horizontal- and vertical polarization channels, as the scattered wave can be differently polarized. The type of transmitted and received polarization of the EM wave is often denoted with the letters H (horizontal linear polarized) and V (vertical linear polarized), where the first letter denotes the transmitted wave polarization and the second letter denotes the received wave polarization.

SAR systems operate with different polarization combinations or polarization channels. Normally this is done in one of three ways; quad-polarimetric (quadrature polarized), dual-polarimetric (dual polarized) and single-polarimetric (single polarized).

- Quad-polarimetric:

  In a quad-polimetric system both H and V polarization are transmitted and received. This results in 4 different polarization combinations that can be utilized, namely:

HH, VV, HV, and VH [35].

In a quad-polarimetric system the transmitted wave polarizations and the received wave polarizations must be orthogonal pairs. As it is only possible to transmit one wave at a time, the polarizations has to be time-multiplexed. This in turn includes caution concerning the Nyquist-sampling theorem with respect to the pulse repetition frequency (PRF) [45]. The major advantage of a quad-polarimetric system is its high resolution, and that the full scattering matrix can be obtained (See section 5.1). Quad-polarimetric systems utilize both amplitude and phase differences and enables more thorough analysis of the scattering. The potentially big disadvantage of such a system is the small areal coverage. As a direct consequence of the PRF, the swath width of a quad-polarimetric system must be no higher than half of a dual-polarimetric or single-polarimetric system [45], limiting the use of quad-polarimetric systems in operational remote sensing.

- Dual-polarimetric:

  Dual-polarimetric systems transmits one polarization channel and receives two. The result is that a dual-polarimetric system utilizes 2 different polarization combinations, namely:

  HH/VV or VV/VH, or HH/HV [35].

  The dual-polarimetric HH/VV combination requires a quad-polarimetric processor but is included here as two polarization channels are used in this combination. The dual-polarimetric data does not include the relative phase between the two received channels, and does not deliver the same polarimetric information as the quad-polarimetric data [45]. The resulting data from dual-polarimetric systems typically has a lower resolution than quad-polarimetric data, but covers a larger area. This makes dual-polarimetric systems better suited for applications where surveillance over large areas are desired, such as operational sea ice charting.

- Single-polarimetric:

  Single-polarimetric systems only transmits and receives one polarization channel and are therefore only capable of the following:

  HH or HV or VH or VV [35].

  Single-polarimetric systems can only deliver one single image of the scene. Of the three different SAR systems, single-polarimetric systems are the longest running systems, and are still being used in certain aspects of remote sensing, such as oil spill detection.

2.4 Scattering

As an EM wave interacts with a target some of the energy is absorbed by the target, while some is re-radiated [14]. The re-radiated energy travels in a new direction in the form of a scattered EM wave. The magnitude and direction of propagation of the scattered EM wave is dependent on the geometric features and the material properties of the object causing the scattering [14]. Scattering can be defined as the physical process where radiation moves out of its trajectory path because of mediums of which the radiation either passes through or bounces off. Scattering can occur in different ways, normally described by surface scattering, double bounce scattering, and volume scattering.

2.4.1 Surface scattering

Surface scattering occurs when the incoming radiation is scattered only once, on the intersection of two medias with dielectric constants ε_1 and ε_2 (See figure 2.4 for an illustrative example of these properties). In remote sensing of the earth this often occurs in the intersection between the atmosphere and the target.

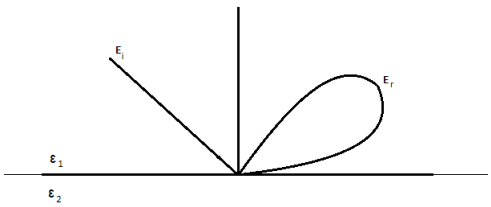

Figure 2.4: Illustration of surface scattering. E represents the EM radiation, subscript i indicates incident, subscript r indicates reflected.

The simplest form of surface scattering happens when the surface is very smooth compared to the incident wavelength, i.e. $\lambda >>$ interface roughness [14]. When this happens, scattering occurs only in the specular direction, i.e. for remote sensing purposes where an active sensor is used, no signal is received for these surfaces. This special case of scattering is illustrated in figure 2.5

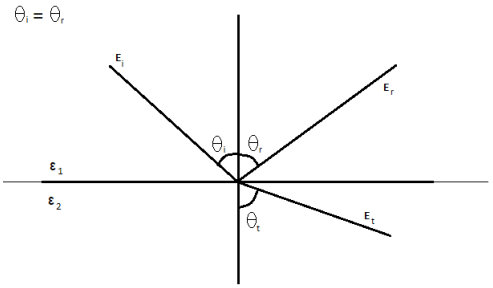

Figure 2.5: Illustration of the scattering from very smooth surface compared to incident wavelength. Subscript i indicates incidence, subscript t indicates transmitted, subscript r indicates reflected.

Snell's law can be utilized to describe the reflected energy and the reflectivity:

$$n_1 sin\theta_i = n_2 sin\theta_t \tag{2.6}$$

where $n_r = \sqrt{\varepsilon_r}$ is the refractive index, given by the Maxwell relation [9], ε_r is the permittivity, $r = 1, 2$, θ_i is the incident angle and θ_t is the transmission angle.

Furthermore, "as a smooth infinite plane interface causes zero crosspolarization" [9] the resulting reflected parameters only consist of copolarized channels, i.e. HH and VV. The resulting reflection matrix given by Fresnel equations then becomes:

$$\begin{bmatrix} R_{HH} & 0 \\ 0 & R_{VV} \end{bmatrix} \tag{2.7}$$

where

$$R_{HH} = \frac{n_1 cos\theta_i - n_2 cos\theta_t}{n_1 cos\theta_i + n_2 cos\theta_t} \tag{2.8}$$

and

$$R_{VV} = \frac{n_2 cos\theta_i - n_1 cos\theta_t}{n_2 cos\theta_i + n_1 cos\theta_t} \tag{2.9}$$

The reflection coefficients are often written in terms of θ_i and ε_2. The Fresnel equations forms the basis for every derivation of the scattering processes.

The derivation stated in equation 2.6 - 2.9 holds for smooth surfaces. However, in most cases the surface is not smooth, and the geometrical properties of the surface alters the relationship between the incident and reflected wave. The surface roughness describes the surface geometrical shape, and is often categorized as smooth, slightly rough, and very rough.

Mathematically, the surface roughness is the root mean square of the actual surface deviation from the averaged surface of the scene [14]. By making the surface illuminated by the sensor finite, or the incoming wave is made finite, the scattering no longer happens in only the Fresnel reflection direction. The main part of the backscattered energy still happens in the Fresnel direction, but the backscattered energy is now distributed in a lobe (see figure 2.6). The lobes extent and physical qualities can be calculated, and is called the coherent component. When the surface roughness increase energy is reflected in the incoherent component of the scattered field. The commonly used criteria for deciding if a surface is smooth or rough is the Rayleigh criterion. According to the Rayleigh criterion a surface is rough if the root mean square (r.m.s) height $> \lambda/8cos\theta_i$ [14]. If the surface is very rough the backscattering tends to happen equally in all directions, following an Lambertian surface. In this case the backscattered energy includes all polarizations.

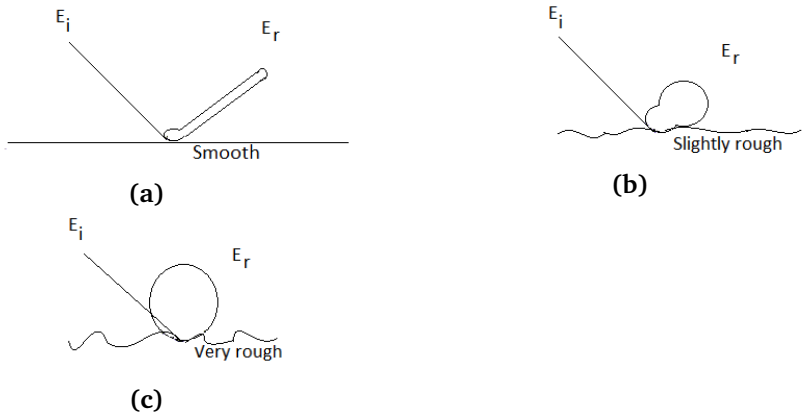

Figure 2.6: Illustration of surface scattering from (a) smooth, (b) slightly rough and (c) very rough surface.

In general, the rougher the surface, the diffuser the backscatter (See figure 2.6). How much of the signal that is scattered other than in the Fresnel reflection direction is dependent on the surface roughness relative to the wavelength of the incident wave [14]. For radar purposes the surface backscatter cross section is of importance. It describes how much of the backscattered energy that propagates towards the sensor and is defined as the ratio between energy received and energy that would have been received if the surface was isotropic [14]. It is given by the expression $\sigma = 10log_{10}(energyratio)[dB]$.

2.4.2 Double bounce

Double bounce scattering occurs when the incident signal interferes with two surfaces before returning (see figure 2.7). The simplest form of double bounce scattering can be illustrated with dihedral retro-reflection [9], commonly known as corner reflectors. Dihedral retro-reflectors consists of two surfaces of which the incoming wave interacts with, at 90 ° to each other. The wave hits one surface before being reflected to the other and returns away from the medium. For smooth surfaces the polarization of the backscattered signal is only in the co-polarized channels, where the HH channel remains unchanged, while the VV channel undergoes a 180 ° phase shift [9]. Double bounce can occur when there exist a rapid change in geometry in the illuminated scene, such as a flat smooth surface and an elevated area. Large scale roughness and elevation of the scene can depolarize the backscattered signal.

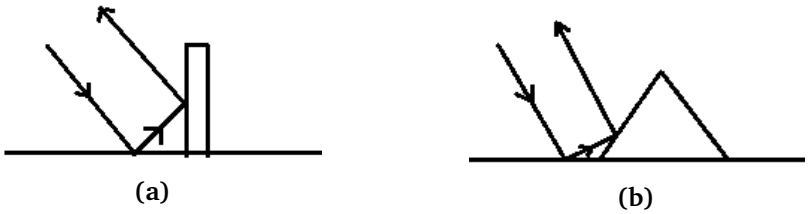

Figure 2.7: Illustration of double bounce scattering from (a) perpendicular surfaces, (b) elevated area not perpendicular.

2.4.3 Volume scattering

Volume scattering occurs when there exists variation in the dielectric properties of a medium [9], i.e. when the medium consists of different constituents. Also the incoming signal has to penetrate the medium in a significant amount for volume scattering to occur. The penetration depth is dependent on the frequency of the incoming radiation and the relative permitivity of the medium.

Volume scattering is different from surface scattering and double bounce scattering in the way that it happens inside of the medium. The scenario can be illustrated as in figure 2.8.

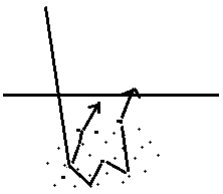

Figure 2.8: Illustration of volume scattering.

2.5 Noise

In all radar products noise and noise-like effects are apparent. It is of uttermost importance to be able to handle these effects and be aware of the underlying theory when working with SAR data.

Noise can be divided into two subsets; multiplicative and additive noise. Additive noise is the type which appears because of physical limitations of the imaging system such as thermal noise. Additive noise is the known noise, and often arise in the sensor itself. Most of the additive noise is produced because of thermal processes in the sensor, and can be treated as Gaussian distributions producing white noise. Reduction of additive noise can be done by either reducing the noise in the aperture or by increasing the power of the signal [16].

Multiplicative noise is the type which appears within the physical system, and are dependent on a variable. One form of multiplicative noise-like disturbance is speckle. Speckle is present in all coherent imaging systems and causes a spurious variation in pixel intensities, seen in images as salt and

pepper noise [28]. Speckle is constructed when the surface is rough compared to the wavelength and the returned signal consists of waves reflected from many elementary scatterers within a resolution cell. This in turn implies a possibility of difference in the phases of the reflected waves from the elementary scatterers, causing a destructing effect of the returned signal if out of phase, and a constructing effect if the waves have similar phases. Because there exists a number of elementary scatterers in one resolution cell and because of the presence of speckle, using a single pixel intensity to measure a targets reflectivity would be erroneous [28]. Speckle is considered as multiplicative noise-like disturbance, as it is dependent on the state of the system. It can be understood as an external source of noise, i.e. not coming from the sensor itself. Mathematically modeling this situation can be done by considering a stochastic differential equation. In the case of speckle theory this can be done with the Rayleigh speckle model for SLC (single look complex) SAR data, which under 3 assumptions leads to a ratio between the standard deviation and the mean being independent of the standard deviation, a basic characteristic of multiplicative noise, that also holds for multi-look processed SAR data [28]. Although mentioned here, speckle is said to be noiselike, and not actual noise. The measurements containing speckle are real measurements used in fields such as SAR interferometry [42].
A mathematical representation of the speckle production can be stated as:

$$Ae^{i\phi} = \sum_{k=1}^{N} A_k e^{i\phi_k} \tag{2.10}$$

where A is amplitude, and ϕ is the phase, and N is the number of elementary scatterers.

Speckle reduction in SAR imaging processing is often done by multi-looking a SLC image. A local averaging over a neighboorhod of single-look processed pixels are done to obtain a multi-looked image [28].

2.6 Radar cross section

The radar cross section (RCS) is a ratio describing the detectability of an object, where a bigger radar cross section answers to a more detectable object. The radar cross section is a measurement based on a hypothetical sphere, re-radiating the incoming EM wave such that the actual radiation measured at the radar is produced. It is therefore not a perfect replica of the actual scene, but the output is still the same [5].

Mathematically the RCS can be expressed as:

$$\sigma = \frac{I_{recieved}}{I_{incident}} 4\pi R^2 \tag{2.11}$$

Where R is the range, and I is intensity [52].
Parameters from the system such as wavelength, polarization, orientation of the landscape and depression angle are all important when it comes to the backscattering [5]. Also properties of the imaged scene is important, such as roughness of the surface, moisture, vegetation and microtopography [5]. Making the area of illumination (O) bigger increases the RCS. Therefore a more generalized expression should be used, namely the normalized backscatter coefficient:

$$\sigma_0 = \frac{\sigma}{O} \tag{2.12}$$

[52] Also called sigma nought, differential radar cross-section or normalized radar cross-section (NRCS). The NRCS is a unitless measure, and are therefore a measure of the target properties, and not the geometric properties. As it is not always easy to know how big O is as the geometry of the ground is everchanging for different scenes, NRCS is often re-written to:

$$\sigma_0 = \frac{\beta_0}{sin(\theta_i)} \tag{2.13}$$

Where β_0 is the radar brightness.

For a volume:

$$\sigma_0^{Volume} = pcos(\theta_i) \tag{2.14}$$

Where p is a constant describing the targets properties. When θ_i increases, σ_0^{Volume} decreases. To avoid dependency on incidence angle a new constant (γ) is defined which also describes volume scattering:

$$\gamma = \frac{\sigma_0}{cos(\theta_i)} \tag{2.15}$$

The NESZ is often used in context with noise. It is the estimation of the radar cross section which would answer to a signal to noise (SNR) ratio equal to 1, i.e. 50 % signal and 50 % noise in the backscattered signal [4]. If the signal contains 50 % noise it lies on the NESZ.

3

Data set and study site

This chapter introduces the satellite utilized for collection of data used in this thesis, the study area, and the data utilized. The thesis utilizes fine quad-polarimetric data for interpretation of polarimetric features and emulation of a dual-polarimetric product and knowledge about the data itself, how it was collected and where it was collected is important as all findings presented in the thesis builds upon this data.

3.1 RADARSAT-2

RADARSAT-2 is a satellite mission funded by the CSA (Canadian Space Agency) and MDA (MacDonald Dettwiler Associates Ltd. of Richmond, DC), launched in December 2007. It had an expected life span of 7 years, but is still operational (April 4th 2018). RADARSAT-2 is a follow up mission from RADARSAT-1, that stopped collecting data in March 2013 [15]. RADARSAT-2 contains a SAR instrument which can be utilized in different imaging modes. The imaging modes for quad-polarimetric- and dual-polarimetric data (see section 2.3) are illustrated in figure 3.1, where the red boxes are placed to show what imaging modes that are used in this study.
The spatial resolution of the data lies within the range of 3-100 meters, depending on the imaging mode selected. RADARSAT-2 is a fully polarimetric SAR satellite, and can therefore deliver quad-polarimetric data.

The imaging frequency is found in the C-band, more concrete at 5.405 GHz (5.5465764 cm).

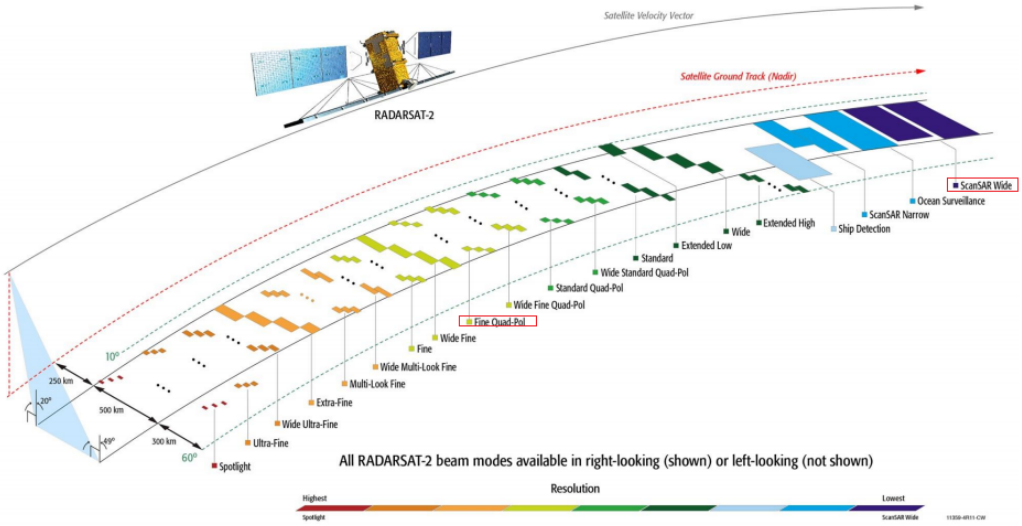

Figure 3.1: Overview of imaging modes, modified from [29].

RADARSAT-2 is equipped with yaw steering, such that there is zero doppler shift at the beam center, and it can look to the left or the right of the flightpath. The right-looking configuration was used for the collection of data utilized in the thesis.

3.2 Study area

The data used in this thesis was acquired November 28th 2017 at 02.55 UTC and are located in the Barents Sea. The Barents Sea is the area of the Arctic with the steepest change of sea ice extent, with an annual maximum extent in April, and minimum extent in September [33]. It is also the area of the Arctic where the time period of melting varies the most [6]. The Barents Sea is relatively shallow, with an average depth of 230m [41].

On the west side of the Barents Sea the northwestern boundary of the Norwegian Sea is located, ranging from the southernmost point of West Spitzbergen to North Cape ($25°45'E$). The northwestern boundary is located on the eastern shore of West Spitzbergen, up to $80°N$ to Cape Leigh Smith $80°05'N$,$65°10'E$. The northern boundary stretches through Cape Leigh Smith through Bolshoy Ostrov, Gilles and Victoria, Cape Mary Harmsworth, the northern coast of Franz-Josef Land to Cape Kohlsaat at $81°14'N$, $65°10'E$. The eastern boundary con-

tinues from Cape Kohlsaat through Cape Zhelaniya, west and southwest coast of Novaya Zemlya, Cape Kussov Noss, Dolgaya Bay at $70°15'N$, $58°25'E$, to Cape Greben and finally Cape Belyi Noss. The southern boundary is located between Svyatoi Nos on $39°47'E$ to Cape Kanin [22]. Because of its location the Barents Sea is affected by both the Arctic water and the Atlantic water, meaning that the Atlantic water will provide a warm front towards the Barents Sea [26]. The sea ice thickness varies greatly on a year to year basis, depending on outer effects such as the amount of sea ice drifting in from the Arctic basin, causing thick multi-year ice to be apparent as opposed to the thin ice visible from in-situ growth [26]. The satellite data used here primarily consists of thin ice and open water. An oil platform is also apparent in the images, with a location outlined in figure 3.3. The location of the imaged scene is shown in figure 3.2, and the σ_0 calibrated and speckle reduced intensity images is shown in figure 3.3.

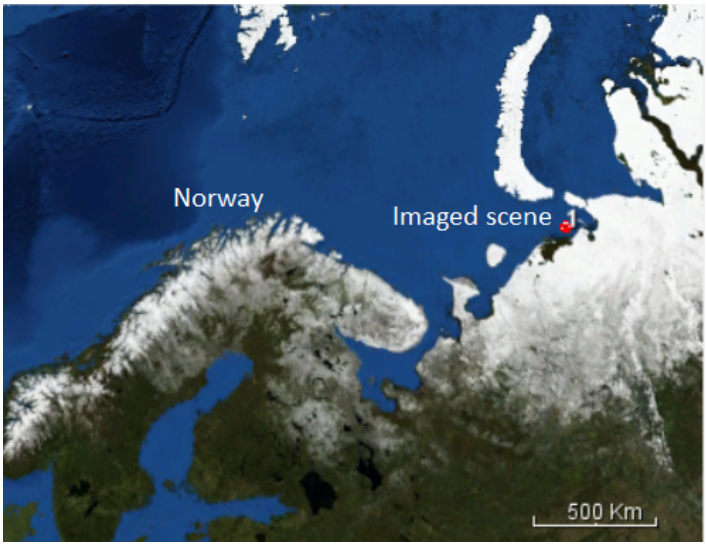

(a)

(b)

Figure 3.2: (a) Location of the imaged scene from November 28th 2017, (b) zoomed in location.

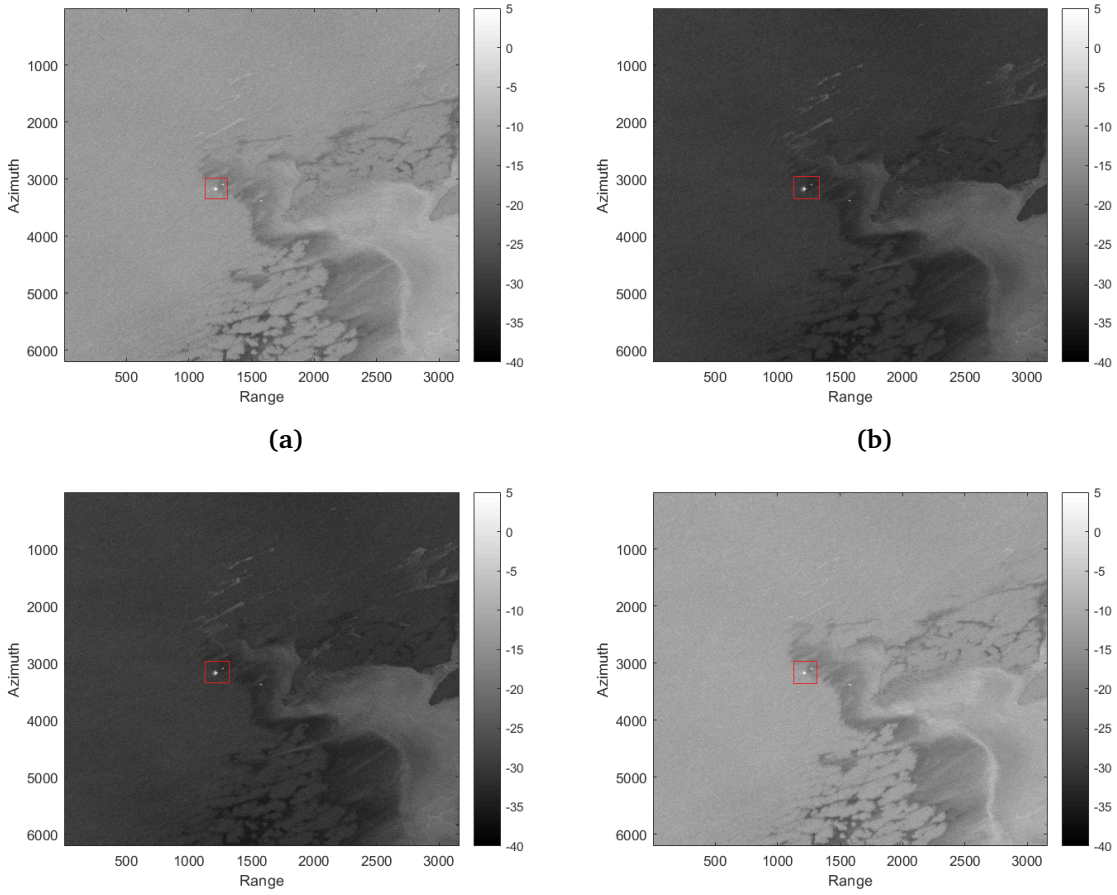

Figure 3.3: Speckle reduced σ_0 calibrated intensity images in dB of the entire scene, from November 28th 2017. (a) HH channel, (b) HV channel, (c) VH channel, (d) VV channel.

3.3 Quad-polarimetric SAR data

The thesis aims to investigate similarities and dissimilarities between a quad-polarimetric scene and an emulated dual-polarimetric scene. The emulation of the dual-polarimetric data is done to meet the parameters for ScanSAR Wide A (SCWA) products. Parameters for Fine quad-polarimetric (FQ13) products and SCWA are presented in table 3.1, found in [30], while the beam specific parameters for the available data is presented in table 3.2.

Parameter		
Beam mode	Fine Quad-Pol	SCWA
Channels	HH, HV, VH, VV	HH/HV or VV/VH or HH or HV or VH or VV
Pixel spacing	4.7 m × 5.1 m	50 m × 50 m
Resolution	5.2 m × 7.6 m	163–73 m × 78-106 m
Scene size	25 km × 25 km	500 km × 500 km
Incidence angle near	18°	20°
Incidence angle far	49°	49°

Table 3.1: Parameters for RADARSAT-2 data utilized.

Parameter	
Beam	FQ13
Incidence angle near	32.44°
Incidence angle far	34.08°

Table 3.2: Beam specific parameters for RADARSAT-2 data utilized.

4

Sea ice

The Arctic Ocean is covered with sea ice throughout the year, though the extent and thickness varies. Overall the yearly maximum areal extent is in March, and the yearly minimum areal extent is in September. In the Barents Sea however the annual maximum extent is in April, and the minimum extent is in September. The Arctic sea ice reflects incoming radiation, that otherwise would have been absorbed by the ocean, which would result in an overall higher ocean temperature and possibly altering the current flow in the ocean. Over the last years climatic changes have caused the amount of Arctic sea ice to decrease, and remote sensing of the Arctic sea ice is therefore important, to deliver evidence and surveillance of the everchanging landscape [36]. Such evidences have shown that the Arctic sea ice has decreased with 11 % per decade for September since the start of continuous and valid sensing started in 1979 (Passive microwave). Before 1979 the data collected was more unevenly spread in time and not that precise, but the trend over a 100 year period is apparent, showing a decrease of Arctic sea ice extent [36]. When sea ice melts and an ice sheet breaks into two, the water between the newly formed sheets heats up, causing Arctic amplification. For the water to freeze again heat has to be released into the atmosphere. The amount of sea ice in Arctic regions can affect shipping traffic, tourism and oil extraction. How the decrease of Arctic sea ice affects these aspects is not yet fully understood [36].

4.1 SAR imaging of sea ice

The backscatter from sea ice depends on a variety of factors. As for all radar imaging the wavelength, incidence angle, polarization and the shape, geometric properties, and physical properties of the backscattering elements is important. To better understand the nature of the backscattered wave, underlying theory of constituents in the imaged scene should be discussed, in particular snow and ice. Salinity and brine is presented prior to snow and ice, as it is an important feature in the discussion. The imaged scene consists of thin sea ice and open water, and ice formation is therefore an important aspect of the thesis.

4.2 Ice formation

Sea ice can form in many ways, leading to different properties that the radar are able to differentiate. It is therefore important to know about the processes of which sea ice is made from, and what characterizes these processes.

When saltwater in the ocean starts freezing small crystal structures forms. These structures are called frazil and are normally 3-4 mm wide. In the production of these frazils salt is pushed out of the structure. Frazils are therefore almost only consisting of fresh water [37]. As these structures merges together floes of new ice is formed. This can be done in different ways. The structures that can be expected in the data utilized in this thesis is presented:

- Grease ice: Grease ice forms in relatively calm waters, and has an appearance that looks like oil slicks. It has a matt appearance in radar images, as it does not reflect much radiation [50]. Further grease ice can form ice sheets called nilas. Nilas is thin, and are often viewed as dark objects in a radar image. These thin layers of ice can float underneath one another undergoing a process known as rafting or in a interlocking manner, where parts of the ice layers goes over and under eachother, in a pattern known as finger rafting [48]. Continuous freezing causes congelation ice to grow, forming a thicker ice sheet. The formation of ice crystals now happens in a slower manner, causing the ice crystals to have a different shape than frazil ice crystals. These crystal structures are called congelation ice crystals.

- Ice rind: Ice rind is normally not thicker than 5 cm, and are formed in calm waters by direct freezing or grease ice [48].

- Pancake ice: Pancake ice is normally 30cm-3m in diameter, with a maximum thickness of about 10 cm. Often pancake ice have an elevated

boundary, as an effect of bumping into other ice (see figure 4.1). Pancake ice can be formed by grease ice, shuga or slush, breaking of ice rind, nilas or motion of waves connecting grey ice [48].

Grease ice and pancake ice is shown in figure 4.1.

(a) **(b)**

Figure 4.1: (a) Grease ice. Image credit: Malin Johansson, UiT The Arctic University of Norway (b) Pancake ice. Image credit: Leif Eriksson Chalmers

4.2.1 Salinity and brine of sea ice

- Salinity: In chemistry parts per thousand is often used to define the amount of a constituent in a mass. For sea ice however, practical salinity units (psu) is widely used. In sea ice the average salinity lies within 32-37 psu, and for polar sea ice it can be less than 30 psu. The freezingpoint of sea water decreases with the increase of salinity. For every 5 parts per thousand the freezing point is reduced with 0.28 degrees celsius, resulting in an average freezingpoint of sea water in polar regions at -1.8 degrees celcius [38].

- Brine: The salt that is pushed out when frazil is produced is called brine and has the shape of a droplet. Most of these droplets are found at the near-surface water, raising the salinity of the near laying water. However, some of the droplets is trapped in pockets between the ice crystals. After time these droplets gets pushed out, resulting in air pockets inside the ice [38].

As salt affects the weight of the water it is an important constituent when it comes to ocean circulation. When brine is released into the ocean the salinity increases, causing the water to sink, and thereby affecting the circulation

[38].

4.2.2 Ice and Snow

As water freezes the dielectric constant decreases, making it almost transparent for microwaves, as opposed to water that has a high dielectric constant. As there might be numerous layers consisting of snow, ice, water, salt, and air bubbles, the backscattered signal can be formed by scattering from the upper boundary, the layers, or the boundaries between the layers [52]. The amount of backscatter from each of these physical geometries are highly dependent on the roughness of the surface [43] and the dielectric constant, where the dielectric constant is highly dependent on the water content. Backscatter from layers of ice and snow is considered as volume scattering, and therefore tend to scatter equally in all directions [52].

- Snow: Snow can be categorized as wet or dry. Dry snow has a low dielectric constant as it does not contain much liquid water, implying that it will only affect high microwave frequencies, acting as volume scattering. In wet snow water droplets are apparent between the ice structures in the snow, affecting the absorption of incoming radiation [43]. The thickness of the snowlayer and the variation of ice crystal size also affects the dielectric properties, and emissivity and scattering is therefore also dependent on these factors [52].

- Freshwater ice: As water freezes the rotational states of the molecules decreases, making the medium close to or a homogeneous medium, i.e. it will have a low dielectric constant [52]. This in turn increases the penetration depth, and as an example C-band microwaves can penetrate approximately 10 meters into the medium [52]. Because of this, microwaves will penetrate the ice and sense the boundary or the next layer underneath the ice. Depending on the geometry of the boundary, scattering direction can be decided. Often this boundary is smooth, resulting in a specular reflection of the scattering [52].

- Sea ice: Sea ice does not only contain water and air bubbles, but also salt. The salt content in sea ice affects the dielectric constant, and brine, salt and air pockets can be as much as 5-20 % of the sea ice volume. The dielectric properties of the ice is strongly dependent on the age of the ice, normally cathegorized as young ice, first year ice and multi year ice. Young ice is normally 10-30 cm thick, and are the ice between the ice formation processes and first year ice. First year ice is 30cm-2m thick, and are defined as sea ice that has gone through less than on winters growth [48]. Multi-year ice is at least 3m thick, and has gone through

at least two summers. Multi-year ice has undergone metamorphism and disposed itself of much salt [48].

Typically new ice (ice that is still in the formation process and <0.3 m thick), first year ice (0.3-2m thick) and multiyear ice (>2m thick) all have different brightness temperature and scattering properties. As new ice and first year ice has not gone through metamorphism it contains more salt and has a higher salinity than multi-year ice. In addition, water can spray the ice, causing potential snow to be saturated with salt water.

As an illustrative example, first year ice normally have a salinity content of 0.5-1.6 % at the surface, 0.4-0.5 % in the bulk, and 3 % near the lower boundary of the ice sheet. Multi-year ice that has undergone desalination will have a profile of less than 0.1 % at the upper boundary, and 0.2-0.3 % in the rest of the ice [52].

A higher salinity implies more absorption of incoming radiation, and therefore less radiation is scattered. However, higher salinity also implies a higher emission. The desalinated ice contains brine and air pockets, acting as dielectric discontinuities, and desalinated ice acts as a volume scatterer, depending on the contribution of these pockets. Typically, multi year ice does not have a great impact from temperature changes under 5 degrees Celsius because "penetration through the top 10 to 20 cm is the minimum required to produce a multi-year-ice-like response" [43]. The contribution is determined on a basis of the size of the pockets compared to the wavelength, the thickness of the layers and the volume fraction. Both frequency and polarization is important at the boundaries between different ice types or open water. As an example, for positive measurements the oceans emissivity is high and increasing as frequency is increased for H and V, while for multi-year ice, emissivity is decreasing with increasing frequencies [52].

4.3 Discrimination of sea ice in radar images

The scattering of EM signals on sea ice usually happens in one of two ways; surface scattering or volume scattering. Surface scattering usually occurs on thin, young sea ice where the geometrical properties are not changed, such as could be the case if rafting has occurred [11]. In intensity images these areas appear dark as the scattering happens in the specular direction (see 2.4). When the temperature decreases frost flowers starts growing. These features consists of ice crystals and roughens the surface of the sea ice. When frost flowers occurs at thin, young sea ice the received backscatter increases, making the

surface bright in the intensity image for C-band frequencies. Volume scattering occurs when the incoming radiation penetrates into the sea ice and meets discontinuities within the ice body[11]. When the sea ice is growing the salt is pushed out, leaving air bubbles that causes volume scattering. When sea ice forms and the thickness increases from 0-10 cm the difference in backscattered intensity usually lies within 5-10 dB as an effect of volume scattering [40]. The phase information found in SAR imaging can also be utilized for discrimination of sea ice, as thin newly formed ice yields phase difference between the HH and VV channel, while older ice yields no phase difference between these two channels [11]. The HH channel is often used when separation of sea ice and open water is preferred, as it is less affected by waves and irregularities of the open water than the VV channel. The co-polarization channels are also normally less affected by noise than the cross-polarization channels [11]. The cross-polarization channels is however when the noise allows it better suited for separation of ice with different surface geometry. The combination of the HH and the HV channels is often used for separating multi-year ice in first-year ice and separating sea ice and open water [11]. The incidence angle can also affect the separation of sea ice, but is not discussed here as the data used in the thesis covers a low range of incidence angles.

Sea ice can be classified as thin sea ice, first-year ice and multi-year ice, i.e. thin sea ice is newly formed sea ice. In microwave remote sensing thin sea ice can be challenging to classify as the backscatter and the polarization of the backscatter vary [20]. Many methods have been constructed to separate different sea ice types for both single-polarimetric (e.g. [27],[51]) and multi-polarimetric data (e.g. [20], [54]). Multi-polarimetric data can utilize backscattering in different polarization channels, enabling a more thorough analysis of the data and can help discriminate sea ice types including polarization difference [39] and co-polarization ratio [20] (see section 6.3). In addition thin sea ice normally has a dark appearance in SAR images [3].

5

Background theory

The results presented in the thesis requires knowledge about the polarimetric features used, and how to obtain those. Further, as dual-polarimetric data is simulated in this thesis the NESZ has to be adjusted accordingly. The chapter introduces the scattering matrix that leads to target vectors used to obtain the covariance and the coherency matrix. An explanation of the scattering matrix used for a dual-polarimetric system consisting of channels HH and HV is introduced, before the theory utilized for NESZ adjustment is presented.

5.1 Scattering matrix

The scattering matrix describes how the incident wave is scattered, and the relationship of the incident and scattered waves, given the Jones vectors is:

$$\underline{E}_S = \frac{e^{-jkr}}{r} S \underline{E}_I \tag{5.1}$$

The relationship holds for far field zones, where $\underline{E}_S$ is the scattered wave, $\underline{E}_I$ is the incident wave, r is the distance from the target and the sensor, k is the

wave vector, and S is the complex scattering matrix given as [28]

$$S = \begin{bmatrix} S_{11} & S_{12} \\ S_{21} & S_{22} \end{bmatrix} \tag{5.2}$$

In a Cartesian coordinate system the scattering matrix can be written as:

$$S_{(\hat{x},\hat{y})} = \begin{bmatrix} S_{XX} & S_{XY} \\ S_{YX} & S_{YY} \end{bmatrix} \tag{5.3}$$

and in the horizontal-vertical coordinate system:

$$S_{(\hat{u}_H,\hat{u}_V)} = \begin{bmatrix} S_{HH} & S_{HV} \\ S_{VH} & S_{VV} \end{bmatrix} \tag{5.4}$$

The diagonal of the scattering matrix is referred to as the co-polarization elements, while the off diagonal elements is referred to as the cross-polarization elements [28]. Note that for a quad-polarimetric system all of the elements in the scattering matrix is utilized, while for a dual-polarimetric system only two channels are available, and elements in the scattering matrix becomes zero.

For a dual-polarimetric system where the HH and HV channels are used the scattering matrix reduces to:

$$S_{(\hat{u}_H,\hat{u}_V)} = \begin{bmatrix} S_{HH} & S_{HV} \\ 0 & 0 \end{bmatrix} \tag{5.5}$$

5.2 Scattering target vector

Extraction of physical information such as H and $\bar{\alpha}$ angles are found through system vectors known as scattering target vectors. These vectors are constructed from the scattering matrix in the following manner:

$$k = V(S) = \frac{1}{2} Tr(S\Psi) \tag{5.6}$$

[28]
Where V represents a vector, Tr is the trace, and Ψ is a matrix basis set.

The Lexicographic matrix basis set (Ψ_L) and the complex Pauli spin matrix basis set (Ψ_P) are two matrix basis sets commonly used, as they form target vectors used to obtain the covariance- (section 5.3) and the coherency matrix (section 5.4) respectively. Ψ_L and Ψ_P is given by:

$$\Psi_L = 2\begin{bmatrix}1 & 0\\ 0 & 0\end{bmatrix} 2\begin{bmatrix}0 & 1\\ 0 & 0\end{bmatrix} 2\begin{bmatrix}0 & 0\\ 1 & 0\end{bmatrix} 2\begin{bmatrix}0 & 0\\ 0 & 1\end{bmatrix} \tag{5.7}$$

and

$$\Psi_P = \sqrt{2}\begin{bmatrix}1 & 0\\ 0 & 1\end{bmatrix} \sqrt{2}\begin{bmatrix}1 & 0\\ 0 & -1\end{bmatrix} \sqrt{2}\begin{bmatrix}0 & 1\\ 1 & 0\end{bmatrix} \sqrt{2}\begin{bmatrix}0 & -j\\ j & 0\end{bmatrix} \tag{5.8}$$

The different matrices in the Pauli decomposition each represents different scattering mechanisms; Single or odd-bounce scattering from a surface (matrix 1), diplane scattering (double or even-bounce scattering) (matrices 2 and 3) and antisymmetric components (matrix 4) [28].

5.3 Covariance matrix

The 3-dimensional covariance matrix (C_3) is obtained through a Lexicographic target vector (k_L). The Lexicographic target vector can be found through Ψ_L. Often the HV and VH channel deliver close to identical information. In these cases reciprocity is assumed. Given reciprocity Ψ_L can be written as [28]:

$$\Psi_L = 2\begin{bmatrix}1 & 0\\ 0 & 0\end{bmatrix} 2\sqrt{2}\begin{bmatrix}0 & 1\\ 0 & 0\end{bmatrix} 2\begin{bmatrix}0 & 0\\ 0 & 1\end{bmatrix} \tag{5.9}$$

The resulting Lexicographic target vector, through equation 5.6 becomes:

$$k_L = \begin{bmatrix} S_{HH} \\ \sqrt{2}S_{XY} \\ S_{VV} \end{bmatrix} \tag{5.10}$$

Where S_{XY} is either S_{HV} or S_{VH}.

The 3-dimensional covariance matrix can then be found by the outer product of

the target vector times the complex conjugate of the transpose of itself:

$$C_3 = \langle k_L k_L^{*T} \rangle \tag{5.11}$$

where $*$ means the complex conjugate, T means transpose, and $\langle\rangle$ is averaging.

The resulting 3-dimensional covariance matrix then becomes:

$$C_3 = \begin{bmatrix} \langle |S_{HH}|^2 \rangle & \sqrt{2}\langle S_{HH} + S_{XY}^* \rangle & \langle S_{HH} + S_{VV}^* \rangle \\ \sqrt{2}\langle S_{XY} S_{HH}^* \rangle & 2\langle |S_{XY}|^2 \rangle & \sqrt{2}\langle S_{XY} S_{VV}^* \rangle \\ \langle S_{VV} S_{HH}^* \rangle & \sqrt{2}\langle S_{VV} S_{XY}^* \rangle & \langle |S_{VV}|^2 \rangle \end{bmatrix} \tag{5.12}$$

5.4 Coherency matrix

The coherency matrix lays the ground for investigation of polarimetric features and scattering properties for quad-polarimetric systems. The 3-dimensional coherency matrix (T_3) can be found through Ψ_P, which given reciprocity can be written as:

$$\Psi_P = \sqrt{2}\begin{bmatrix} 1 & 0 \\ 0 & 1 \end{bmatrix} \sqrt{2}\begin{bmatrix} 1 & 0 \\ 0 & -1 \end{bmatrix} \sqrt{2}\begin{bmatrix} 0 & 1 \\ 1 & 0 \end{bmatrix} \tag{5.13}$$

The resulting Pauli target vector, through equation 5.6 becomes:

$$k_P = \frac{1}{\sqrt{2}} \begin{bmatrix} S_{HH} + S_{VV} \\ S_{HH} - S_{VV} \\ 2S_{XY} \end{bmatrix} \tag{5.14}$$

The 3-dimensional coherency matrix (T_3) can then be found by the outer product of the target vector times the complex conjugate of the transpose of itself:

$$T_3 = \langle k_P k_P^{*T} \rangle \tag{5.15}$$

The resulting 3-dimensional coherency matrix then becomes:

$$T_3 = \frac{1}{2}\begin{bmatrix} \langle|S_{HH}+S_{VV}|^2\rangle & \langle(S_{HH}+S_{VV})(S_{HH}-S_{VV})^*\rangle & 2\langle(S_{HH}+S_{VV})S_{XY}^*\rangle \\ \langle(S_{HH}-S_{VV})(S_{HH}+S_{VV})^*\rangle & \langle|S_{HH}-S_{VV}|^2\rangle & 2\langle(S_{HH}-S_{VV})S_{XY}^*\rangle \\ 2\langle S_{XY}(S_{HH}+S_{VV})^*\rangle & 2\langle S_{XY}(S_{HH}-S_{VV})^*\rangle & 4\langle|S_{XY}|^2\rangle \end{bmatrix} \tag{5.16}$$

5.5 Decomposition of scattering matrix used for dual-polarimetric HH/HV

The coherency matrix can not be found for a dual-polarimetric HH/HV system, and the covariance matrix is therefore used instead. According to [28] the eigenvalues of a coherency matrix and a covariance matrix are the same, and the eigenvectors have a relation to each other. This relationship can be shown by the two expressions of the decompositions of the coherency and covariance matrices:

$$T_3 = U_P \Sigma_P U_P^{-1} \tag{5.17}$$

where U_P is a unitarian matrix with orthogonal eigenvectors of T_3, and Σ_P is a diagonal, nonnegative real matrix.

$$C_3 = U_C \Sigma_L U_C^{-1} \tag{5.18}$$

where U_C is a unitarian matrix with orthogonal eigenvectors of C_3, and Σ_C is a diagonal, nonnegative real matrix. [28]

By utilizing a Unitarian matrix ($U_{3(L-P)}$) that transforms Lexicographic to Pauli it can be shown that:

$$T_3 = U_P \Sigma_P U_P^{-1} = U_{3(L-P)} C_3 U_{3(L-P)}^{-1} \tag{5.19}$$

which is assumed to also hold for a dual-polarimetric system.
The target scattering vector for a dual-polarimetric HH/HV system can be

found by utilizing the general expression for obtaining the target vector (k) for compact-polarimetric and dual-polarimetric systems given in [46]:

$$k = \begin{bmatrix} cos(\chi)(cos(\theta_R)S_{HH} + sin(\theta_R)S_{HV}) + isin(\chi)(sin(\theta_R)S_{HH} - cos(\theta_R)S_{HV}) \\ cos(\chi)(cos(\theta_R)S_{VH} + sin(\theta_R)S_{VV}) + isin(\chi)(sin(\theta_R)S_{VH} - cos(\theta_R)S_{VV}) \end{bmatrix} \tag{5.20}$$

where χ is the ellipticity angle and θ_R is the roll angle.
Setting χ and θ_R to zero reveals that the target vector is:

$$k_L = \begin{bmatrix} S_{HH} \\ S_{HV} \end{bmatrix} \tag{5.21}$$

The covariance matrix (C_2) for the HH and HV channels becomes:

$$C_2 = \langle k_L k_L^{*T} \rangle = \begin{bmatrix} \langle |S_{HH}|^2 \rangle & \langle S_{HH} S_{HV}^* \rangle \\ \langle S_{HV} S_{HH}^* \rangle & \langle |S_{HV}|^2 \rangle \end{bmatrix} \tag{5.22}$$

The approach to obtain the target scattering vector used in this study secures that the power contained in the scattering vector holds for a dual-polarimetric system, while other approaches [23], use a SPAN consistent with quad-polarimetric data. The total power scattered is represented by the SPAN.

5.6 Additive noise

Additive noise is commonly interpreted as thermal noise, but can also rise from Analog-to-Digital conversion (both quantization and saturation), interference arising in the transponders, and ambiguities such as ghost images. Thermal noise and quantization noise is considered as white noise, i.e. having a circularly-symmetric Gaussian distribution with zero mean and constant spectral density for every bandwidth [18]. In addition it is assumed that the true scattering is completely uncorrelated with the noise term, and the noise term in different channels is uncorrelated with each other. A mathematical representation of the additive noise can be derived from the received signal matrix (M) in the following manner:

$$M = \begin{bmatrix} S_{HH} & S_{HV} \\ S_{VH} & S_{VV} \end{bmatrix} + \begin{bmatrix} n_{HH} & n_{HV} \\ n_{VH} & n_{VV} \end{bmatrix} = S + N \tag{5.23}$$

Where n_{ij} is the noise withheld in each polarization channel of the received signal matrix, and N is the noise matrix.
The properties of the noise arizing from thermal processes and quantization can be represented as:

$$\langle n_{ij} \rangle = 0 \tag{5.24}$$

$$\langle n_{ij} n_{ij}^* \rangle = \sigma_{ij}^n \tag{5.25}$$

Where σ_{ij}^n is the noise power (NESZ)

$$\langle n_{ij} n_{kl}^* \rangle = 0 \tag{5.26}$$

for $i \neq k$ and $j \neq l$.

$$\langle n_{ij} S_{kl}^* \rangle = 0 \tag{5.27}$$

for all i, j, k, l.

Adding white Gaussian noise to radar images can be done either directly at the SLC products, or in matrices where cross products are apparent, such as the coherency and the covariance matrix. If reciprocity is assumed, the covariance matrix is formed by the outer product of the lexicographic targetvector times its complex transpose ($\langle k_L k_L^{*T} \rangle$). The lexicographic targetvector is represented as:

$$k_L = \begin{bmatrix} (S_{HH} + n_{HH}) \\ \sqrt{2}(S_{XY} + n_{XY}) \\ (S_{VV} + n_{VV}) \end{bmatrix} \tag{5.28}$$

If S_{XY} is S_{HV} the covariance matrix becomes:

$$C_3 = \begin{bmatrix} \langle |S_{HH}|^2 + \sigma_{HH}^n \rangle & \sqrt{2}\langle S_{HH} + S_{HV}^* \rangle & \langle S_{HH} + S_{VV}^* \rangle \\ \sqrt{2}\langle S_{HV} S_{HH}^* \rangle & 2\langle |S_{HV}|^2 + \sigma_{HV}^n \rangle & \sqrt{2}\langle S_{HV} S_{VV}^* \rangle \\ \langle S_{VV} S_{HH}^* \rangle & \sqrt{2}\langle S_{VV} S_{HV}^* \rangle & \langle |S_{VV}|^2 + \sigma_{VV}^n \rangle \end{bmatrix} \tag{5.29}$$

Similarly, the coherency matrix is formed by the outer product of the Pauli targetvector times its complex transpose ($\langle k_P k_P^{*T} \rangle$), assuming reciprocity. The

Pauli targetvector is represented as [21]:

$$k_p = \begin{bmatrix} \frac{1}{\sqrt{2}} S_{HH} + S_{VV} + (n^n_{HH} + n^n_{VV}) \\ \frac{1}{\sqrt{2}} S_{HH} - S_{VV} + (n^n_{HH} - n^n_{VV}) \\ \frac{1}{\sqrt{2}} 2(S_{XY} + n^n_{XY}) \end{bmatrix} \tag{5.30}$$

If S_{XY} is S_{HV} the coherency matrix becomes [21]:

$$T_3 = \frac{1}{2} \begin{bmatrix} \langle |S_{HH} + S_{VV}|^2 + (\sigma^n_{HH} + \sigma^n_{VV}) \rangle & \langle (S_{HH} + S_{VV})(S_{HH} - S_{VV})^* \rangle & 2\langle (S_{HH} + S_{VV}) S^*_{HV} \rangle \\ \langle (S_{HH} - S_{VV})(S_{HH} + S_{VV})^* \rangle & \langle |S_{HH} - S_{VV}|^2 + (\sigma^n_{HH} - \sigma^n_{VV}) \rangle & 2\langle (S_{HH} - S_{VV}) S^*_{HV} \rangle \\ 2\langle S_{HV}(S_{HH} + S_{VV})^* \rangle & 2\langle S_{HV}(S_{HH} - S_{VV})^* \rangle & 4\langle (|S_{HV}|^2 + \sigma^n_{HV}) \rangle \end{bmatrix} \tag{5.31}$$

From the covariance- and coherency matrix it is clear that the additive noise only affects the diagonal, where the cross product of a given channel is made. If noise is added to simulate a certain situation such as change of an aperture it could be advantageous to add the noise directly on the covariance or coherency matrix. Generation of noise is done on the basis of a statistical distribution, which would yield different results in pixel values when done on SLC product separately, and the simulation of noise would have to be done a sufficient amount of times to obtain a respectable result.

6 Polarimetric features

Polarimetric features can be further divided into the subclasses multi-polarization features and single-polarization features. Multi-polarization features is obtained from polarimetric SAR systems utilizing more than one polarization channel. Polarimetric SAR deliver results in a variety of fields, based on information concerning surface geometry, roughness and dielectic properties. Through target decomposition multi-polarization features can be extracted. Widely used target decompositions include Krogager's decomposition, Cloude and Pottiers decomposition, Freeman and Durdens decomposition, Yamaguchis decomposition, Touzis decomposition, and Cameron and Rais decomposition [53]. In this thesis the cross-polarization ratio is found, and Cloude and Pottiers eigenvector and eigenvalue decomposition is used to obtain the multi-polarimetric features H and $\bar{\alpha}$. The cross-polarization ratio is often used as a complementary aid for classification of sea ice, while the H and $\bar{\alpha}$ is used to differentiate between different scattering mechanisms. The single-polarization feature damping ratio is also utilized in the thesis, a ratio that could classify sea ice in radar images. In addition, the co-polarization ratio is utilized to separate different constituents in the imaged scene.

6.1 Entropy and $\overline{\alpha}$-angle

α and H are polarimetric features that conventionally is obtained from the coherency matrix of a quad-polarimetric system [28]. α can be used to investigate

the scattering of the scene, while H describes the randomness of the scattering (i.e. it is also linked to the depolarization of the signal). α and H are independent of the statistical distribution, and can be found from the eigenvalues and eigenvectors of the coherency matrix. The eigenvalues and eigenvectors of the coherency matrix can be used to decompose the scattering. The coherency matrix is a hermitian positive semi-definite matrix, and it follows that it can be diagonalized by utilizing a unitary similarity transformation [32]:

$$[T] = [U][\Lambda][U]^{-1} = [T_1]+[T_2]+[T_3] = \lambda_1(e_1{e_1}^{*T})+\lambda_2(e_2{e_2}^{*T}) + \lambda_3(e_3{e_3}^{*T}) \quad (6.1)$$

Where Λ is the diagonal eigenvalue matrix consisting of real, non-zero eigenvalues, and U is the unitary eigenvector matrix, where the eigenvectors are orthonormal, and e is the eigenvectors.

By diagonalizing the coherency matrix of a distributed scatterer, decomposition into non-coherent coherency matrices is possible [32]. This leads to matrices of rank 1, each having a deterministic scattering contribution.
H can be gathered from the eigenvalues of the coherency matrix. It have the advantage that it is not changed because of the unitary transformation. This is because the scattering process have the same eigenvalues independent of the basis used, i.e. it is roll-invariant.
However, for the HH/HV dual-polarimetric data a covariance matrix is used to obtain H and $\bar{\alpha}$. The eigenvalues are the same for the covariance matrix as for the coherency matrix and the eigenvectors are related. However, the $\bar{\alpha}$ for a HH/HV dual-polarimetric system is not roll-invariant [1].

6.1.1 Entropy

H is a measure of the randomness of the scattering. It is a parameter that can be utilized to describe "the statistical disorder of each distinct scatter type within the ensemble" [28] and can be written as:

$$H = -\sum_{b=1}^{G} P_b log_G P_b \quad (6.2)$$

Where

$$P_b = \frac{\lambda_b}{\sum_{b=1}^{G} \lambda_b} \quad (6.3)$$

and G is the polarimetric dimension [28]. The eigenvalues of the coherency matrix is rotationally invariant, and it therefore follows that the H is roll-

invariant.

For a quad-polarimetric system this implies a H expressed as:

$$H = -\sum_{b=1}^{3} P_b log_3 P_b \tag{6.4}$$

and for a dual-polarimetric system:

$$H = -\sum_{b=1}^{2} P_b log_2 P_b \tag{6.5}$$

H can take values from 0 to 1, where 1 indicates complete randomness of the scattering. This happens when there exists more than one scatterer, and they are all contributing equally. The lesser the value of the H is, the less depolarization of the signal occurred. The extreme value of 0 indicates that there is only one non-zero eigenvalue, which means that there has not been any depolarization of the signal. For a fully polarimetric system there is only one scattering matrix describing the situation, i.e. λ_2 and λ_3 equals zero.

6.1.2 $\overline{\alpha}$-angle

$\bar{\alpha}$ is a parameter that gives an expression to what physical scattering mechanisms that are present in the image [28]. For a fully polarimetric system it is roll-invariant as the eigenvalues of the coherency matrix is rotationally invariant. It is expressed as:

$$\bar{\alpha} = \sum_{b=1}^{G} P_b \alpha_b \tag{6.6}$$

Where

$$0 \leq \bar{\alpha} \leq 90 \tag{6.7}$$

For a quad-polarimetric system: α_b can be derived from the eigenvectors, given

as:

$$e_b = \begin{bmatrix} cos(\alpha_b)e^{b\phi 1b} \\ sin(\alpha_b)cos(\beta_b)e^{b\phi 2b} \\ sin(\alpha_b)sin(\beta_b)e^{b\phi 3b} \end{bmatrix} \tag{6.8}$$

and

$$\alpha_b = arccos(|e_{1b}|) \tag{6.9}$$

Each α_b can in most cases correspond to different types of scattering, where $0 < \alpha_b < 30$ is surface scattering, $40 < \alpha_b < 50$ is dipol-like scattering, and $60 < \alpha_b < 90$ is dihedral scattering, which also holds for $\bar{\alpha}$ [32]. $\bar{\alpha}$ is low over ocean areas (indicating surface scattering), and differ over ice, depending on the age of the ice, structures and whether there exists snow on the surface or not.

For a dual-polarimetric system: The second eigenvector is orthogonal to the principal vector. α can therefore be derived from the principal eigenvector, given as:

$$e_1 = \begin{bmatrix} cos(\alpha_1) \\ sin(\alpha_1)e^{i\phi} \end{bmatrix} \tag{6.10}$$

[1]
and

$$\bar{\alpha} = P_1\alpha_1 + P_2(\frac{\pi}{2} - \alpha_1) \tag{6.11}$$

[1] and [10]

6.2 H/$\overline{\alpha}$-plot

A commonly used method for interpreting H and $\bar{\alpha}$ is to plot them together, with the $\bar{\alpha}$-angles on the y-axis, and H values on the x-axis. This representation presents a visual interpretation of the data, where the plot can be divided into 8 feasible and a not feasible region, enabling classification of all random scattering mechanisms [28]. The boundaries are not finite, and vary with factors such

as what constituents that are apparent in the scene. In the H/$\bar{\alpha}$-plot 8 regions are utilized to differ between scattering mechanisms, in addition to the non feasible region (3). Those are: Bragg surface (9), dipole (8), dihedral reflectors (7), random surface (6), anisotropic particles (5), double reflection propagation effects (4), random anisotropic scatterers (2), and complex structures (1). The regions can be seen in figure 6.1.

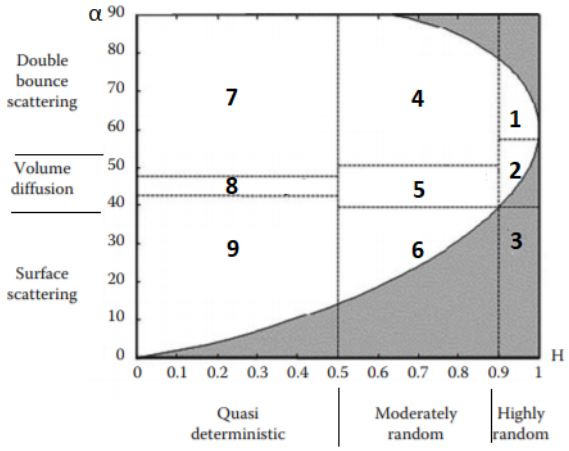

Figure 6.1: H/$\bar{\alpha}$-plot with regions. Modified from [28]

6.3 Co-polarization ratio

The co-polarization ratio requires a quad-polarimetric processor, and is in this thesis only used to prove evidence of the existence of open water and sea ice in the imaged scene. The co-polarization ratio is expressed differently in literature, some using the VV channel over the HH channel (e.g. [20]), some using the HH channel over the VV channel (e.g. [7]), some squaring the channels (e.g. [7]) and some taking caution to incidence angle (e.g. [3]). In this thesis the following expression for the co-polarization ratio is used:

$$R_{HH/VV} = \frac{\langle |S_{VV}| \rangle}{\langle |S_{HH}| \rangle} \tag{6.12}$$

[20]

The co-polarizarion ratio over sea ice varies with frequency of the signal. For C-band microwave remote sensing, as used in this thesis the co-polarization ratio over thin, young sea ice is low [7]. Other studies such as [55] and [24] found

that the co-polarization ratio decreases and approaches 0 dB with increasing thickness of young ice for C-band microwave remote sensing.

The co-polarization ratio can discriminate smooth surfaces well, as horizontally polarized waves will reflect from them while vertically polarized waves penetrates into the medium having a smooth surface. This can be shown by utilizing the Fresnel equations introduced in section 2.4.1 [20]. As a surface becomes rougher less backscattering is received in the HH channel, causing the co-polarization ratio to approach zero. The dielectric properties and the scattering mechanisms of open water (such as Bragg scattering) causes the co-polarization ratio to obtain positive values.

6.4 Cross-polarization ratio

The cross-polarization ratio for HH and HV channel is defined as:

$$R_{HV/HH} = \frac{\langle |S_{HV}| \rangle}{\langle |S_{HH}| \rangle} \tag{6.13}$$

It is a measure of the depolarization [13], which implies that the roughness of the scene and volume like scattering is important for the cross-polarization ratio. The cross-polarization ratio can be used for separation of multi-year ice and first-year ice, sea ice and open water, detection of icebergs, and ice age classification [47].

6.5 Damping ratio

The damping ratio utilizes the difference in backscatter from open water and a medium damping the capillary waves in the water and thereby reducing the amount of backscatter to classify constituents in the imaged scene. The radar backscatter over fluids is dependent on the waves, where high waves implicates more backscatter than low waves [25]. The damping ratio is often used for oil spill detection (e.g. [19], [17], [25]), as the oil dampens the waves, appearing dark in radar images. Although often used for oil spill detection these effects is also apparent in areas containing sea ice [44]. The damping ratio is found

by the following expression:

$$DR = \frac{\langle \sigma_{0,sea} \rangle}{\langle \sigma_{0,D} \rangle} \tag{6.14}$$

Where σ_0, sea is the mean backscatter from open water areas and σ_0, D is the mean backscatter from the damping medium.

7 Method

In this chapter the methods used to extract the results are explained. Much of what is presented builds upon chapter 5. The basic theory of calibration, multi-looking, NEZS adjustment, and emulation is are elaborated upon. In addition, methods for obtaining results in each case/step for the H, $\bar{\alpha}$ and the H/$\bar{\alpha}$-plot study, and the cross-polarization ratio and the damping ratio studies are presented. Calibration and multi-looking is performed on each case/step as it is for all studies of SAR data.

7.1 Calibration

Calibration is the first processing step when working with satellite data. Calibration of radar images are performed to convert measured values in the aperature into ground truth reflectivity [42]. The ultimate goal of calibration is to address issues relating to noise, azimuth processing, and the gain term. The gain comes from range antenna pattern, propagation and range compression [42]. The data is calibrated to contain its complexity:

$$calibrated\ value = \frac{digital\ value}{D} \tag{7.1}$$

where $digital\ value$ is the original values of the images given, and D is the gain.
The values for D is extracted from the LUT (Look-up tables) files given in the

metadata supplied with the satellite images. In this thesis the σ_0 values are used for calibration.

7.2 Multi-looking

Multi-looking is performed to reduce the amount of speckle in an image. For SLC data this is accomplished by averaging neighbouring pixels in azimuth direction. Additionally, a boxcar filter can be applied to remove more of the speckle [28]. The multi-looking is performed on the covariance and coherency matrices, and is delineated with a $\langle\rangle$. In the covariance and coherency matrices multi-looking is done by averaging. The averaging window used in this study is 7x7 pixels in size.

7.3 Adjustment of NESZ

When emulating dual-polarimetric data from quad-polarimetric data, the NESZ has to be adjusted accordingly. RADARSAT-2 deliver both quad-polarimetric and dual-polarimetric data, and the NESZ adjustment was, in this emulation, performed to meet the NESZ level of dual-polarimetric SCWA products. The NESZ for the quad-polarimetric data and the dual-polarimetric data, covering the incidence angles for the quad-polarimetric product is shown in figure 7.1.

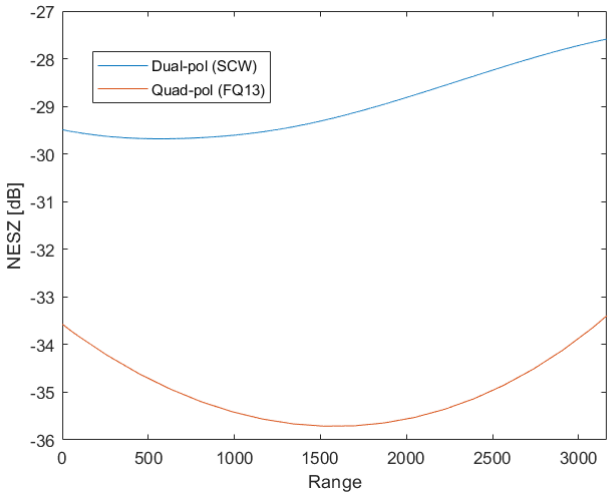

Figure 7.1: NESZ of quad-polarimetric FQ13 and dual-polarimetric SCWA data.

As seen in section 5.6 the crossproduct of noise in one polarization channel yields the NESZ. From the received signal matrix (the S matrix) both the covariance and coherency matrix can be found, and the NESZ is increased by adding white Gaussian noise with power equal to the difference in NESZ for each range position in these matrices.
The NESZ is obtained in dB and had to be transformed to linear values before being added to the SLC products, the covariance- or the coherency matrices. This was done in the following manner:

$$\sigma_{ij}^{n}(DP - QP) = 10^{NESZ_{DP}/10} - 10^{NESZ_{QP}/10} \tag{7.2}$$

Where $\sigma_{ij}^{n}(DP - QP)$ is the desired difference in linear domain, $NESZ_{DP}$ is the NESZ for the dual-polarimetric product in dB, and $NESZ_{QP}$ is the NESZ for the quad-polarimetric product in dB. For simplicity $\sigma_{ij}^{n}(QP)$ will be used as an abbreviation of the quad-polarimetric NESZ transformed from dB domain.

The new NESZ in the emulated products were found utilizing the following equation:

$$\sigma_{ij}^{n}(new) = \sigma_{ij}^{n}(QP) + \sigma_{ij}^{n}(DP - QP) \tag{7.3}$$

Where $\sigma_{ij}^{n}(new)$ is the new NESZ equal to that of a dual-polarimetric SCWA product.
Adjusting the NESZ leads to a change in the eigenvalues of the covariance- and coherency matrices. This implies a change in the results for polarimetric features such as H and $\bar{\alpha}$ (See Appendix).

7.4 Emulating dual-polarimetric data

The goal of the emulation is to obtain a product with pixel spacing, NESZ and polarization channels equal to an already existing dual-polarimetric product. The emulation of a complete dual-polarimetric product is, in this thesis, done in four steps:

- Averaging: Averaging is done with a simple averaging filter, which utilizes a mask defined as:

$$Av_{mask} = \frac{1}{m * n}[ones] \tag{7.4}$$

  where m and n defines the size of the mask. This thesis utilizes a mask of dimensions 7×7.

- Downsampling: The image is after being averaged downsampled according to the ratio between the pixel spacing for FQ13 and SCWA products in azimuth and range direction given in [29].

- Polarization channel reduction: The reduction of polarization channels is a straight forward process where two polarization channels are removed to obtain the same amount of polarization channels as a dual-polarimetric product. In this thesis dual-polarimetric HH/HV products are desired, and the VH and VV channels is therefore removed.

- NESZ adjustment: The NESZ was adjusted by adding the difference of the quad-polarimetric NESZ and the dual-polarimetric NESZ to the covariance matrix, the coherency matrix, and directly at the SLC products according to section 7.3 and 5.6.

7.5 Structure of the entropy, $\overline{\alpha}$ and H/$\overline{\alpha}$-plot study

Emulating dual-polarimetric from quad-polarimetric data is done to achieve an improved understanding of the information loss and to evaluate the reasons behind it. Generally dual-polarimetric data (i.e. data with two polarization channels) has a lower resolution than quad-polarimetric data and contains more additive noise. To evaluate each step in the emulation process and to gain knowledge of how the different steps alter the results, individual case studies are considered. For the study concerning the polarimetric features of H, $\bar{\alpha}$, and the H/$\bar{\alpha}$-plot the workflow is divided into 7 cases. An overview of these cases can be found in table 7.1.

Case 1	The data is kept as quad-polarimetric and the NESZ is adjusted in the covariance matrix.
Case 2	The data is kept as quad-polarimetric and the NESZ is adjusted in the coherency matrix.
Case 3	The data is kept as quad-polarimetric and the NESZ is adjusted on the SLC products before the coherency matrix is obtained.
Case 4	The data is downsampled and averaged to obtain dual-polarimetric resolution.
Case 5	The polarization channels are reduced from 4 to 2.
Case 6	The data is converted to dual-polarimetric by downsampling, averaging and reduction of polarization channels. The NESZ is kept constant.
Case 7	The data is converted to dual-polarimetric by downsampling, averaging and reduction of polarization channels before the NESZ is adjusted in the covariance matrix.

Table 7.1: Overview of cases in the H, $\bar{\alpha}$, and H/$\bar{\alpha}$-plot study.

Case 1-3 introduces NESZ adjustment on quad-polarimetric products, case 4-6 introduces the different steps used to obtain dual-polarimetric products without regard to the NESZ adjustment, and finally case 7 emulates a dual-polarimetric product with an adjusted NESZ.

7.6 Structure of the cross-polarization ratio and damping ratio studies

As in the H, $\bar{\alpha}$ and the H/$\bar{\alpha}$-plot study the workflow in the cross-polarization ratio and the damping ratio studies is devided into steps. These steps are the same for these studies and are presented in table 7.2. As the cross-polarization ratio requires the HH and the HV channels and the damping ratio only requires one polarization channel, reduction of polarization channels is not included as a step of the emulation process in these studies.

Step 1	The data is kept as quad-polarimetric and the NESZ is adjusted on the SLC products
Step 2	The data is downsampled and averaged to obtain dual-polarimetric resolution.
Step 3	The data is downsampled and averaged to obtain dual-polarimetric resolution and the NESZ is adjusted on the SLC products.

Table 7.2: Overview of emulation steps for cross-polarization ratio and damping ratio.

The damping ratio is found by averaging a local neighbourhood around each range position over an area of purely open water in the intensity image before being divided on the multi-looked intensity image of the scene. The results are presented in dB, which is obtained by taking $10 * log_{10}(Ratio)$.

The cross-polarization ratio is found by dividing the multi-looked image from the HV channel on the multi-looked image from the HH channel. The results are presented in dB, which is obtained by taking $10 * log_{10}(Ratio)$.

8

Results and discussion

In this chapter the co-polarization ratio is used to show that the imaged scene consists of thin first year ice and open water. Further, the 7 cases in the H, $\bar{\alpha}$, and the H/$\bar{\alpha}$-plot study is compared with results obtained from the original quad-polarimetric product. The cross-pol ratio is also presented and discussed in this chapter, as well as the damping ratio. The sensitivity to the NESZ is also presented as H and $\bar{\alpha}$ are sensitive to changes in the SNR.

8.0.1 Co-polarization ratio

As mentioned in section 6.3 the co-polarization ratio can be found by:

$$R_{HH/VV} = \frac{\langle |S_{VV}| \rangle}{\langle |S_{HH}| \rangle} \tag{8.1}$$

The co-polarization ratio can be used to discriminate between ice types and open water. The co-polarization ratio image in dB is presented in figure 8.1, showing that there is two distinctively different areas in the imaged scene. As thin sea ice normally have properties related to Fresnel reflection, and that the co-polarization ratio approaches zero when the thickness of young sea ice increases the areas in figure 8.1 that consists of small values is classified as thin ice. Open water is seen in areas with higher, positive co-polarization ratio values.

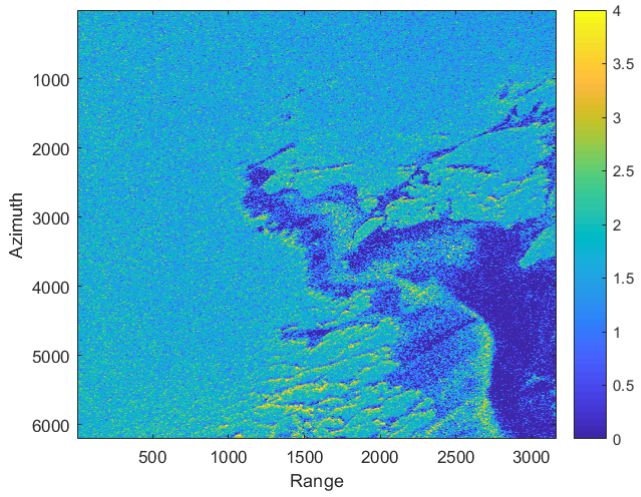

Figure 8.1: Co-polarization ratio image in dB over the entire scene, from November 28th 2017.

8.0.2 Sensitivity to the NESZ

H and $\bar{\alpha}$ are sensitive to the NESZ and it follows that the SNR is of equal importance. A transect is chosen in the imaged scene and plotted in figure 8.2 over the calibrated and filtered image from the HH channel. The mean of the values in the transect for each range position is then calculated for each polarization channel and plotted together with the FQ13 product NESZ and a SCWA product NESZ in figure 8.3.

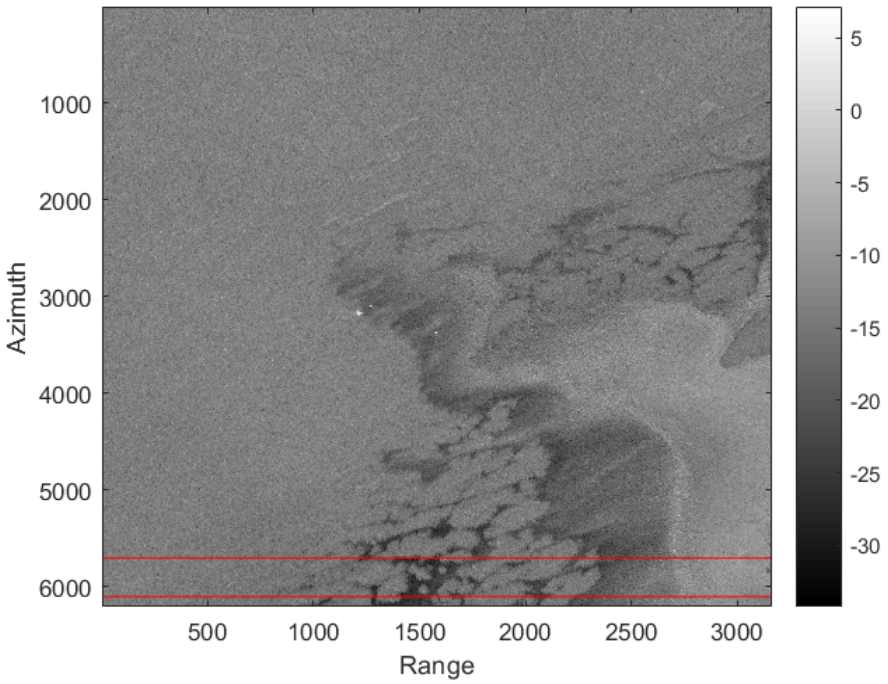

Figure 8.2: Transect of the calibrated and speckle reduced image in dB. Illustrated in the HH channel of the original data of the entire scene, from November 28th 2017.

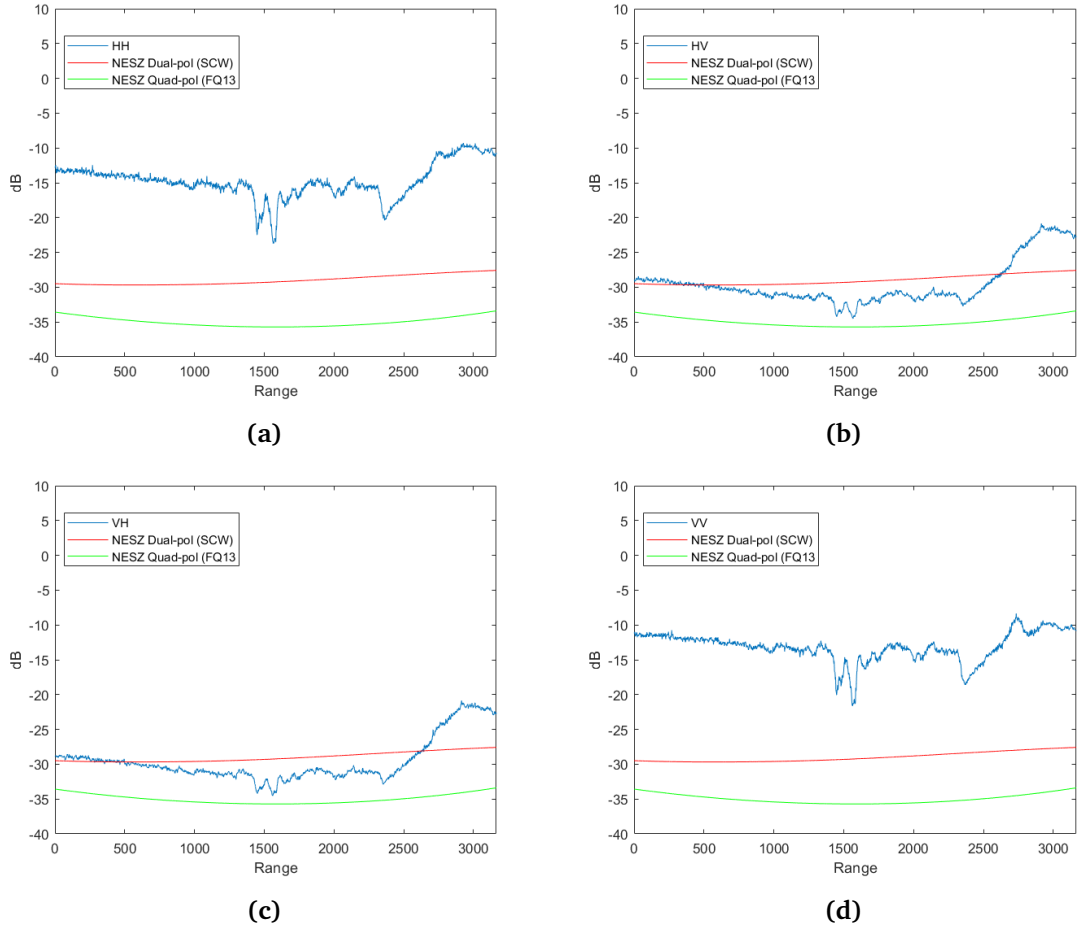

Figure 8.3: Mean backscatter range profiles plotted with the NESZ for dual-polarimetric (SCWA) and quad-polarimetric (FQ13) for (a) the HH channel, (b) the HV channel, (c) the VH channel, (d) the VV channel.

For RADARSAT-2 NESZ are beam specific and it follows that it is the same for all channels. It is clear that the signal in the cross-polarization channels contains less power than in the co-polarization channels. The HH channel ranges from -9.28 dB to -23.71 dB, the VV channel ranges from -8.35 dB to -21.63 dB, the HV channel ranges from -20.85 dB to -34.50 dB, and the VH channel ranges from -20.85 dB to -34.54 dB (see figure 8.3). This is visible as the difference between the cross-polarization channels and the quad-polarimetric NESZ is less (minimum 1 dB) than the difference between the co-polarization channels and the quad-polarimetric NESZ. For the dual-polarimetric NESZ both cross-polarization channels have areas that contains less power than the NESZ, while the co-polarimetric channels both lies over the NESZ. According to [31] a difference of 6dB or more between the signal and the NESZ represents

a satisfactory signal to noise ratio. The difference between the signals and the dual-polarimetric NESZ is shown in figure 8.4.

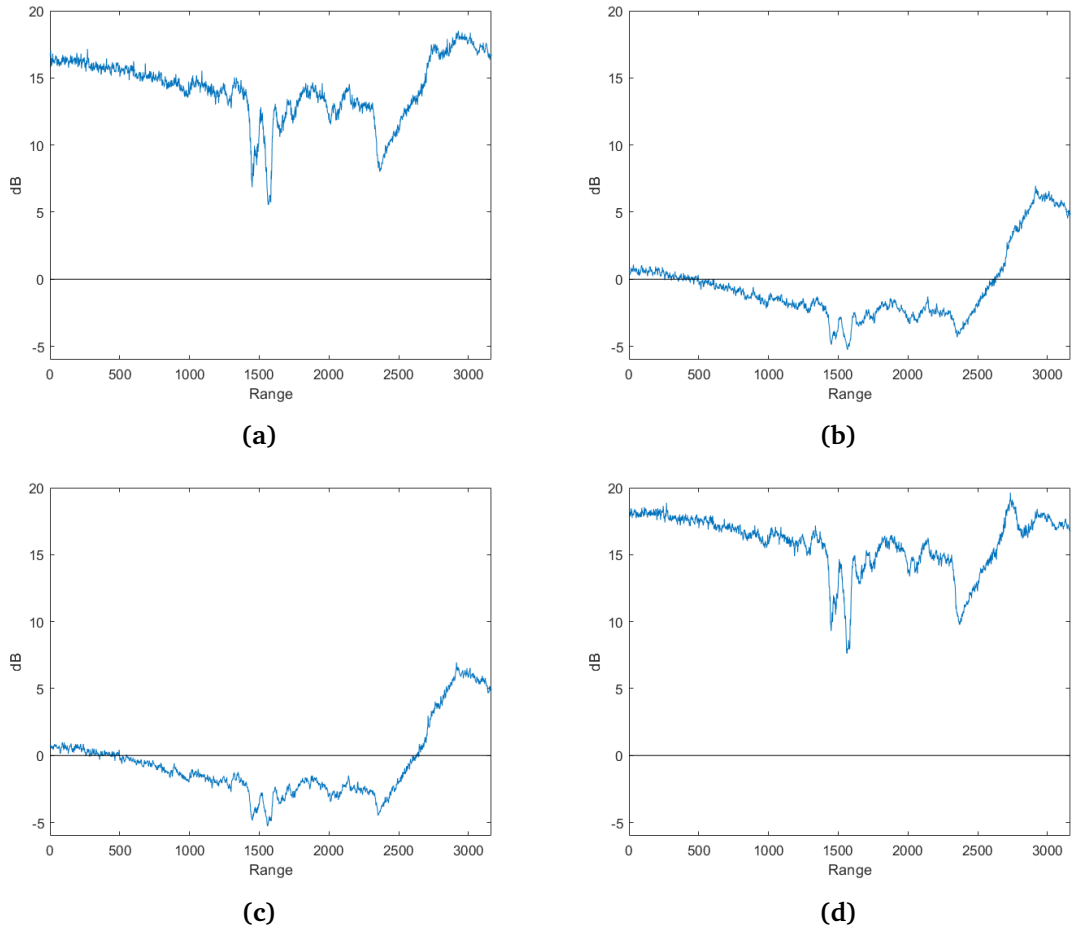

Figure 8.4: Difference between quad-polarimetric mean backscatter range profiles and dual-polarimetric (SCWA) NESZ for (a) the HH channel, (b) the HV channel, (c) the VH channel, (d) the VV channel.

The signal in the HH channel has a minimum difference to the dual-polarimetric NESZ of 5.53 dB, while the signal in the VV channel has a minimum difference to the dual-polarimetric NESZ of 7.62 dB. These signals more or less satisfy the difference of 6 dB, while the cross-polarization channels both have a maximum difference to the dual-polarimetric NESZ of about 6.95 dB. The cross-polarization channels will mostly have a difference of less than 6 dB, while the co-polarization channels have a difference of 6 dB or more except for the area with the lowest backscattering. Given this the co-polarization channels delivers signals that can safely be used for further analysis, and the additive noise is not disturbing the data in a manner that would give erroneous results when interpreting the data and calculating polarimetric features of the data. The cross-polarization channels does not obtain the difference of 6 dB over most areas, i.e. caution has to be used when interpreting results from the cross-polarization channels.

8.1 Entropy, $\overline{\alpha}$, H/$\overline{\alpha}$-plot study

In this section the cases represented in table 7.1 are presented and discussed. The cases will be compared with the results from the covariance and the coherency matrix of the original quad-polarimetric product. The H, $\bar{\alpha}$ and the H/$\bar{\alpha}$-plot is found for all cases to give a platform for comparison.

The H, $\bar{\alpha}$ and the H/$\bar{\alpha}$-plot from the covariance and the coherency matrices of the original quad-polarimetric product is shown in fig 8.5.

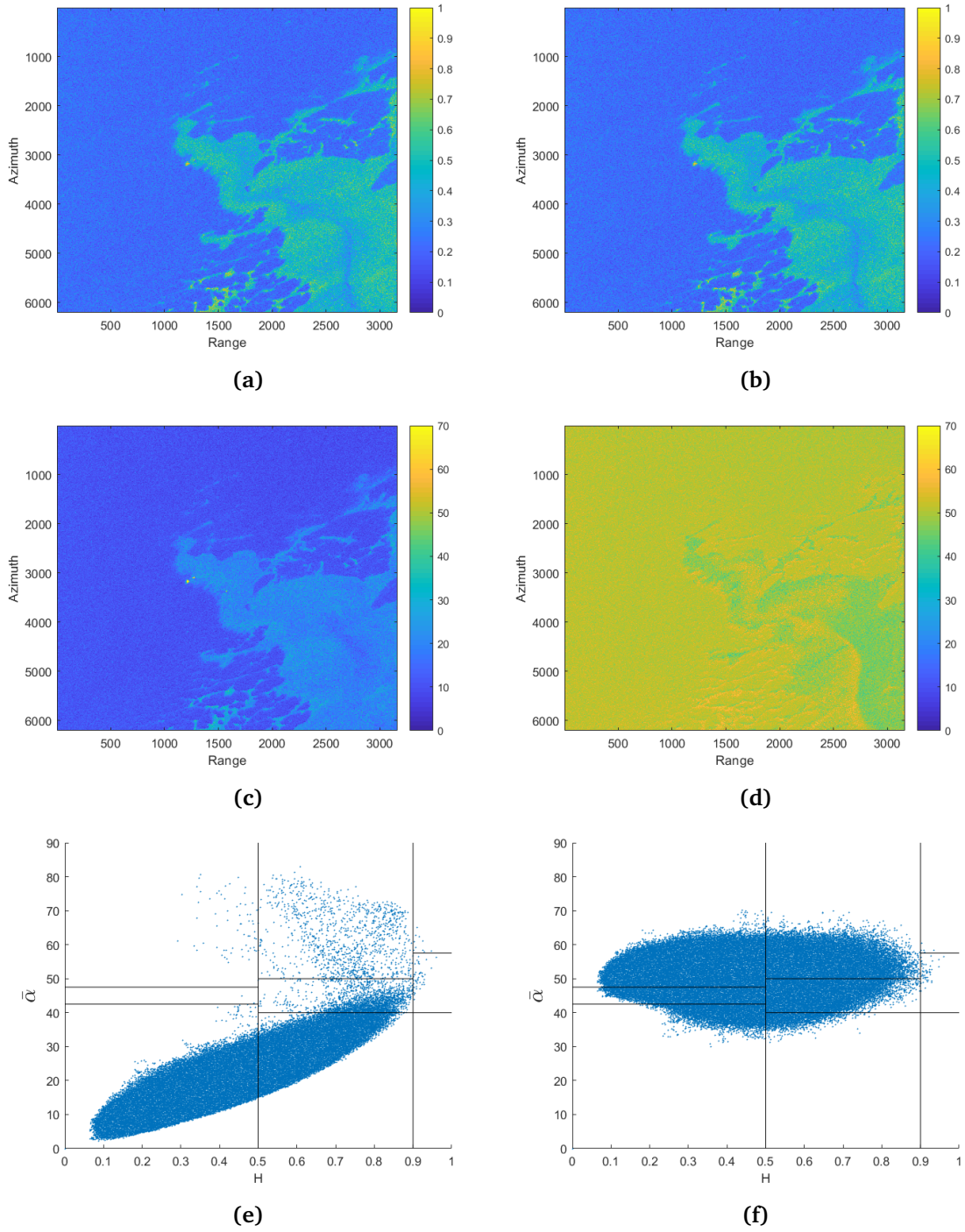

Figure 8.5: H image from (a) the coherency matrix, (b) the covariance matrix, $\bar{\alpha}$ image from (c) the coherency matrix, (d) the covariance matrix, H/$\bar{\alpha}$-plot from (e) the coherency matrix, (f) the covariance matrix.

Before the results from the cases are represented and discussed the differences between finding H, $\bar{\alpha}$, and H/$\bar{\alpha}$-plot from the covariance and the coherency matrix are addressed (see figure 8.5). The H images are equal both visually and numerically (maximum difference of $-4.38 * 10^{-15}$). The $\bar{\alpha}$-angle image is however not equal. These differences comes from the equality of the eigenvalues but not the eigenvectors as presented in section 5.5. The $\bar{\alpha}$-angles determines if the scattering is surface, double-bounce or volume like. It is visible in figure 8.5 that the values from the coherency matrix implies surface and partly double-bounce scattering, while the values from the covariance matrix implies double-bounce and volume scattering. It is clear that when using the covariance matrix the H image gives correct results while the $\bar{\alpha}$-angles are erroneous. Visually it is still possible to differ between different scattering scenes in the $\bar{\alpha}$ image.
The H/$\bar{\alpha}$-plot obtained from the coherency matrix shows that the majority of the scattering is surface scattering from Bragg surfaces and random surfaces. As an effect of the changed eigenvectors the H/$\bar{\alpha}$-plot obtained from the covariance matrix is not equal to the one from the coherency matrix. The values are spread over surface scattering, volume scattering and double bounce scattering. As the imaged scene consists of open water and thin ice it is expected to be classified as surface scattering, and it follows that the H/$\bar{\alpha}$-plot from the coherency matrix deliver the most anticipated result. Therefore H, $\bar{\alpha}$, and H/$\bar{\alpha}$-plot from the coherency matrix will be used as the main goal for the simulations and as the primary aid for comparison, while the polarimetric features obtained from the covariance matrix will function as a complementary aid for comparison.

The H values and $\bar{\alpha}$-angles from the coherency matrix over sea ice is consistent with findings in [12] which stated that fragmented pack ice, pack ice and first-year ice had H values in the range of 0.4-0.7, and $\bar{\alpha}$-angles in the range of 10-40 °. The findings from the covariance matrix is consistent with the findings in [12] for H values, but the $\bar{\alpha}$-angles are showing different results, as previously discussed.

8.1.1 NESZ adjustment

Case 1

After calibration the covariance matrix for the quad-polarimetric data is obtained according to the theory presented in section 5.3. The NESZ is then adjusted according to section 5.6, by utilizing the difference between the NESZ of the quad-polarimetric RADARSAT-2 FQ13 product and the dual-polarimetric RADARSAT-2 SCWA product. The resulting H, $\bar{\alpha}$, and H/$\bar{\alpha}$-plot is presented in fig 8.6.

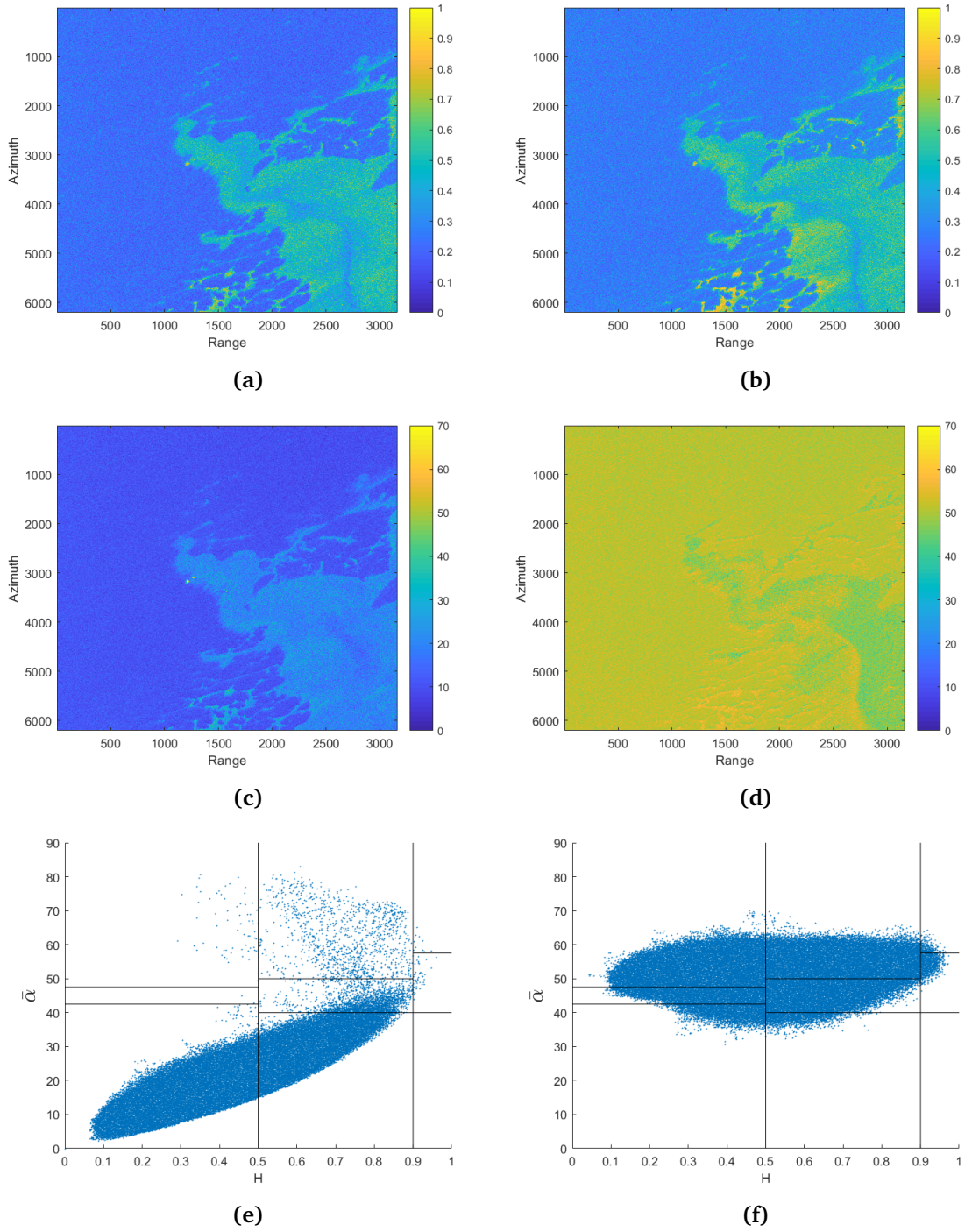

Figure 8.6: H image from (a) the coherency matrix, (b) the covariance matrix found in case 1, $\bar{\alpha}$ image from (c) the coherency matrix, (d) the covariance matrix found in case 1, H/$\bar{\alpha}$-plot from (e) the coherency matrix, (f) the covariance matrix found in case 1.

The H image obtained in case 1 is similar to the H image from the coherency matrix of the original quad-polarimetric data, with higher values in the ROIs (region of interest) outlined in figure 8.7. These ROIs contain low backscatter values in the intensity image, causing these areas to be more affected by the NESZ adjustment done in this case. This is intuitive as the power of the NESZ added is the same in each range position, causing a bigger change where the original signals power is lower. Raising the NESZ implicates a higher power of noise in the received signal, which again implicates more randomness (higher H), see subsection 6.1.1.
As the eigenvectors is different for the coherency and the covariance matrix the $\bar{\alpha}$-angles will also become different, based on the theory presented in section 6.1.2. The $\bar{\alpha}$ image from case 1 resembles the $\bar{\alpha}$ image from the covariance matrix from the original quad-polarimetric data more than the $\bar{\alpha}$ image from the coherency matrix from the original quad-polarimetric data.
The H/$\bar{\alpha}$-plot obtained in case 1 shows an overall tendency of $\bar{\alpha}$-angles centered around 50 °. This is an increase in overall $\bar{\alpha}$-angles, also visible in the $\bar{\alpha}$ image. The H values ranges from quasi deterministic to highly random, as for H from the original quad-polarimetric data, but have some higher values seen in the H image. The scattering mechanisms deduced from the H/$\bar{\alpha}$-plot is spread over all but the non feasible region, and contains little surface scattering.

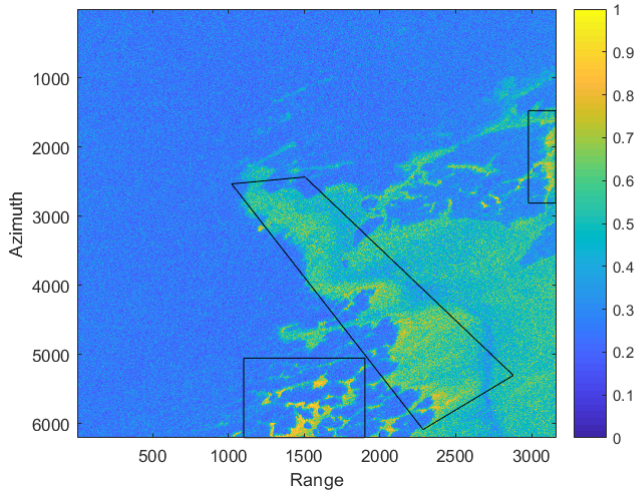

Figure 8.7: ROIs of low σ_0 backscatter and higher H values outlined in black boxes, shown in H image from case 1.

Case 2

After calibration the coherency matrix for quad-polarimetric data is obtained according to the theory presented in section 5.4. The NESZ is then adjusted according to section 5.6, by utilizing the difference between the NESZ of the quad-polarimetric RADARSAT-2 FQ13 product and the dual-polarimetric RADARSAT-2 SCWA product. The resulting H, $\bar{\alpha}$, and H/$\bar{\alpha}$-plot is presented in fig 8.8.

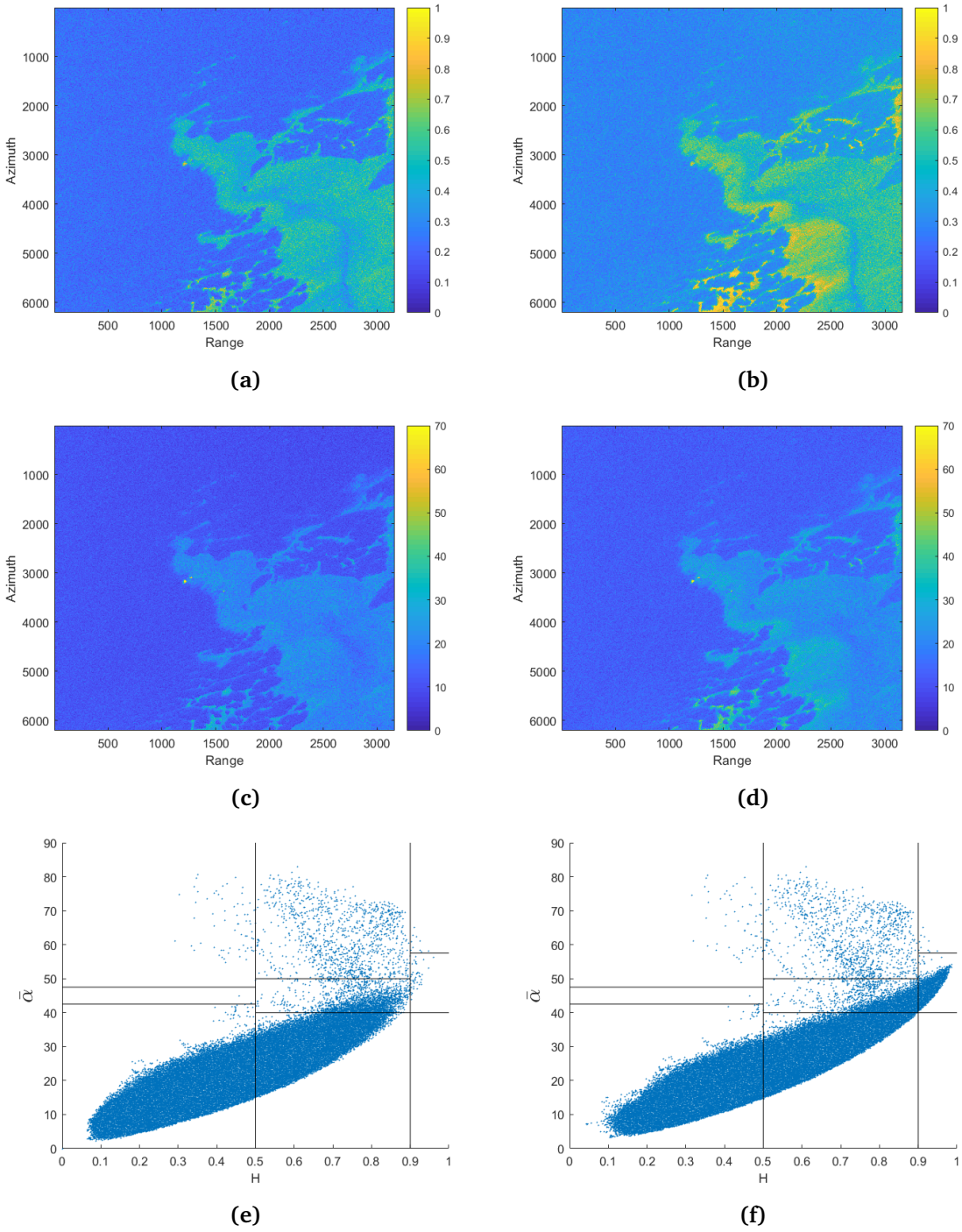

Figure 8.8: H image from (a) the coherency matrix, (b) the coherency matrix found in case 2, $\bar{\alpha}$ image from (c) the coherency matrix, (d) the coherency matrix found in case 2, H/$\bar{\alpha}$-plot from (e) the coherency matrix, (f) the coherency matrix found in case 2.

As in case 1 the H image undergoes higher changes in the ROIs seen in figure 8.7 by adjustment of the NESZ. These areas are the same as in case 1 and the same reasoning for why these areas are more affected holds for case 2 as well. However, the change in values are not the same as in case 1. This is unexpected, as the eigenvalues should be the same for the coherency and the covariance matrix (see section 5.5). Overall in the H image this difference is small, as seen in figure 8.9. Here the difference between the H values for each position is found, before averaged for each range position and plotted. The maximum difference in figure 8.9 is 0.055 indicating a maximum difference of 5.5% and a minimum difference of 0.029 indicating a minimum difference of 2.9%. The smallest differences is found over open water where the difference between the signal and NESZ is biggest, while the biggest differences is found over areas with sea ice, specially the areas outlined in the ROIs seen in figure 8.7. Possible reasons can be the SNR and the low backscattering in these areas.

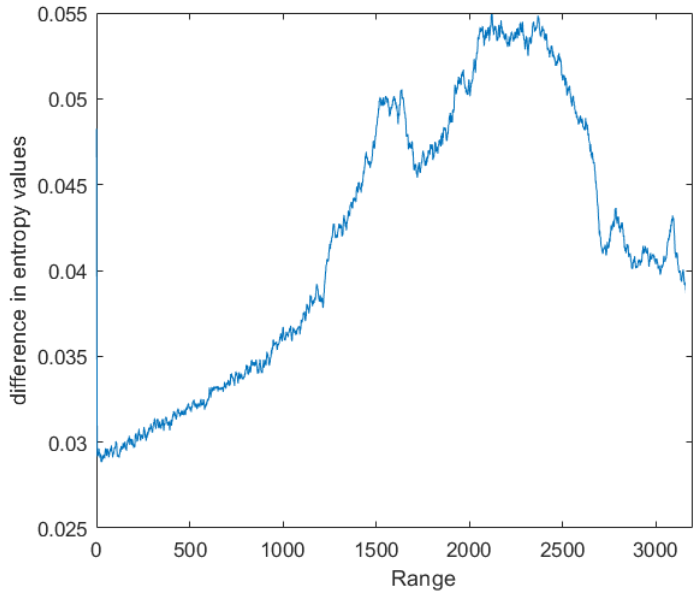

Figure 8.9: Mean difference in range direction between case 1 and case 2 H.

From figure 8.9 it can be seen that the difference over ice is bigger than over open water. Two of the areas where the difference is largest visually is chosen and presented in figure 8.10. The difference in H values is found for each position in the areas before the mean of the difference is found. The mean of the difference in area 1 is 0.074 which implies a difference of 7.4%, and the mean of the difference in area 2 is 0.07, i.e. 7%. The rest of the cases bases its H on the covariance matrix, and it is assumed that the NESZ adjustment on the covariance matrix is correct. However, extra care has to be taken over area 1 and area 2, as these areas yielded the most different results from NESZ adjustment on the covariance- and the coherency matrix.

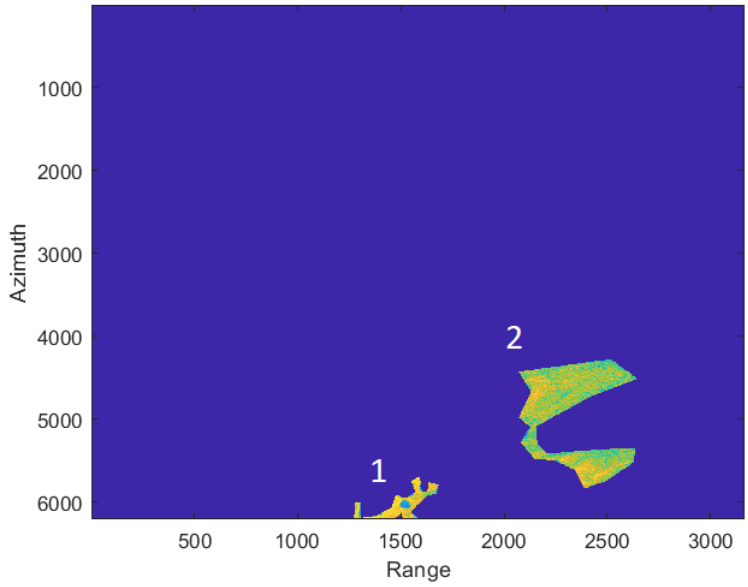

Figure 8.10: Areas where the difference in H is most apparent between case 1 and case 2.The areas is presented in the H image from case 2.

The $\bar{\alpha}$ image shows expected results. It resembles the one from the coherency matrix obtained from the original quad-polarimetric data but contains higher values. The 2D Pearson correlation coefficient is 0.97 for these two. As a constant is added in each range direction the eigenvector will still be the same, and the difference seen in the $\bar{\alpha}$ image comes from the change of eigenvalues (see Appendix).
The H/$\bar{\alpha}$-plot resembles the one obtained from the coherency matrix of the original quad-polarimetric data. The differences is caused by the difference in eigenvalues, leading to higher values of H, and higher angles of $\bar{\alpha}$. The NESZ adjustment is done by adding higher values on the diagonal of the coherency matrix, leading to higher eigenvalues as explained in the Appendix. The majority of the scattering is still surface scattering, i.e. the majority of the

scattering is classified as Bragg scattering and random surface scattering. The cluster has a slight shift to the right of the plot, and some values have moved to scattering from random anisotropic scatterers.

Case 3

After calibration the NESZ is adjusted by adding circularly white Gaussian noise with power equal to the NESZ directly on the SLC products, i.e.

$S_{i,j}(new) = S_{i,j}(QP) + N_{i,j}$, where $N_{i,j} \sim CN(0, \sigma^n_{i,j})$ is the added noise.

The coherency matrix is then obtained, and should correspond to the one in case 2, based on the theory in section 5.6. The resulting H, $\bar{\alpha}$, and the H/$\bar{\alpha}$-plot is shown in fig 8.11.

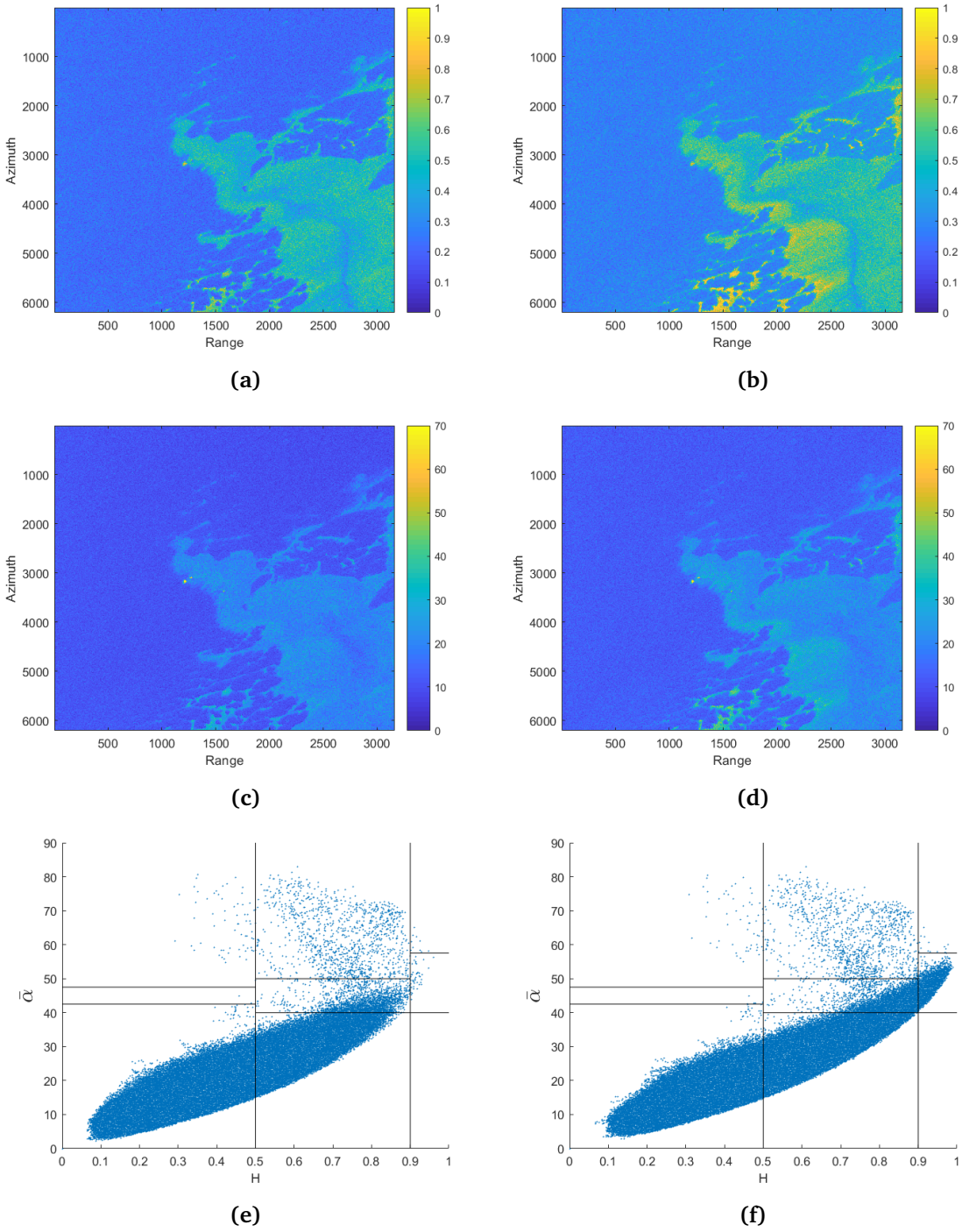

Figure 8.11: H image from (a) the coherency matrix, (b) the coherency matrix found in case 3, $\bar{\alpha}$ image from (c) the coherency matrix, (d) the coherency matrix found in case 3, H/$\bar{\alpha}$-plot from (e) the coherency matrix, (f) the coherency matrix found in case 3.

As in case 2 the H image shows expected results. It contains higher values than the H image from the coherency matrix from the original quad-polarimetric data, but has an overall resemblance. The H image from case 2 and case 3 are visually close to identical. Numerically the difference in H value has a mean of 0.021 and a standard deviation of 0.003.
Similar to the H image the $\bar{\alpha}$ image shows similarities to the $\bar{\alpha}$ image from the coherency matrix of the original quad-polarimetric data. It is visually close to identical to the one obtained in case 2, and the difference in angle has a mean of 0.500 and a standard deviation of 0.189.
The H/$\bar{\alpha}$-plot is also visually close to identical as that in case 2, which is intuitive as the differences in the H and $\bar{\alpha}$ is minimal. The 2D Pearson correlation coefficient for the H and $\bar{\alpha}$ is 0.991 and 0.990, respectively.

Case 1 and 2 shows that raising the NESZ by utilizing the covariance and the coherency matrix gives different results in the H image. This is not expected as the theory states that the eigenvalues should be the same for the covariance and the coherency matrix. The constant added to the diagonal of the matrices are the same, and should affect the eigenvalues in an equal manner. Case 3 shows that raising the NESZ directly on the SLC products deliver close to the same results as in case 2, and proves that adjustment of NESZ can be done directly on the SLC products. It is seen that the adjustment of NESZ causes higher overall values in both the H values and the $\bar{\alpha}$-angles.

8.1.2 Dual-polarimetric data emulation

Case 4

After calibration the quad-polarimetric SLC products is downsampled and averaged according to the difference in pixel spacing and incidence angle for the RADARSAT-2 FQ13 product and the RADARSAT-2 SCWA product. The covariance matrix is then found for the emulated quad-polarimetric product with dual-polarimetric resolution. In this case no noise is added. The resulting H, $\bar{\alpha}$, and $\bar{\alpha}$-plot is shown in fig 8.12.

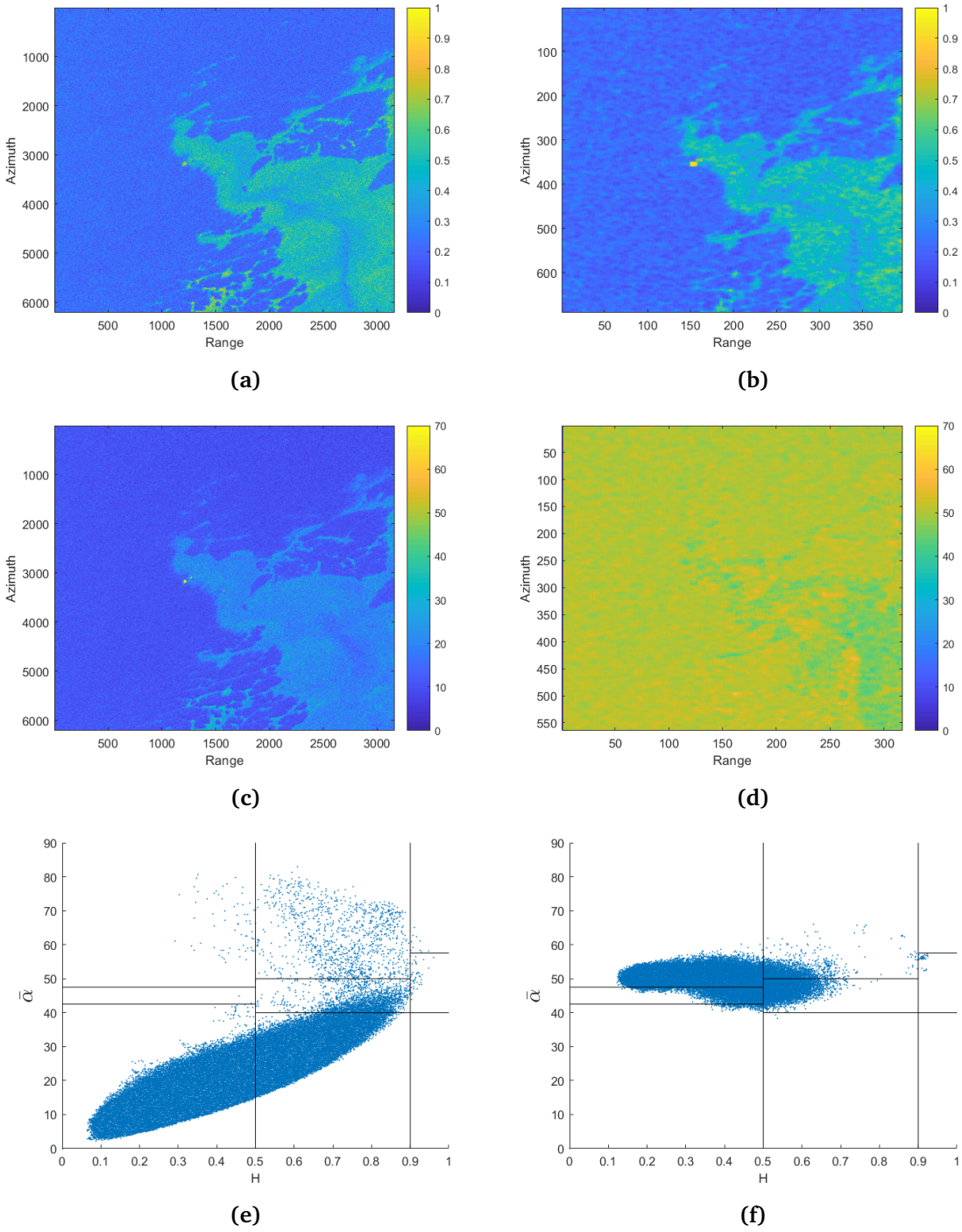

Figure 8.12: H image from (a) the coherency matrix, (b) the covariance matrix found in case 4, $\bar{\alpha}$ image from (c) the coherency matrix, (d) the covariance matrix found in case 4, H/$\bar{\alpha}$-plot from (e) the coherency matrix, (f) the covariance matrix found in case 4.

The downsampling is clearly visible in the H image. It resembles the H image from the coherency matrix obtained from the original quad-polarimetric data, with similar values in corresponding areas of the imaged scene. The mean value in each range position over a transect equal to the one shown in figure 8.2 is found for the H images shown in figure 8.12 and plotted in figure 8.13, where the mean values found for the product with dual-polarimetric resolution are interpolated using nearest neighbour.

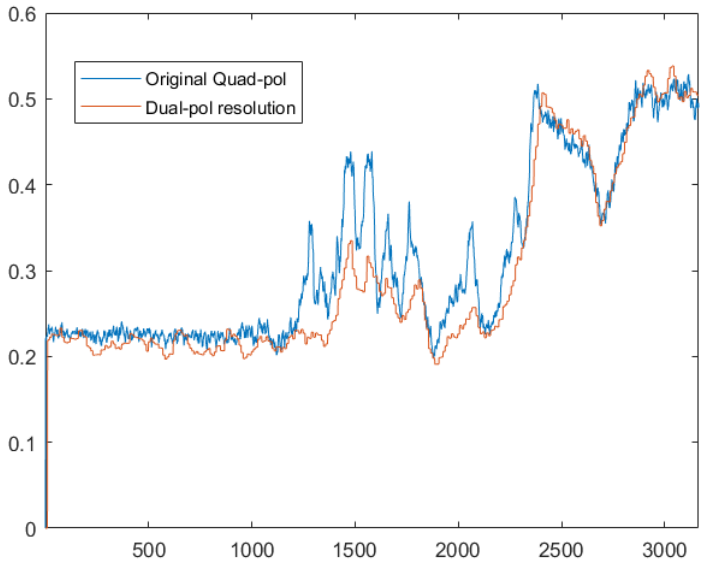

Figure 8.13: Mean values for each range position.

The emulation of dual-polarimetric resolution does not seem to affect the overall values much, but causes less finer details to appear in the imaged scene. The $\bar{\alpha}$ image is expected to show different angles than the one gained from the coherency matrix from the original quad-polarimetric data, as the eigenvectors are not the same. The values are intermediate, around 50 °, and resembles the $\bar{\alpha}$ image obtained from the covariance matrix of the original quad-polarimetric product but also the $\bar{\alpha}$ image obtained from case 1 (figure 8.6d).

The H/$\bar{\alpha}$-plot shows that the $\bar{\alpha}$ consist of intermediate values, and that the H falls between 0.1-0.9. Its shape is consistent with previous results building on the covariance matrix. The spread in H values compared to the H values for the coherency matrix from the original quad-polarimetric data is less continuous. Gradually changing the pixel spacing shows the averaging effect, where the outlying values moves towards the center. The H/$\bar{\alpha}$-plots with 0.2, 0.4, 0.6, and 0.8 times the actual difference between the RADARSAT-2 FQ13 and SCWA pixel spacing is represented in figure 8.14.

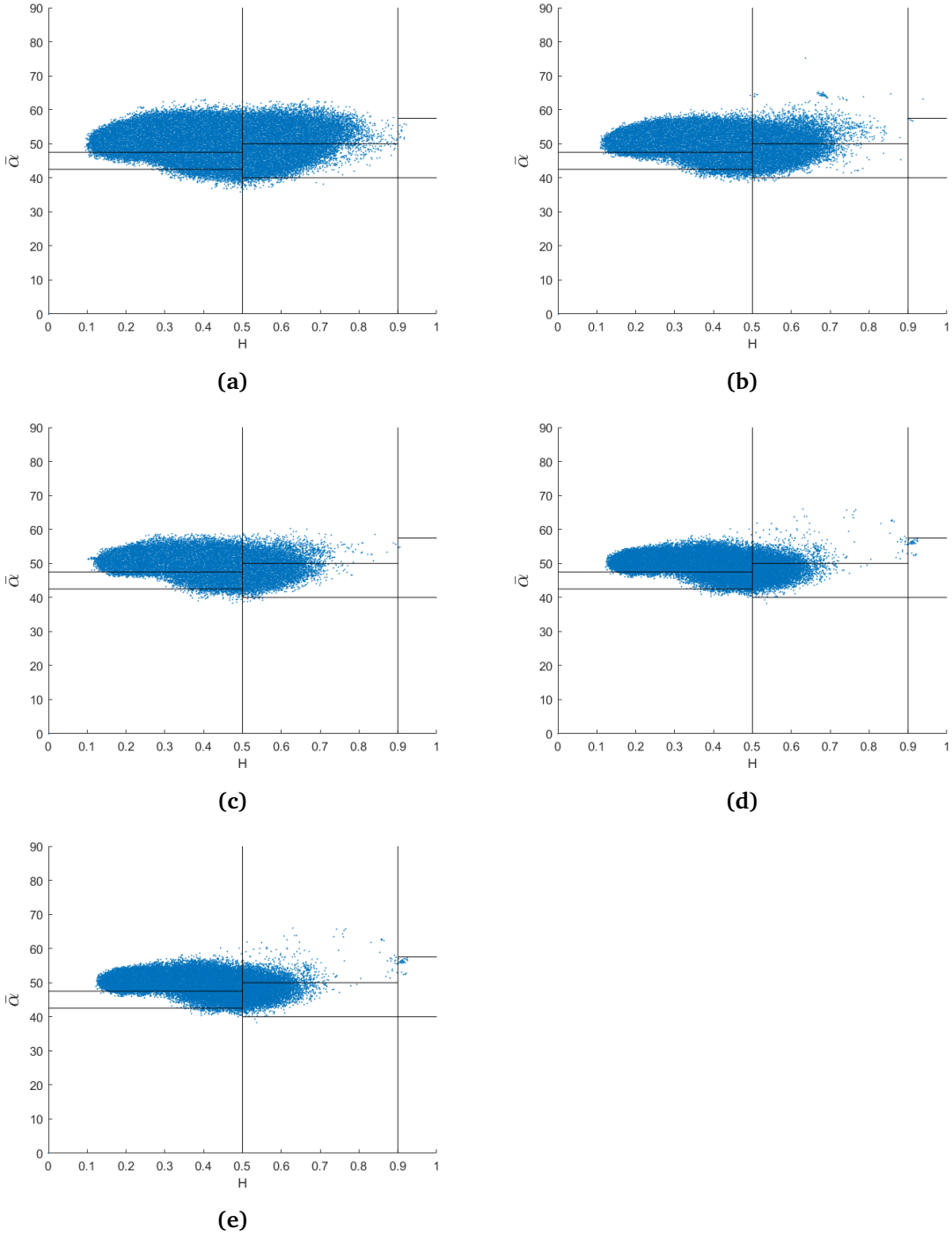

Figure 8.14: Increasing the difference of pixel spacing in increments (a) 0.2 times, (b) 0.4 times, (c) 0.6 times, (d) 0.8 times the actual difference, leading to the actual difference (e) between FQ13 and SCWA pixel spacing.

Case 5

After calibration channels VH and VV are removed, to emulate a dual-polarimetric product with quad-polarimetric resolution. The covariance matrix is then found. In this case no noise is added. The resulting H, $\bar{\alpha}$, and $\bar{\alpha}$-plot is shown in figure 8.15.

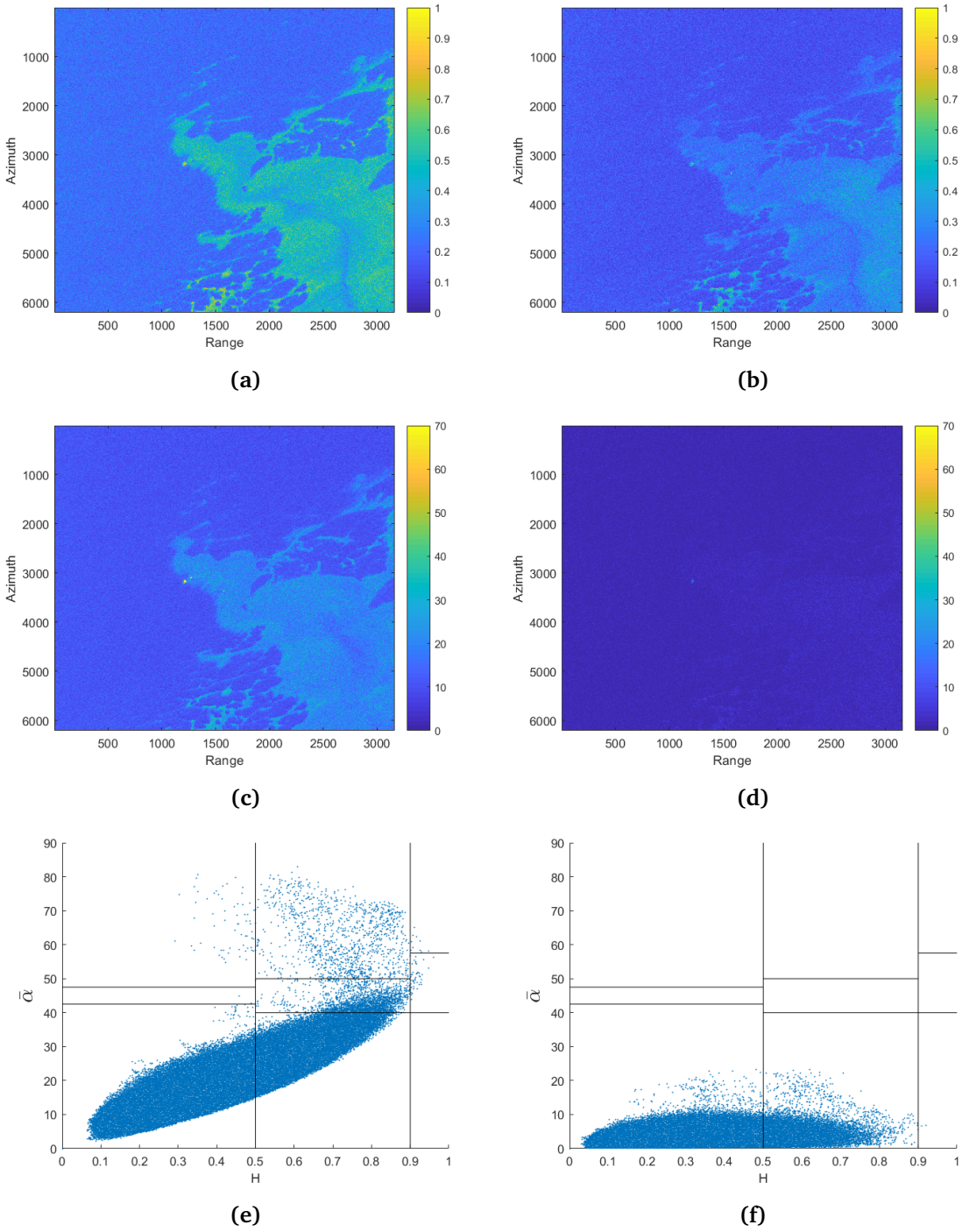

Figure 8.15: H image from (a) the coherency matrix, (b) the covariance matrix found in case 5, $\bar{\alpha}$ image from (c) the coherency matrix, (d) the covariance matrix found in case 5, H/$\bar{\alpha}$-plot from (e) the coherency matrix, (f) the covariance matrix found in case 5.

The H image in case 5 contains lower values than the H image from the coherency matrix obtained from the original quad-polarimetric data as seen in figure 8.15. Areas of higher values in the H image from the original quad-polarimetric data still contains higher values in the H image from case 5. The mean difference between the H over two areas with higher values and two areas with lower values is found. The areas chosen is seen in fig. 8.16

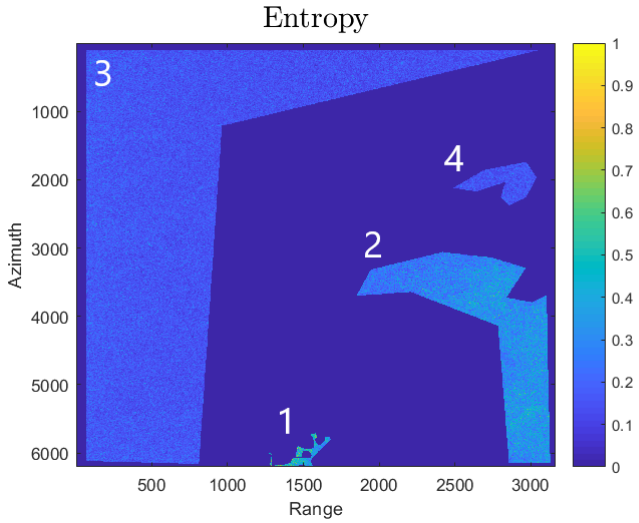

Figure 8.16: Areas chosen in the two H images. 1 2 contains higher values, 3 4 contains lower H values.

An overview of mean σ_0 values in the HH channel, H values from the original quad-polarimetric data and H values from case 5 in these areas are presented in table 8.1 along with the mean difference of H from the original quad-polarimetric data and case 5. The σ_0 values are obtained after calibration and speckle reduction of the data.

Area	Type of area	σ_0	H quad-pol	H Case 5
1	TNFI	0.0037	0.5986	0.4371
2	ThNFI	0.0629	0.4804	0.2914
3	OW	0.0475	0.2156	0.1525
4	OW	0.0397	0.2171	0.1607
Mean diff H values	Area 1	Area 2	Area 3	Area 4
	0.1632	0.1753	0.0617	0.0563

Table 8.1: Overview of σ_0 values in the HH channel, mean H values and mean difference between H values from the original quad-polarimetric data and case 5, TNFI = Thin newly formed ice, ThNFI = Thicker newly formed ice, OW = Open water.

The difference lies between 5.63% to 6.17% over the low H areas chosen and 16.32% to 17.53% over the high H areas. It is clear that the difference is not the same over the whole image, but the difference over area 1 and 2 is close to the same, and the difference over 3 and 4 is close to the same.
As with the H image, the $\bar{\alpha}$ image consists of lower angles than in the image from the original quad-polarimetric data. In earlier cases where the $\bar{\alpha}$ was calculated based on the covariance matrix the angles were higher than the $\bar{\alpha}$-angles obtained from the coherency matrix. This is not the case here, and the eigenvectors is clearly altered by the reduction of polarization channels.
The values in the H/$\bar{\alpha}$-plot is spread throughout the H, but contain low $\bar{\alpha}$-angles. A question that arises is how different pure scatterers would be placed when only the HH and HV channel is used. As stated in section 5.2 a targetvector can be found by $k = V(S) = \frac{1}{2}Tr(S\Psi)$. The scattering matrix of an isotropic surface, horizontal dipole and isotropic dihedral is represented in the following way, respectively:

$$S_{iso} = \begin{bmatrix} 1 & 0 \\ 0 & 1 \end{bmatrix}, S_{dip} = \begin{bmatrix} 1 & 0 \\ 0 & 0 \end{bmatrix}, S_{dih} = \begin{bmatrix} 1 & 0 \\ 0 & -1 \end{bmatrix} \text{ [Lee, Pottier, 2009]}$$

For quad-polarimetric data these scattering mechanisms represents $\bar{\alpha}$-angles of 0°, 45°, and 90° respectively. However, for dual-polarimetric HH/HV data these scattering mechanisms is represented as $S_{iso} = S_{dip} = S_{dih} = \begin{bmatrix} 1 & 0 \\ 0 & 0 \end{bmatrix}$, and $\bar{\alpha}_{iso} = \bar{\alpha}_{dip} = \bar{\alpha}_{dih} = 0$. Dual-polarimetric HH/HV are in other words not able to diminish between different scattering mechanisms, and it follows that the H/$\bar{\alpha}$-plot contains values close to 0 in the $\bar{\alpha}$ direction.
By utilizing two polarization channels the H values decreases. In this case the number of H values above 0.8 is reduced, causing less scattering in the highly random domain of the H. The $\bar{\alpha}$-angles of different scatterers is not able to differ in the dual-polarimetric HH/HV case, as all elementary scatterers are characterized by the same scattering matrix. Also the NESZ causes implications when using emulated dual-polarimetric C-band SAR data. The HV channel

does not attain the desired difference of 6 dB between the backscattered signal and the NESZ proposed in [31], and it follows that the SNR in the HV channel is too low.

Case 6

In case 6, after calibration, the data is averaged and downsampled before polarization channels VH and VV is removed. The resulting dual-polarimetric emulated product with quad-polarimetric NESZ is then used to find the covariance matrix. The resulting H, $\bar{\alpha}$, and $\bar{\alpha}$-plot is shown in figure 8.17.

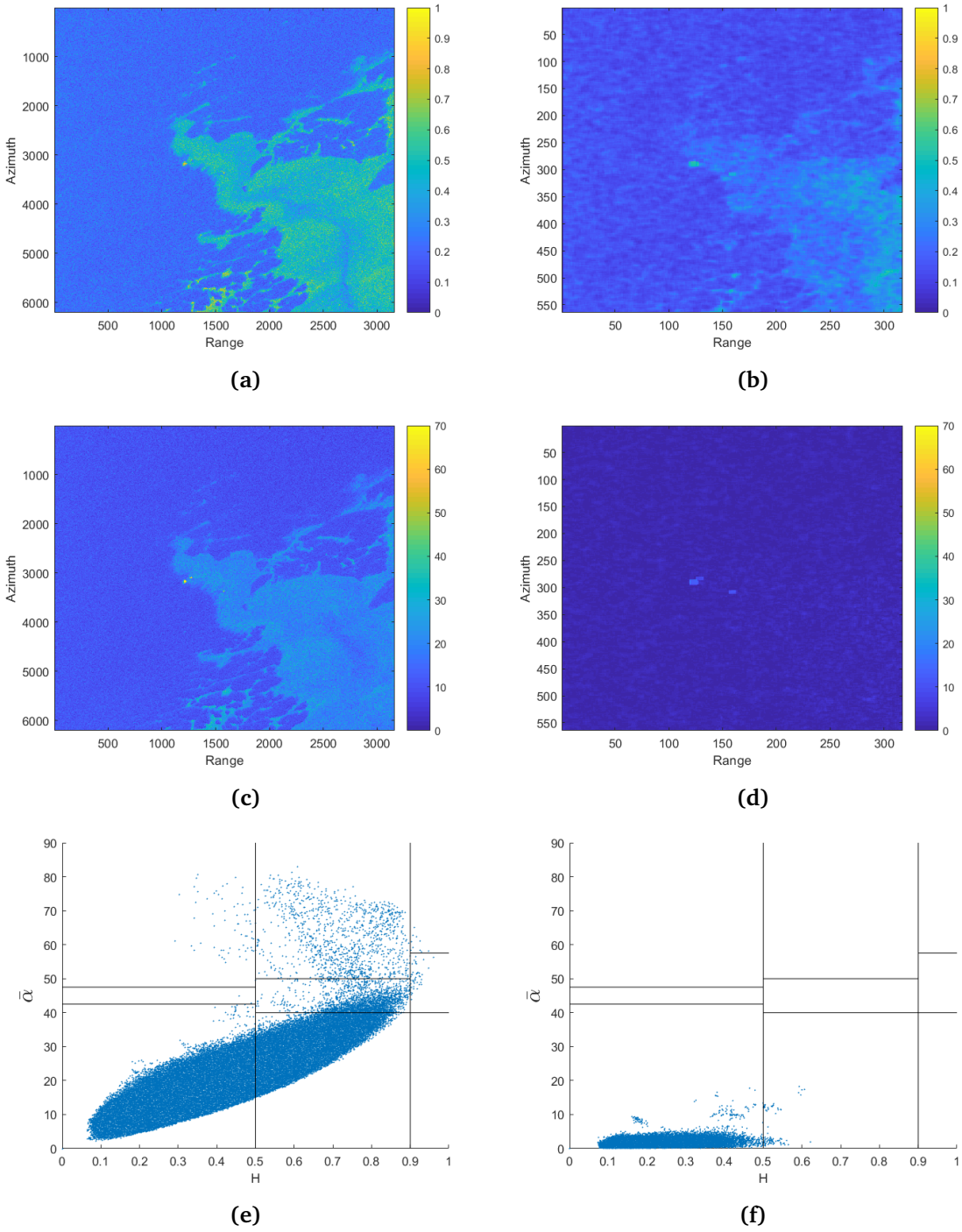

Figure 8.17: H image from (a) the coherency matrix, (b) the covariance matrix found in case 6, $\bar{\alpha}$ image from (c) the coherency matrix, (d) the covariance matrix found in case 6, H/$\bar{\alpha}$-plot from (e) the coherency matrix, (f) the covariance matrix found in case 6.

The H image has a lower resolution than the one obtained from the coherency matrix of the original quad-polarimetric data. The H values is lower throughout the image caused by the reduction of polarization channels, implying that the eigenvalues have been altered (see section 6.1.1). The majority of the H values ranges from about 0.1-0.55, a shorter range than for the original quad-polarimetric data caused by the adjustment of pixel spacing. This is intuitive as some of the finer details in the quad-polarimetric data is neglected, and the information used is smoothed.
As the H values the $\bar{\alpha}$-angles are also lower than from the original quad-polarimetric data, and the image looks more or less monotone. The eigenvectors is clearly altered by the reduction of polarization channels. It is not possible to diminish between different scatterers (single, double bounce and volume) as the $\bar{\alpha}$-angles for these are the same, as the scattering matrix describing these scattering mechanisms are the same, as shown in case 5.
The H/$\bar{\alpha}$-plot shows that both the H values and the $\bar{\alpha}$-angles are lower than the ones obtained from the coherency matrix of the original quad-polarimetric data.
It is clear that multiple effects causes degradation of the signal even before the adjustment of the NESZ. It is still possible to separate between bigger areas of high and low H, but the values of high and low H varies between the original data and the emulated dual-polarimetric data. The $\bar{\alpha}$-angles is expected to differ as it is withdrawn from the covariance matrix for the dual-polarimetric data. Also here it is clear that the reduction of polarization channels to dual-polarimetric HH/HV causes all $\bar{\alpha}$-angles to be zero, and different scattering mechanisms are not possible to differ.

Case 7

After calibration the data is averaged and downsampled to meet dual-polarimetric resolution. Then, the polarization channels (VH and VV) is removed before the covariance matrix is found. The NESZ is then adjusted by adding the difference between the RADARSAT-2 FQ13 product NESZ and the RADARSAT-2 SCWA product NESZ. The resulting H, $\bar{\alpha}$, and $\bar{\alpha}$ plot is shown in fig 8.18. Case 7 represents a full emulation of a dual-polarimetric product from a quad-polarimetric product.

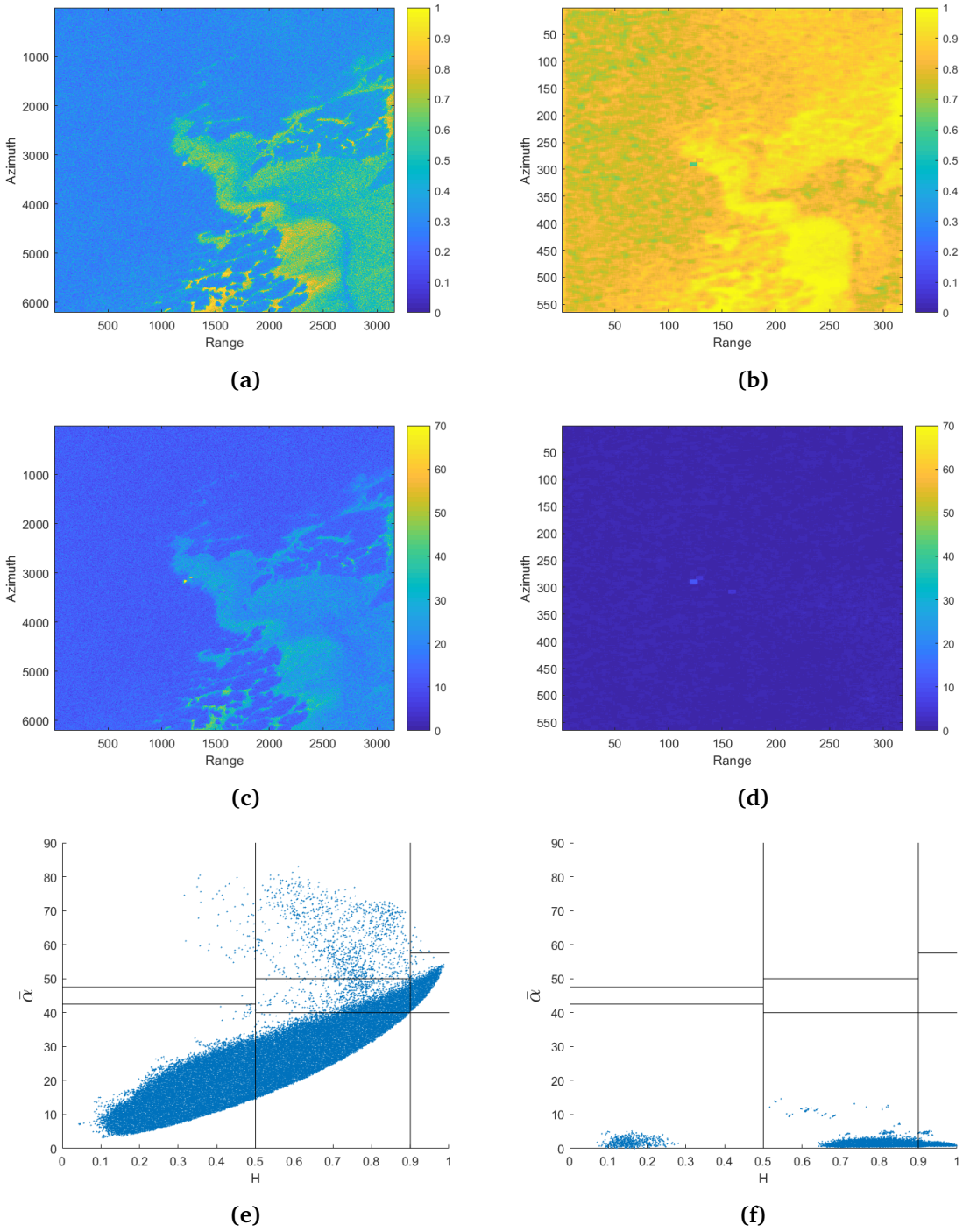

Figure 8.18: H image from (a) the coherency matrix, (b) the covariance matrix found in case 7, $\bar{\alpha}$ image from (c) the coherency matrix, (d) the covariance matrix found in case 7, H/$\bar{\alpha}$-plot from (e) the coherency matrix, (f) the covariance matrix found in case 7.

The H image from case 7 contains higher values than the other cases. It is apparent that raising the NESZ have a bigger impact on the H for the complete emulated dual-polarimetric data. Most of the H values lies in two distinct clusters, one around 0.1-0.2 and the other around 0.64-1. The cluster with higher H contains more values as visible in figure 8.18b and f. As two polarization channels are removed much information is also discriminated, causing the adjustment of the NESZ to be more apparent. In addition most of the HV channel lies underneath the NESZ (see figure 8.4), and the signal from the HV channel can therefore deliver faulty results when the desired output is ground truth. As the overall H values are high it implies that the eigenvalues of the covariance matrix is more altered by the adjustment of the NESZ when only two polarization channels are used.
The $\bar{\alpha}$ image resembles the one obtained in both case 6 and case 5. It is intuitive based on the theory presented in section 7.3 that the $\bar{\alpha}$ image should be similar to the one from case 6 as the noise is added on the diagonal of the covariance matrices, and the biggest change is found in the eigenvalue, which is of less importance in the $\bar{\alpha}$-angles than the H values. It is also apparent that it is not possible to differentiate between single-, double bounce- and volume scattering, as the scattering matrices for these types of mechanisms becomes the same for dual-polarimetric HH/HV products.
The H/$\bar{\alpha}$-plot forms two distinct clusters on each side of the H range, which implies that there exists two areas of the image with different disorder. All values are based around 0 in $\bar{\alpha}$ direction, which is intuitive as the HH and HV channels are used in this case. Some of the values are also found in the non feasible region of the H/$\bar{\alpha}$-plot. The disctinct clusters visible in figure 8.18(f) forms based on the adjustment of the NESZ. An incrementwise adjustment of the NESZ was done and presented in figure 8.19. Here the NESZ was adjusted with 0.1,0.2,0.3,...,0.9 times the difference between FQ13 NESZ and SCWA NESZ. The distinctiveness of the clusters increases for each increment.

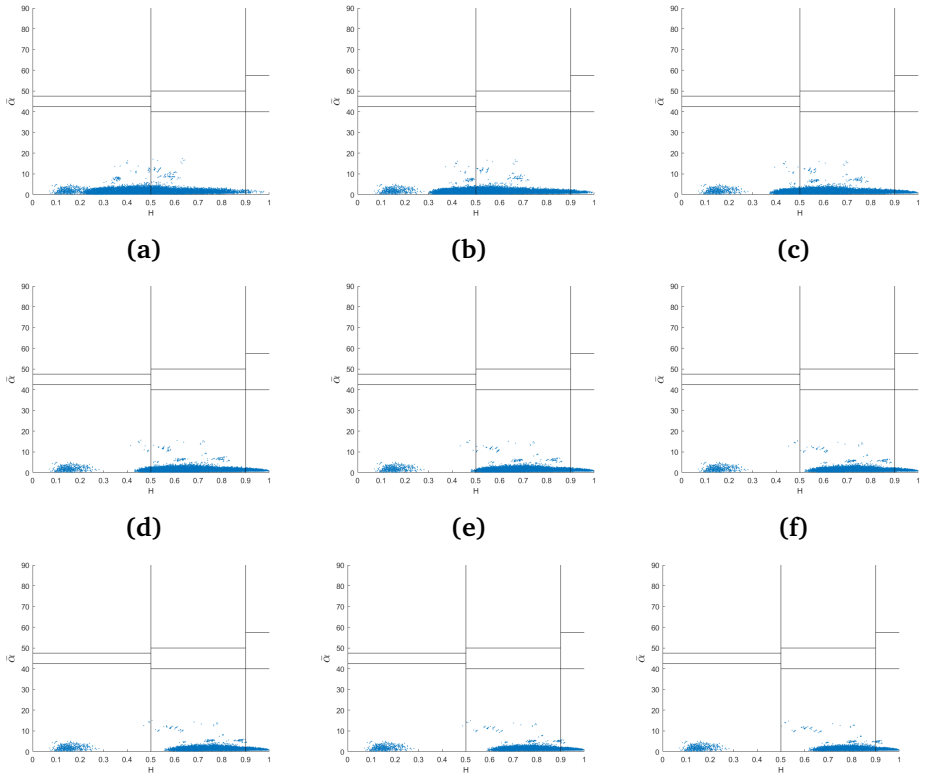

Figure 8.19: H/$\bar{\alpha}$-plots of dual-polarimetric data with (a) 0.1, (b) 0.2, (c) 0.3, (d) 0.4, (e) 0.5, (f) 0.6, (g) 0.7, (h) 0.8, (i) 0.9 times the difference of FQ13 NESZ and SCWA NESZ.

Mean values of H and $\bar{\alpha}$-angles from all the cases over the 4 regions outlined in figure 8.16 is presented in table 8.2.

Area	Area 1	Area 2	Area 3	Area 4
Type of area	TNFI	ThNFI	OW	OW
I [dB]	-24.30	-11.41	-13.06	-13.93
Mean H				
Comp	0.59	0.49	0.22	0.22
Case 1	0.75	0.52	0.26	0.29
Case 2	0.82	0.54	0.29	0.35
Case 3	0.79	0.53	0.28	0.32
Case 4	0.39	0.49	0.21	0.21
Case 5	0.43	0.31	0.16	0.16
Case 6	0.26	0.31	0.15	0.15
Case 7	0.98	0.83	0.79	0.90
Mean $\bar{\alpha}$				
Comp	27.43	20.09	10.94	10.63
Case 1	54.32	48.00	51.17	51.14
Case 2	38.21	21.97	12.76	14.10
Case 3	37.43	21.66	12.39	13.45
Case 4	51.16	47.43	50.41	50.34
Case 5	3.21	2.81	1.84	1.85
Case 6	1.77	1.79	1.27	1.25
Case 7	0.93	1.32	1.05	0.95

Table 8.2: Mean values of H and $\bar{\alpha}$ for 4 areas. TNFI = Thin newly formed ice, ThNFI = Thicker newly formed ice, OW = Open water, I is the backscattered intensity. Comp = the values obtained from the coherency matrix of the original quad-polarimetric data.

The results in table 8.2 is plotted in figure 8.20 for H, and figure 8.21 for $\bar{\alpha}$.

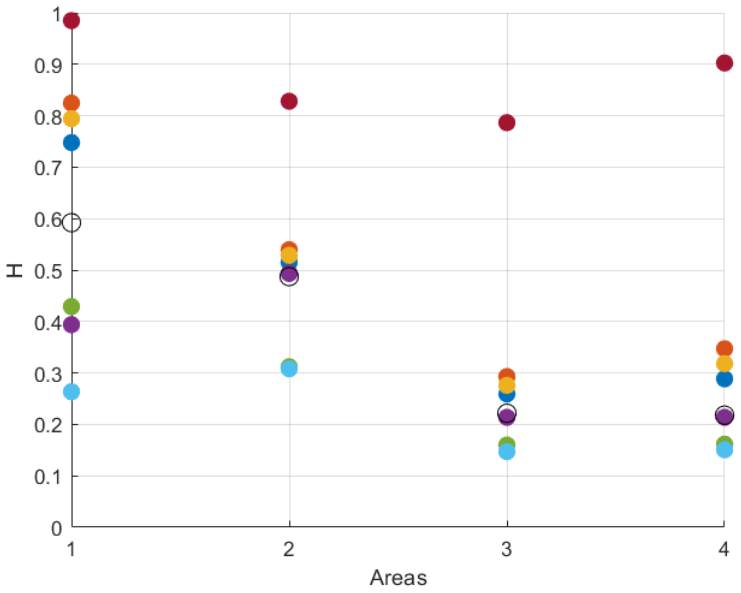

Figure 8.20: H values from all cases over thin newly formed ice, thicker newly formed ice, and two open water areas. Blue = Case 1, orange = Case 2, yellow = Case 3, purple = Case 4, green = Case 5, cyan = Case 6, red = Case 7, black outlined = from the coherency matrix of the original quad-polarimetric data.

From figure 8.20 and previous discussions it is observed that:

- Reduction of polarization channels leads to lower overall H values, which again implies that $H_3 = -\sum_{b=1}^{3} P_b log_3 P_b > H_2 = -\sum_{b=1}^{2} P_b log_2 P_b$, as seen in case 5.

- Raising the NESZ leads to higher overall H values, but has a bigger impact on areas with low backscattering, as seen in case 1, 2, and 3. Raising the NESZ implies higher eigenvalues as the NESZ is only found on the diagonal of the covariance and the coherency matrices. Higher eigenvalues leads to higher H values.

- Lowering of the pixel spacing can cause variation in the relationship between the H values of constituents in the scene as the resolution is changed. This can be seen in case 4 where the relationship between area 1 (a small area of sea ice surrounded by open water) and the other areas is altered.

Case 6 combines pixel spacing adjustment (coarser resolution) and reduction of polarization channels (lower H values), leading to lower overall H values and

a change in the relationship between the H values of area 1 and the other areas.

Case 7 combines pixel spacing adjustment, reduction of polarization channel and adjustment of NESZ, i.e. the only difference between case 6 and case 7 is the adjustment of NESZ. The consequence of adjusting the NESZ is higher overall H values, where areas of low backscattering becomes more affected. Case 7 shows high overall H values and the relationship between area 1 and the other areas is more alike case 1, 2, and 3 as an effect of adjustment of the NESZ. It shows that even though the relationship between all the areas correlates well with the results from the original quad-polarimetric data it might be an effect of NESZ and not the signal itself. It also implies that the relationship between areas with high backscattering is less affected by adjustment of NESZ, and a separation of different constituents can be possible in the H images.

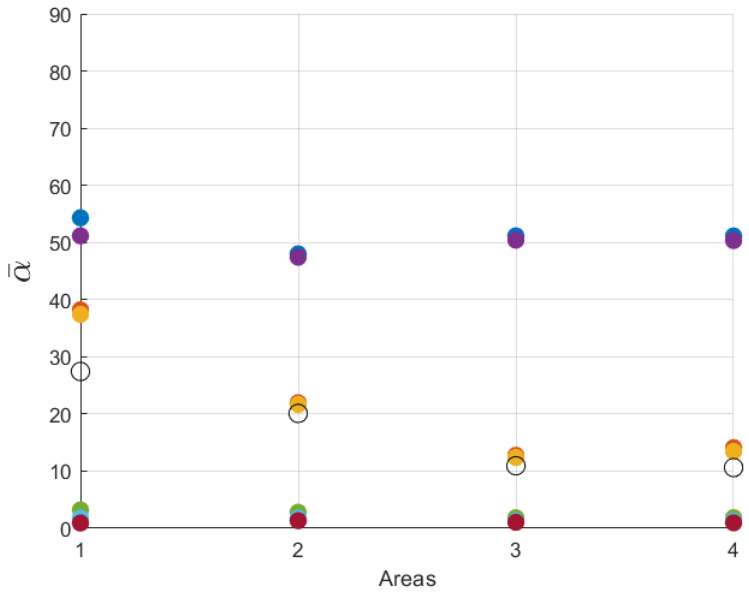

Figure 8.21: $\bar{\alpha}$-angles from all cases over thin newly formed ice, thicker newly formed ice, and two open water areas. Blue = Case 1, orange = Case 2, yellow = Case 3, purple = Case 4, green = Case 5, cyan = Case 6, red = Case 7, black outlined = from the coherency matrix of the original quad-polarimetric data.

The $\bar{\alpha}$-angles is mainly affected by the eigenvectors and the eigenvectors of a coherency and a covariance matrix is different for the same data, but has a relationship to eachother. Case 1 and case 4 utilizes the covariance matrix of the original quad-polarimetric product and the pixel spacing adjusted quad-polarimetric product, respectively. It is apparent that the adjustment of pixel spacing does not affect the $\bar{\alpha}$-angles considerably as the relationship between

areas, and the values are similar in case 1 and case 4. However, a bigger difference between the cases is seen over area 1 as for the H. Case 2 and case 3 is close to identical, which is intuitive as the only difference between the cases is how the NESZ was adjusted. Case 5, 6 and 7 yields similar results to eachother, as only the HH and the HV channel is utilized and elementary scattering mechanisms (surface, double-bounce and volume) is described by the same scattering matrix. To sum up:

- Reduction of polarization channels from a quad-polarimetric product to a dual-polarimetric product utilizing the HH/HV combination causes different scattering mechanisms to be described by the same scattering matrix.

- Raising the NESZ affects only the eigenvalues of the covariance and the coherency matrices as the NESZ is found on the diagonal of these matrices. The $\bar{\alpha}$-angles is mainly dependent on the eigenvectors of these matrices, and it follows that the $\bar{\alpha}$-angles does not change considerably when the NESZ is adjusted.

- Lowering of the pixel spacing can cause variation in the relationship between the $\bar{\alpha}$-angles of constituents in the scene as the resolution is changed. This change is however not as apparent as for the H values.

8.2 Cross-polarization ratio study

When utilizing the cross-polarization ratio only two polarization channels is utilized, and it follows that reduction of polarization channels does not give differences in cross-polarization ratio from quad-polarimetric and dual-polarimetric data. Two possible sources of differences maintain; adjustment of pixel spacing, and adjustment of NESZ. The obtained cross-polarization ratio images for (a) the original quad-polarimetric data, (b) quad-polarimetric data with dual-polarimetric NESZ, (c) downsampled and averaged to meet pixel spacing of SCWA dual-polarimetric products, and (d) downsampled, averaged and NESZ adjusted to obtain a fully emulated dual-polarimetric product is shown in figure 8.22. For simplicity (a) is hereby denoted as $R_{HV/HH}(QP_{QP})$, (b) as $R_{HV/HH}(QP_{DP})$, (c) as $R_{HV/HH}(DP_{QP})$, and (d) as $R_{HV/HH}(DP_{DP})$.

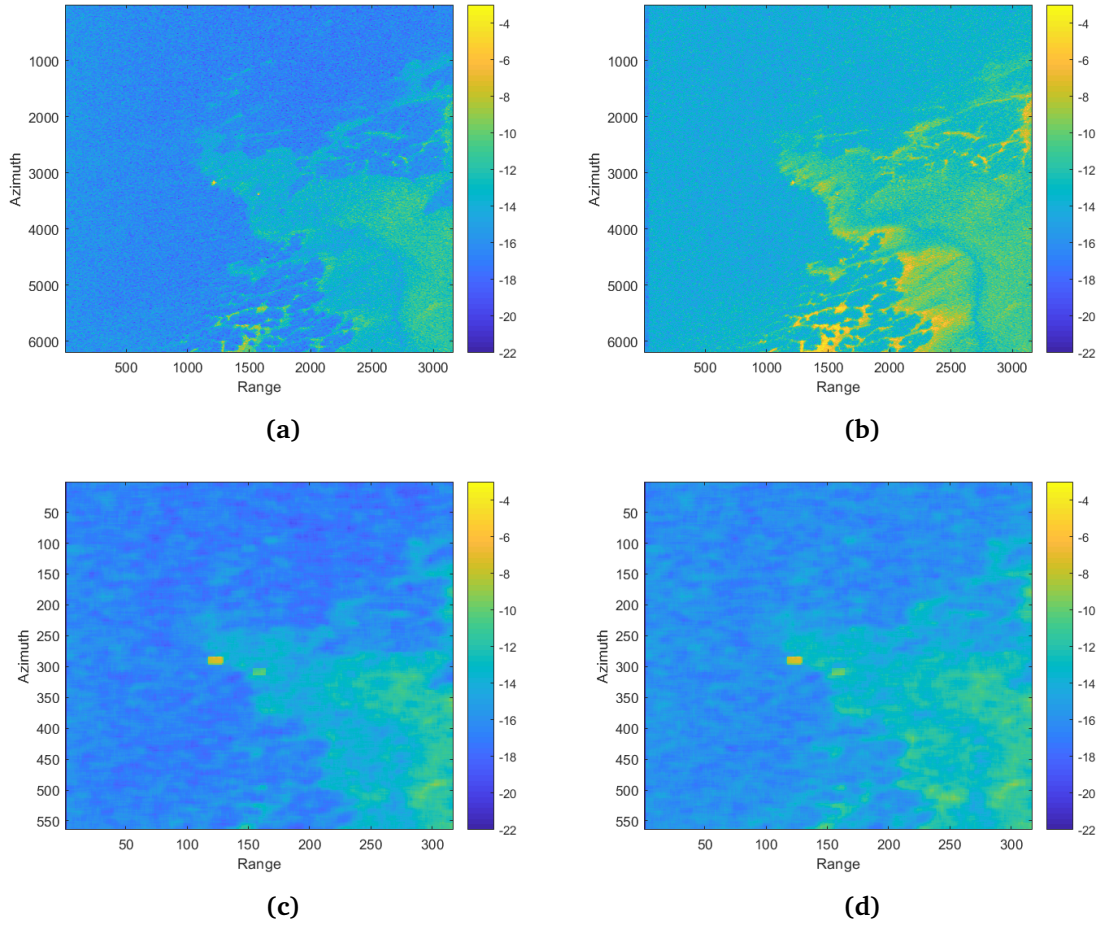

Figure 8.22: Cross-polarization ratio of (a) original quad-polarimetric, (b) quad-polarimetric with dual-polarimetric NESZ, (c) dual-polarimetric with quad-polarimetric NESZ, (d) dual-polarimetric with dual-polarimetric NESZ.

The difference between figure 8.22(a) and figure 8.22(b) is similar to what was seen in Case 1 and Case 2 when the H was discussed. The areas with lower backscattering contains higher values in $R_{HV/HH}(QP_{DP})$ than in $R_{HV/HH}(QP_{QP})$, implying a bigger difference between the HH and HV channels in these areas. This can be seen in figure 8.23 where $R_{HV/HH}(QP_{QP})$ is subtracted from $R_{HV/HH}(QP_{DP})$.

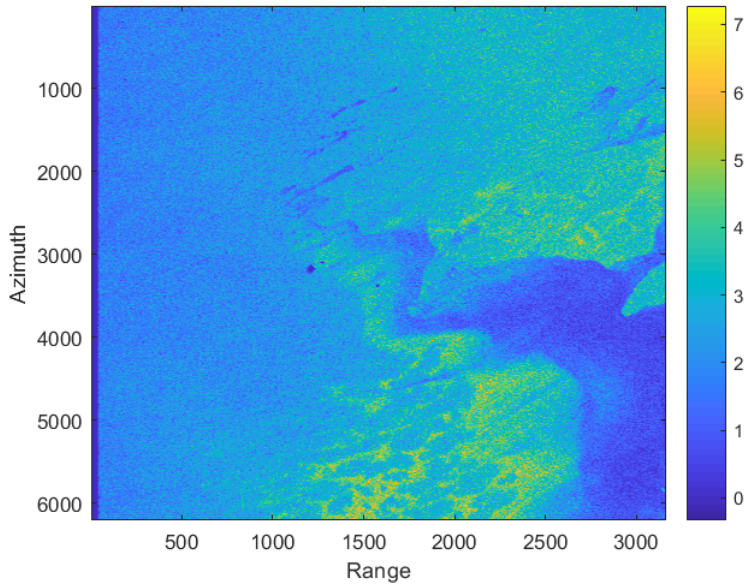

Figure 8.23: $R_{HV/HH}(QP_{QP})$ subtracted from $R_{HV/HH}(QP_{DP})$ in dB.

The HV channel lies closer to the NESZ than the HH channel, i.e. the power of the signal in the HV channel is lower than in the HH channel. When the NESZ is adjusted white Gaussian noise with the same power is added to both channels. The relative change of the signal strength is higher for the HV channel than the HH channel as the original signal power is lower. This again leads to higher values in the cross-polarization ratio, i.e.

$$\left|\frac{a + \langle|S_{HV}|\rangle}{a + \langle|S_{HH}|\rangle}\right| \rangle \left|\frac{\langle|S_{HV}|\rangle}{\langle|S_{HH}|\rangle}\right| \tag{8.2}$$

Where a is a constant.

The adjustment of NESZ (addition of white Gaussian noise) increases the values in the cross-polarization ratio and could be a possible source of error if constituents in the imaged scene is classified only by the cross-polarization ratio.

The effects of the adjustment of pixel spacing in $R_{HV/HH}(DP_{QP})$ resembles what was observed in the H, $\bar{\alpha}$ case studies. The courser resolution is clearly visible when the pixel spacing of a SCWA product is utilized. The range of values decreases, and the variation seen in $R_{HV/HH}(QP_{QP})$ decreases. Finer details are no longer visible, but the overall values are similar. The means and

standard deviations of the 4 images shown in figure 8.22 is presented in table 8.3.

Ratio	Mean value [dB]	Standard deviation [dB]
$R_{HV/HH}(QP_{QP})$	-15.30	1.83
$R_{HV/HH}(QP_{DP})$	-12.88	1.87
$R_{HV/HH}(DP_{QP})$	-15.76	1.61
$R_{HV/HH}(DP_{DP})$	-14.94	1.57

Table 8.3: Mean and standard deviation of $R_{HV/HH}(QP_{QP})$, $R_{HV/HH}(QP_{DP})$, $R_{HV/HH}(DP_{QP})$, $R_{HV/HH}(DP_{DP})$.

Some areas that previously contained different scattering properties is after downsampling harder to observe (area 1), while some areas are not possible to separate from its surroundings (area 2), as seen in figure 8.24. As an interpreter both of these areas are hard to separate from its surroundings, and pre known attributes of the imaged scene is required.

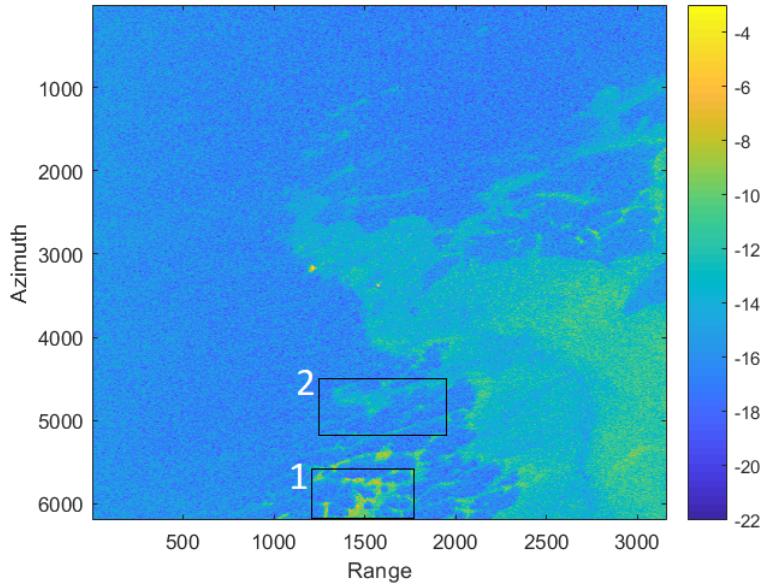

Figure 8.24: Two areas implying different scattering properties in $R_{HV/HH}(QP_{QP})$ and $R_{HV/HH}(DP_{QP})$. Shown in $R_{HV/HH}(QP_{QP})$.

The adjustment of NESZ in $R_{HV/HH}(DP_{DP})$ yields an overall positive change compared to $R_{HV/HH}(DP_{QP})$, as the adjustment of NESZ in $R_{HV/HH}(QP_{DP})$ did compared to $R_{HV/HH}(QP_{QP})$.
The mean of these changes in each range position was calculated as follows:

$$R_{HV/HH}(QP_{diff}) = 10 * log_{10}R_{HV/HH}(QP_{DP}) - 10 * log_{10}R_{HV/HH}(QP_{QP})$$

and

$$R_{HV/HH}(DP_{diff}) = 10 * log_{10}R_{HV/HH}(DP_{DP}) - 10 * log_{10}R_{HV/HH}(DP_{QP})$$

and plotted in figure 8.25. The difference in the dual-polarimetric data were interpolated using nearest neighbour for comparison purposes.

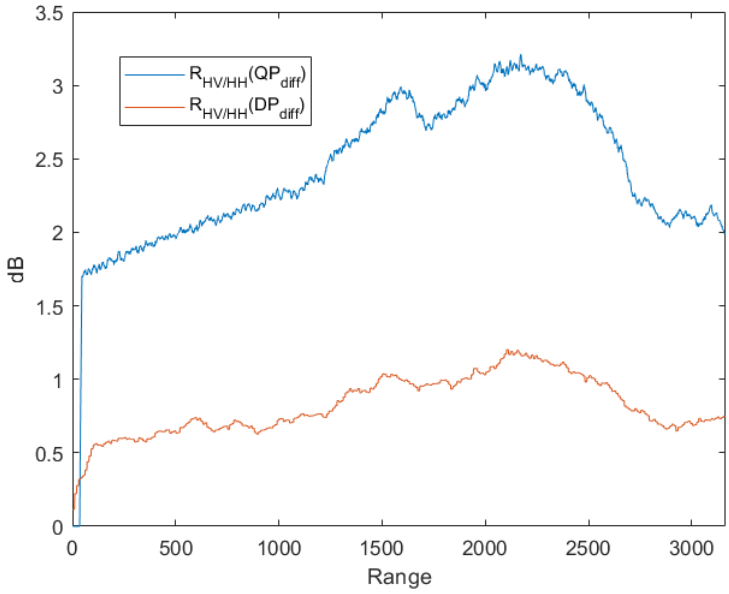

Figure 8.25: mean difference between cross-polarization ratios with quad-polarimetric NESZ and dual-polarimetric NESZ in dB.

$R_{HV/HH}(QP_{diff})$ and $R_{HV/HH}(DP_{diff})$ have similar properties, and the Spearman correlation between them are 0.96. The difference between $R_{HV/HH}(DP_{QP})$ and $R_{HV/HH}(DP_{DP})$ varies between 0.19-1.19 dB for a change of NESZ of about 5 dB in average (see figure 8.3). This change is dependent on the constituents in the imaged scene and the amount of backscatter. The cross-polarization ratio of the fully emulated dual-polarimetric product reveals two distinctively different surfaces in the imaged scene, implying that the imaged scene consists of atleast two surfaces of different scattering properties.

8.3 Damping ratio study

The damping ratio only utilizes one polarization channel, and since the main focus of this thesis is camparison between quad-polarimetric data and dual-polarimetric HH/HV data only the damping ratio of the HH channel and the damping ratio of the HV channel are presented. It is a single-polarization feature, and it follows that the reduction of polarization channels does not affect the damping ratio. The possible sources of difference in damping ratio between quad-polarimetric data and dual-polarimetric HH/HV data is the adjustment of pixel spacing and the adjustment of NESZ. The resulting damping ratio images for the original quad-polarimetric data, quad-poarimetric data with dual-polarimetric NESZ, data with dual-polarimetric resolution and quad-polarimetric NESZ, and the fully emulated dual-polarimetric product is shown in figure 8.26 for the HH channel, and figure 8.27 for the HV channel.

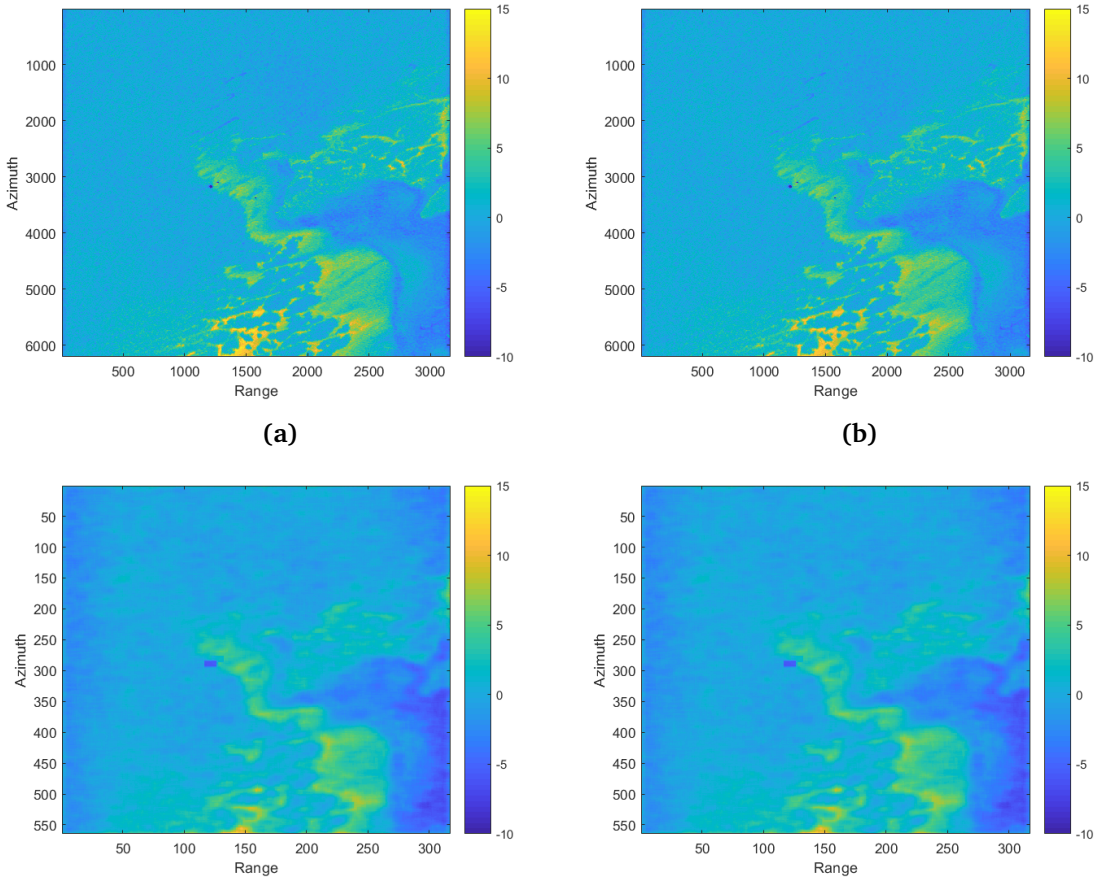

Figure 8.26: Damping ratio of (a) original quad-polarimetric, (b) quad-polarimetric with dual-polarimetric NESZ, (c) dual-polarimetric with quad-polarimetric NESZ, (d) dual-polarimetric with dual-polarimetric NESZ for the HH channel.

Visually, adjustment of the NESZ does not seem to affect the damping ratio from the HH channel much. Adjustment of pixel spacing leads to a coarser resolution, and some areas can be harder to distinguish from its surroundings. The mean value of the damping ratio from the HH channel in the areas outlined in figure 8.16 is presented in table 8.4.

	Area 1	Area 2	Area 3	Area 4
Type of area	TNFI	ThNFI	OW	OW
QP w/ QP NESZ	11.00	-1.45	0.31	1.23
QP w/ DP NESZ	10.11	-1.43	0.30	1.99
DP w/ QP NESZ	7.11	-3.22	-0.39	-0.66
DP w/ DP NESZ	7.03	-3.22	-0.39	-0.66

Table 8.4: Mean value of damping ratio. QP = quad-polarimetric, DP = dual-polarimetric, TNFI = Thin newly formed ice, ThNFI = Thicker newly formed ice, OW = Open water. All values are in dB.

The values shows that for all the cases the ratio over open water in linear domain is close to 1, which is intuitive as values from open water is divided on values from open water in these areas. The damping ratio over thin newly formed ice have higher values than thicker newly formed ice for all the cases, implying that the backscatter from thin newly formed ice is lower.

- Adjustment of NESZ (increasing the NESZ) changes the damping ratio over the areas differently. The difference is caused by the difference in backscatter over the areas. Area 1 is a low backscatter area, and the NESZ adjustment is more dominant as the change of $\langle\sigma_{0,sea}\rangle$ is lower than the change of $\langle\sigma_{0,D}\rangle$, causing a decrease in the damping ratio. $10 * log_{10}(x)$ have the property that it is negatively increasing for $x\langle 1$ and positively increasing for $x\rangle 1$. Area 2 have a negative damping ratio, implying that the backscatter of area 2 is higher than the mean backscatter of open water covering the same incidence angles. Adjustment of NESZ will therefore affect the mean backscatter from open water more than area 2, causing a slight positive change. The change is however much less apparent than the change over area 1. Area 3 have a bigger coverage than the other areas and are located over open water. The change of damping ratio is minimal as $\langle\sigma_{0,sea}\rangle$ is close to the same as $\langle\sigma_{0,D}\rangle$. Area 4 provides interesting findings. The damping ratio is higher for area 4 than area 3, although both contain open water. Possible sources of difference can be the difference in incidence angle (damping ratio changes with increasing incidence angle [31]), damping of the open water from surrounding sea ice and salinity of the water.

  A general statement of the implications of the damping ratio from adjustment of the NESZ follows: For areas of lower backscattering than open water the NESZ adjustment will lower the damping ratio. For areas of same or close to the same backscattering as open water the NESZ adjustment will not affect the damping ratio in a considerable manner. For areas with higher backscatter than open water the NESZ adjustment will move the damping ratio closer to zero.

- Lowering of pixel spacing causes areas of low backscattering surrounded by higher backscattering to increase, such as area 1. Area 1 will therefore have a lower damping ratio. Area 2 will be affected by a boundary of higher intensity values, and the difference between intensity over open water and area 2 increases, leading to a higher negative value of the damping ratio. Area 3 and area 4 undergoes minor changes as these areas covers open water. The difference seen is caused by the surroundings, altering the overall intensity value of the area.

  A general statement of the implications of the damping ratio from adjustment of pixel spacing follows: The implications of adjusting the pixel spacing is dependent on the surroundings of the ROI. It causes coarser resolution so that local variations decreases but the overall values in bigger monotone areas is close to the same.

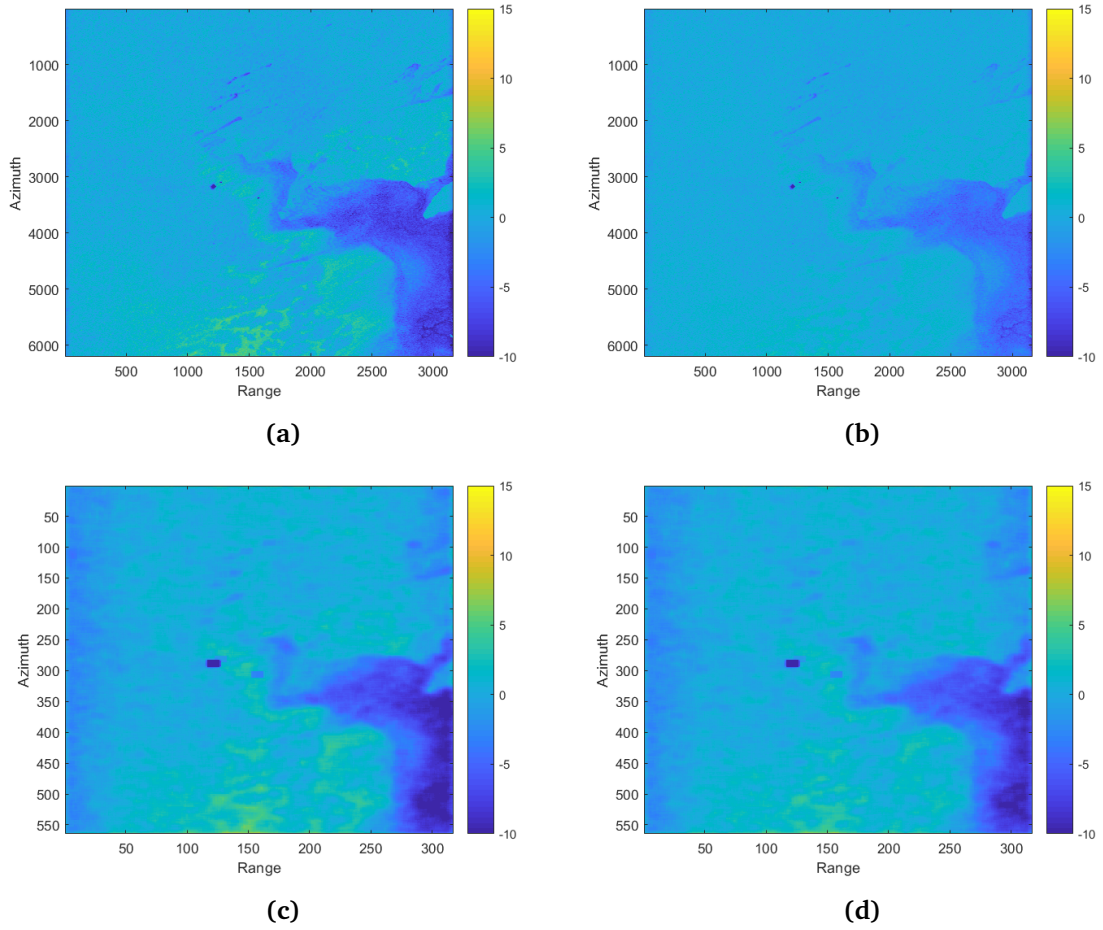

Figure 8.27: Damping ratio of (a) original quad-polarimetric, (b) quad-polarimetric with dual-polarimetric NESZ, (c) dual-polarimetric with quad-polarimetric NESZ, (d) dual-polarimetric with dual-polarimetric NESZ for the HV channel.

Visually, adjustment of the NESZ causes a slight change in the damping ratio over some areas in the HV channel. Adjustment of pixel spacing leads to a coarser resolution, and some areas can be harder to distinguish from its surroundings. The mean value of the damping ratio from the HV channel in the areas outlined in figure 8.16 is presented in table 8.5.

	Area 1	Area 2	Area 3	Area 4
Type of area	TNFI	ThNFI	OW	OW
QP w/ QP NESZ	4.49	-5.85	0.32	0.73
QP w/ DP NESZ	1.85	-3.84	0.19	0.36
DP w/ QP NESZ	4.98	-6.83	-0.14	-0.04
DP w/ DP NESZ	3.76	-6.11	-0.19	-0.29

Table 8.5: Mean value of damping ratio. QP = quad-polarimetric, DP = dual-polarimetric, TNFI = Thin newly formed ice, ThNFI = Thicker newly formed ice, OW = Open water. All values are in dB.

It is apparent that the damping ratio of the HV channel is more affected by the adjustment of the NESZ. This is intuitive as the HV signal contains lower power than the HH signal, and the NESZ adjustment utilizes white Gaussian noise with the same power for both cases. The changes yields the same influence of the damping ratio for the HH and the HV channel except for area 4. It is possible that the NESZ adjustment influences the HV channel enough to overthrow the changes seen in the HH channel, as the NESZ have a bigger impact on the HV channel than the HH channel.

Most operational dual-polarimetric SAR satellites offer HH/HV combinations, and the data used in the master thesis is of this form. Dual-polarimetric HH/VV could in some cases deliver better results than dual-polarimetric HH/HV as the co-polarization channels normally has a better SNR. Dual-polarimetric HH/VV is however only offered from satellites with a quad-polarimetric processor.

The results of this study showed that it could be challenging to interpret the $\bar{\alpha}$-angles and the H values for HH/HV dual-polarimetric data. This is consistent with findings in [49]. Also [1] suggests that the resulting $\bar{\alpha}$ and H is dependent on the polarization channels used. Further [23] states that the HH/HV $\bar{\alpha}$ cannot separate between the different scattering mechanisms.

9

Conclusion

Before the cases were presented it was proven that the H of the coherency- and the covariance matrices from the same data are equal, while the $\bar{\alpha}$-angles becomes different because of the different eigenvectors of the coherency- and the covariance matrices. The H and the $\bar{\alpha}$-angles were originally obtained for the coherency matrix and the $\bar{\alpha}$-angles is consistent with the expected results over open water and thin sea ice (Bragg scattering and Fresnel reflection). The $\bar{\alpha}$-angles obtained from the covariance matrix is higher and classifies the scattering mechanisms wrongly. It is however possible to separate the majority of sea ice from open water visually. As an effect of the erroneous $\bar{\alpha}$-angles the H/$\bar{\alpha}$-plot from the covariance matrix contains too high $\bar{\alpha}$-angles, while the H values are correct. It shows that the H values from a covariance matrix can be used for further polarimetric analysis while the $\bar{\alpha}$-angles will give erroneous numerical results if conventional interpretation is used. A visual interpretation could still be usable.
Case 1, 2, and 3 showed the effects of adding white Gaussian noise to raise the NESZ. They showed that the H undergoes higher changes than the $\bar{\alpha}$-angles as addition of white Gaussian noise only affects the eigenvalues of the coherency- and the covariance matrices. An interesting result became visible in case 1 and 2, where the H became different. The theory presented and the results did not link together and a minor error in the code is most plausible. It was also shown that adding white Gaussian noise on the SLC data or directly on the coherency and the covariance matrices yields small differences (about 7.4 % at most, and less than 2.9% at least). By raising the NESZ of the original quad-polarimetric data to meet the desired dual-polarimetric NESZ no major changes were seen

but the areas with the lowest σ_0 values were most affected. A bigger adjustment of the NESZ could however lead to erroneous results as the H and the $\bar{\alpha}$-angles increases when the NESZ is increased because of the change in eigenvalues.
The emulation of dual-polarimetric data from quad-polarimetric data was done by averaging a neighbourhood of pixels and downsample according to the pixel spacing of SCWA dual-polarimetric products before two polarization channels was removed and the NESZ was adjusted. The pixel spacing adjustment caused the finer details in the H image and the $\bar{\alpha}$-angle image to be reduced. As a direct effect of the averaging the range of H values and $\bar{\alpha}$-angles was reduced. The reduction of polarization channels caused the H values and the $\bar{\alpha}$-angles to decrease. The decrease of $\bar{\alpha}$-angles was proven by utilizing the scattering matrices of quasi-deterministic surface, double-bounce and volume scattering, which is all zero for a dual-polarimetric HH/HV product. The $\bar{\alpha}$-angles of different scattering mechanisms are therefore not separable, and the $\bar{\alpha}$-angles and the H/$\bar{\alpha}$-plot can not be used for dual-polarimetric HH/HV products. The H still separates between open water and sea ice, where higher values are found over sea ice than open water as in the H image from the original quad-polarimetric data.
The final emulation of dual-polarimetric data including adjustment of NESZ yielded an H image unlike the H images obtained in other cases. It consists of high H values, implying a scattering scene with high randomness. The results are erroneous, and shows that the H values obtained in this thesis can not be used. The $\bar{\alpha}$ image consisted of lower values, as two polarization channels are removed. The adjustment of the NESZ does not alter these values as the white Gaussian noise is added on the diagonal of the covariance matrix.
It is clear that dual-polarimetric HH/HV products lack some of the polarimetric features that can be found from quad-polarimetric data (H $\bar{\alpha}$, H/$\bar{\alpha}$). The adjustment of pixel spacing caused the variation of H values and $\bar{\alpha}$-angles to decrease, leading to lesser finer details in the data. The reduction of polarization channels caused the $\bar{\alpha}$-angles from different scattering mechanisms to be the same, making separation of them unlikely. For a dual-polarimetric HH/VV product (only attainable through a quad-polarimetric processor) these effects can possibly be avoided. The adjustment of the NESZ resulted in H values that is not consistent with what is expected for sea ice and open water. A better SNR could yield usable H values, although in this thesis the H and the $\bar{\alpha}$-angles for a dual-polarimetric HH/HV product can not be used for conventional H/$\bar{\alpha}$ interpretation.

The cross-polarization ratio study showed that emulated dual-polarimetric data can sometimes be used without much information loss. The results were not affected by NESZ adjustment in a manner similar to the H and $\bar{\alpha}$, implying that the cross-polarization ratio is less sensitive to the NESZ level. The cross-polarization ratio is however sensitive to the pixel spacing if smaller geometric features and their properties are of interest. The study implies that

dual-polarimetric products can be used to obtain the cross-polarization ratio for studies of medium to large scale geometric bodies consisting of surfaces of medium to high backscattering.

The damping ratio study showed that the adjustment of the NESZ had a bigger impact on the damping ratio from the HV channel than the HH channel. It was also shown that adjustment of pixel spacing leads to a coarser resolution, and that the change of values is dependent on its surroundings. Both channels delivered visually separation of different constituents in the imaged scene for the fully emulated dual-polarimetric product, but better separation was found in the HH channel.

10

Future work

This thesis introduces a study of the differences between H, $\bar{\alpha}$, the H/$\bar{\alpha}$-plot, the cross-polarization ratio, and the damping ratio from quad-polarimetric and dual-polarimetric data. It emulates dual-polarimetric data from quad-polarimetric data and compares the information in each emulation step with the original data. Some factors are after this thesis left unanswered, and improvements on the study can also be made.

- The thesis concludes that conventional interpretation of H, $\bar{\alpha}$, the H/$\bar{\alpha}$-plot of dual-polarization HH/HV products yield erroneous results. It is however in all the cases possible to separate sea ice from open water visually in the H images and a further analysis could yield properties of the H that enables differentiation of bodies in an imaged scene. The $\bar{\alpha}$ did however yield less promising results.

- The cross-polarization ratio can be further analysed and the findings in this thesis can be validated by using more data to back up the findings presented in the thesis.

- The damping ratio was found for the HH and the HV channel. The HH channel showed itself to be less affected by the NESZ adjustment than the HV channel, and different scattering surfaces were more easily separated in the HH channel. A further analysis including incidence angle corrections, and other corrections can be done.

- More features can also be studied, which could give a deeper understanding of the difference in information between quad-polarimetric data and dual-polarimetric data.

- The emulation of dual-polarimetric data can also be done differently. As the adjustment of pixel spacing is done by averaging and downsampling over a local neighbourhood, this neighbourhood is multi-looked. Other studies (such as [11]) proposes a lowpass filter for adjustment of pixel spacing, which could manage to avoid the local multi-looking.

- Dual-polarimetric VV/VH was not covered in this thesis, and can be added in further studies.

- The findings should also be validated towards real dual-polarimetric data. This can be done by comparing quad-polarimetric data and dual-polarimetric data covering the same scene, with an aquisition time as close to equal as possible.

Appendix

The eigenvalues and eigenvectors of matrix $\hat{A}$ is obtained from the expression

$$\hat{A}e = \lambda e \qquad \text{(Appendix.1)}$$

Where e is the eigenvectors, and λ is the eigenvalues.
Rewriting the equation yields:

$$(\hat{A} - \lambda\hat{I})e = 0 \qquad \text{(Appendix.2)}$$

where $\hat{I}$ is the identity matrix, and $(\hat{A} - \lambda\hat{I})$ is singular.
For a matrix to be singular the determinant has to be zero:

$$det(\hat{A} - \lambda\hat{I}) = 0 \qquad \text{(Appendix.3)}$$

This expression is solvable for λ.
The eigenvectors is obtained by solving equation Appendix.2.
A nxn matrix ($\hat{A}$) have n eigenvalues, and the sum of the eigenvalues ($\sum_{i=1}^{n} \lambda_i$) equals the trace of matrix $\hat{A}$ ($\sum_{i=1}^{n} a_{ii}$). When a constant is added to the diagonal of matrix $\hat{A}$, the same constant will be added to the eigenvalues, i.e. If $\hat{A}$ gives the eigenvalues λ_1,λ_2,...,λ_n and a new matrix $B = \Upsilon(c\hat{I})$ where c is a scalar, then the eigenvalues of B equals $c\lambda_i$, because $\sum_{i=1}^{n} ca_{ii} = \sum_{i=1}^{n} c\lambda_i$, where a is elements in $\hat{A}$. [5]

Bibliography

[1] Ainsworth, T.L.; Preiss, M.; Stacy, N.; Nord, M.; Lee, J.S. Analysis of compact polarimetric SAR imaging modes.// Proceedings of the 3rd International Workshop on Science and Applications of SAR Polarimetry and Polarimetric Interferometry. 2007

[2] Bertoia, C.; Falkingham, J.; Fetterer, F. Polar SAR data for operational sea ice mapping.// Analysis of SAR Data of the Polar Oceans. Berlin. Springer-Verlag, pp. 201-234, 1998

[3] Brekke, C.; Holt, B.; Jones, C.; Skrunes. S. Discrimination of oil spills from newly formed sea ice by synthetic aperture radar.// Remote Sensing of Environment, 2014

[4] Calabrese, D.; Episcopo, R. Derivation of the SAR Noise Equivalent Sigma Nought.//EUSAR 2014; 10th European Conference on Synthetic Aperture Radar, 2014

[5] Campbell, J. B.; Wynne, R. H. Introduction to Remote Sensing, 5th ed. New York: The Guilford Press, 2011

[6] Carmack, E., et al. Towards quantifying the increasing role of oceanic heat in sea-ice loss in the new arctic. Bulletin of the American Meteorological Society, vol. 96(12), pp. 2079-2105, 2015

[7] Carsey, F. Microwave remote sensing of sea ice, American Geophysical Union, Vol. 68, 1992

[8] Chuvieco, E., Huete, A. Fundamentals of Satellite Remote Sensing. Boca Raton: CRC Press Taylor and Francis Group, 2010

[9] Cloude, S.R. POLARISATION application in remote sensing. Don Mills: Oxford university press, 2010

[10] Cloude, S.R. The dual polarization entropy/alpha decomposition: A PAL-

SAR case study. 2007

[11] Dierking, W. Sea ice monitoring by synthetic aperture radar.// Oceanography, Vol. 26(2), pp. 100-111, 2013

[12] Dierking, W., Wesche, C., C-band radar polarimetry useful for detection of icebergs in sea ice?// IEEE Transactions Geoscience Remote Sensing, Vol. 52 (1), pp. 25–37, 2014

[13] Drinkwater, M.; Kwok, R.; Rignot, E.; Israelsson, H.; Onstott, R. G.; Winebrenner, D.P. Potential Applications of Polarimetry to the Classification of Sea Ice.//Microwave Remote Sensing of Sea Ice. Geophysical Monograph Series, Vol. 68, pp. 419–430, 1992.

[14] Elachi, C.; Van Zyl, J. Introduction to the physics and techniques of Remote Sensing. 2nd ed. Hoboken, New Jersey: John Wiley Sons, Inc., 2006.

[15] eoPortal Directory. RADARSAT-2. https://directory.eoportal.org/web/eoportal/satellite-missions/r/radarsat-2 (Accessed: 01.12.2017)

[16] European Space Agency. RADAR and SAR Glossary. https://earth.esa.int/handbooks/asar/CNTR5-2.html (Accessed 07.12.2017)

[17] Franceschetti, G.; Iodice, A.; Riccio, D.; Ruello, G.; Siviero. R. SAR raw signal simulation of oil slicks in ocean environments.// IEEE Transactions Geoscience Remote Sensing, Vol. 40(9), pp. 1935–1949, 2002.

[18] Freeman, A. The effect of noise on polarimetric SAR data. Proceeding International Geoscience and Remote Sensing Symposium, pp. 799–802, 1993

[19] Gade, M.; Alpers, W.; Hühnerfuss, H.; Masuko, H.; Kobayashi, T. Imaging of biogenic and anthropogenic ocean surface films by the multifrequency/multipolarization SIR-C/X-SAR.// Journal of Geophysical Research: Oceans, Vol. 103(C9), pp. 18,851–18,866; 1998

[20] Geldsetzer, Y. Sea ice type and open water discrimination using dual co-polarized C-band SAR.// Canadian Journal of Remote Sensing Vol. 35(1), pp. 73-84, 2009

[21] Hajnsek, I.; Papathanassiou, K.P.; Cloude, S.R. Removal of Additive Noise in Polarimetric Eigenvalue Processing. Geoscience and Remote Sensing Symposium, 2001

[22] International Hydrographic Organization. Limits of Oceans and Seas. 3rd edition. 1953 https://www.iho.int/iho_pubs/standard/S-23/S-23_Ed3_1953_EN.pdf Accessed: 24.04.2018

[23] Ji, K.; Wu, J. Scattering Mechanism Extraction by a Modified Cloude-Pottier Decomposition for Dual Polarization SAR.//Remote Sensing. 2015

[24] Kern, S.; Gade, M.; Haas, C.; Pfaffling, A. Retrieval of thin-ice thickness using the L-band polarization ratio measured by the helicopter-borne scatterometer Heliscat. Annals of Glaciology. Vol.44 (1), pp.275–280, 2006

[25] Kim, D.-J.; Moon, W.; Kim, Y.-S. Application of TerraSAR-X data for emergent oil-spill monitoring.// IEEE Transactions on Geoscience and Remote Sensing, Vol. 48(2), pp. 852–863, 2010

[26] King, J., Spreen, G.; Gerland, S.; Haas, C.; Hendricks, S.; Kaleschke, L.; Wang, C. Sea-ice thickness from field measurements in the northwestern Barents Sea.// Journal of Geophysical Research: Oceans, Vol.122(2), pp.1497–1512, 2017

[27] Kwok, R.; Nghiem, S.V.; Yueh S.H.; Huynh, D.D. Retrieval of thin ice thickness from multifrequency polarimetric SAR data.// Remote Sensing of Environment, Vol. 51(3), pp. 361-374, 1995

[28] Lee, J. S.; Pottier, E. Polarimetric radar imaging: From basics to applications. New York: Taylor Francis Group, 2009

[29] MDA. Radarsat-2 product description. Issue 1/13, 2016

[30] MDA. Radarsat-2 product format definition. Issue 1/15, 2016

[31] Minchew, B.; Jones, C.E.; Holt, B. Polarimetric Analysis of Backscatter From the Deepwater Horizon Oil Spill Using L-Band Synthetic Aperture Radar.// IEEE Transactions on Geoscience and Remote Sensing, Vol.50(10), 2012

[32] Moreira, A.; Prats-Iraola, P.; Younis, M.; Krieger, G.; Hajnsek, I.; Papathanassiou, K.P. A tutorial on synthetic aperture radar.// IEEE Geoscience and Remote Sensing Magazine. Vol.1(1), 2013

[33] MOSJ. Sea ice extent in the Barents Sea and Fram Strait. 2018 http://www.mosj.no/en/climate/ocean/sea-ice-extent-barents-sea-fram-strait.html Accessed: 04.04.18

[34] Nandan V.; Geldsetzer T.; Islam T.; Yackel, J.J.; Jagvijay P.S.; Gill, M.; Fuller, C.; Grant G.; Duguay C. Remote Sensing of Environment, Vol. 187, 2016

[35] Natural resources Canada. Polarization in radar systems, 2014 http://www.nrcan.gc.ca/node/9567 (Accessed: 01.12.2017)

[36] National Snow & Ice Data Center. Arctic Sea Ice 101. http://nsidc.org/cryosphere/icelights/arcticsea-ice-101 (Accessed: 01.12.2017)

[37] National Snow & Ice Data Center. Ice formation. https://nsidc.org/cryosphere/seaice/characteristics/formation.html (Accessed: 01.12.2017)

[38] National Snow & Ice Data Center. Salinity and brine. urlhttps://nsidc.org/cryosphere/seaice/characteristics/brine$_s alinity.html$(*Accessed* : 01.12.2017)

[39] Nghiem S.V.; Bertoia C.; Study of Multi-Polarization C-Band Backscatter Signatures for Arctic Sea Ice Mapping with Future Satellite SAR.// Canadian Journal of Remote Sensing. Vol. 27(5), pp. 387-402, 2001

[40] Nghiem, S.V.; Kwok, R.; Yueh, S.H.; Gow, A.J.; Perovich, D.K.; Kong, J.A.; Hsu; C.C. Evolution in polarimetric signatures of thin saline ice under constant growth.// Radio Science. Vol. 32(1), pp. 127–151, 1997

[41] Norwegian polar institute. Barents Sea. 2014 http://www.npolar.no/en/the-arctic/the-barents-sea/ Accessed: 04.04.18

[42] Oliver, C.; Quegan, S. Understanding synthetic aperture radar images. Rayleigh: SchTech Publishing, Inc., 2004

[43] Onstott, R.G. SAR and Scatterometer Signatures of Sea Ice.// Microwave Remote Sensing of Sea Ice. pp. 73–104, 1992

[44] Rabault, J.; Sutherland, G.; Gundersen, O.; Jensen, A.; Measurements of wave damping by a grease ice slick in Svalbard using off-the-shelf sensors and open source electronics. Vol. 63, pp. 372-381, 2017

[45] Raney, R. K.; Hopkins J.; A perspective on compact polarimetry.// Geoscience and Remote Sensing newsletter. 2010.

[46] Sabry, R.; Vachon, P. W. A Unified Framework for General Compact and Quad Polarimetric SAR Data and Imagery Analysis.// IEEE Transactions

on Geoscience and Remote Sensing. Vol. 52, pp. 582-602, 2014

[47] Scheuchl, B.; Flett, D.; Caves, R.; Cumming, I. Potential of RADARSAT-2 data for operational sea ice monitoring.// Canadian Journal of Remote Sensing. Vol. 30(3), pp. 448–461, 2004

[48] Smolyanitsky, V.; Sea-Ice Nomenclature, Vol. 1,2,3. 2015. http://www.jcomm.info/index.php?option=com_oe&task=viewDocumentRecord&docID=14598 (Accessed: 15.02.2018)

[49] Sugimoto, M.; Ouchi, K.; Nakamura, Y. On the similarity between dual- and quad-eigenvalue analysis in SAR polarimetry.// Remote Sensing Letters. 2013

[50] WMO/OMM/. WMO Nomenclature no 259. http://www.aari.ru/gdsidb/xml/volume1.php?lang1=0&lang2=1&arrange=0&self=0 (Accessed: 15.02.2018)

[51] Wohl, G.M.; Operational Sea Ice Classification from Synthetic Aperture Radar Imagery.// Photogrammetric Engineering and Remote Sensing. Vol. 61(12), pp. 1455-1462, 1995

[52] Woodhouse, I. H. Introduction to microwave remote sensing. Florida: Taylor Francis Group, 2006.

[53] Yang, J., Yamaguchi, Y., Lee, J.S, Touzi, R., Boerner, W.M.; Applications of Polarimetric SAR.// Journal of Sensors. Vol. 2015, 2015

[54] Zakhvatkina, N.; Korosov, A.; Muckenhuber, S.; Sandven, S.; Babiker, M.; Operational algorithm for ice-water classification on dual-polarized RADARSAT-2 images.// The Cryosphere. Vol. 11, pp. 33-46, 2017

[55] Zhang, X.; Dierking, W.; Zhang, J.; Meng, J.; Lang, H.; Retrieval of the thickness of undeformed sea ice from simulated C-band compact polarimetric SAR images.// The Cryosphere, Vol. 10, pp. 1529–1545, 2016